Adsorption Calorimetry for Energy Conversion Technologies: Applications in Organic Photovoltaics, Catalysis, and Atomic Layer Deposition

James M. Lownsbury

A dissertation

submitted in partial fulfillment of the

requirements for the degree of

Doctor of Philosophy

University of Washington

2016

Reading Committee:

Charles T. Campbell, Chair

David G. Castner

Jim Pfaendtner

Program Authorized to Offer Degree:

Chemical Engineering

University of Washington

Abstract

Adsorption Calorimetry for Energy Conversion Technologies: Applications in Organic Photovoltaics, Catalysis, and Atomic Layer Deposition

James M. Lownsbury

Chair of the Supervisory Committee:
Professor Charles T. Campbell
Chemical Engineering

Fossil fuel combustion accounts for over two-thirds of greenhouse gas emissions worldwide, and as the global population continues to grow, so does our carbon footprint. The root cause of climate change is relatively simple to describe: atmospheric CO_2 transmits visible light from the sun, but absorbs infrared light radiated by the Earth. This "greenhouse effect" makes life on Earth possible, but it is somewhat sensitive to the concentration of CO_2 (and other gases) in the atmosphere. Unfortunately, solving anthropogenic climate change is not nearly as simple as causing it. Since the end of the Industrial Revolution in 1870, global carbon emissions have increased exponentially, with over *30 gigatons* of CO_2 released in 2013 alone. Moreover, with an effective atmospheric residence time of ~200 years, roughly a quarter of those CO_2 molecules released at the end of the 19^{th} century still contribute to climate change today! It is clear that a multifaceted approach must

be taken in order to mitigate the harmful effects of climate change, and key to these efforts will be the research and development of (1) efficient, new energy conversion technologies that take advantage of abundant renewable resources, such as solar energy, (2) advanced catalytic materials with high selectivity and activity in order to make industrial processes more efficient, and (3) porous materials capable of high volume carbon capture.

Organic photovoltaics (OPV) are promising "third-generation" solar cells that can be produced cheaply and scaled to large areas. In normal operating mode, OPV devices are typically structured by mixing an electron-donating polymer with electron-accepting fullerene, with this "bulk heterojunction" sandwiched between a transparent conducting anode and metal cathode. Thus, metal-organic interfaces, such as that between the electron acceptor and electron-conducting metal cathode, are critical to the performance of these devices, and while much research in the OPV field is focused on incrementally bumping up device efficiency, a deeper understanding of these systems can be gained through surface science studies of these crucial interfaces as they are prepared.

Likewise, the structure-functional relationships between metal nanoparticles and metal-oxide supports is a topic of immense interest to the field of heterogeneous catalysis. Metal-organic frameworks (MOFs) are extremely versatile materials composed of small metal or metal oxide nodes connected by organic linker groups of a fixed length and conformation, forming highly ordered, porous structures with large surface areas. Since the nodes in many MOFs are oxide clusters of controllable sizes near ~1 nm in diameter, they can be thought of as very well-defined and homogeneous oxide "nano-supports" to which catalytic metals can be attached to improve activity or simply to provide a more homogeneous and well-defined structure to facilitate fundamental studies of oxide-supported metal clusters. The organic linker groups effectively

isolate these nodes (and the supported metals) from each other, thus possibly preventing sintering of the metal centers. Thus, MOFs hold great promise for applications in heterogeneous catalysis, separations, and greenhouse gas storage, and the binding of metal atoms to the oxide nodes of MOFs is a subject of considerable interest.

In this dissertation, adsorption calorimetry is used in concert with surface spectroscopies in ultrahigh vacuum (UHV) to study the adsorption of calcium metal onto phenyl-C_{61}-butyric acid methyl ester (PCBM), by far the most well-studied and prominently-used electron accepting material in OPV. Calcium metal, due to its very low work function, is commonly used as a cathode material in normal OPV devices, making the Ca/PCBM interface critically important for understanding device performance and stability. This study reveals a tendency for Ca metal to diffuse subsurface over 10 nm deep and react aggressively with subsurface methyl ester groups of PCBM to make the Ca carboxylate of PCBM.

Next, a comprehensive experimental and theoretical study of Ca metal on the MOF NU-1000 is presented. NU-1000 is a particularly promising MOF for catalysis because of its water- and temperature-stability, and large porosity and surface area. Our results reveal a tendency for Ca metal to diffuse subsurface over 20 nm deep to react strongly with the hydroxyl- and H_2O-terminated nodes producing $Ca(OH)_2$ nanoparticles. This is the first study where the interaction of metal atoms with the metal-oxide cluster nodes of *any* MOF has been characterized in detail with respect to experimental bonding energetics, and it provides a crucial benchmark for computational models of metal bonding to the oxide nodes in MOFs.

Finally, this dissertation presents the first-ever calorimetric measurements of the adsorption of precursors used in atomic layer deposition (ALD) using a specially-designed calorimeter. According to the ISI Web of Science, journal articles on the topic of ALD were cited

>32,000 in the year 2015 alone, a trend which has grown exponentially since the first publication in 1981. ALD is a versatile technique for depositing uniform thin films of precision thickness with exceptional conformity to underlying substrates, even when the surfaces are extremely complex. It has been applied to a wide range of fields including semiconductors, batteries, biomaterials, photovoltaics, and catalysis, including OPVs and MOFs, making this study a perfect complement to our UHV adsorption calorimetry experiments. Unique to ALD is the sequential, self-limiting surface reactions that are separated in time by inert gas purging. We focus on the sequential reaction of trimethylaluminum and water to make Al_2O_3, by far the most extensively studied ALD reaction scheme and the focus of numerous review papers, which cycles between a methylated and hydroxylated surface. We show that the reaction heat of the first half-reaction is ~426 kJ/mol and that for the second half-reaction is ~187 kJ/mol (both exothermic). These measured energies will enable future computational studies to verify the nature of the surface intermediates involved in the elementary steps of this highly important ALD process to make conformal alumina films. We then extend this new ALD calorimetry technique to the formation of three other relevant oxides films by ALD—TiO_2, MnO, and one other process to make Al_2O_3—to highlight the technique's versatility.

Taken together, the work presented in this dissertation represents an attempt at deeper understanding of interfaces pertinent to the broad fields of energy conversion and carbon capture, and these results will help to guide the development of efficient new technologies, which is vitally important in order to address the global issue of climate change. The calorimetric study of Ca on PCBM is perhaps the most fundamentally significant study yet produced by our group on metal-organic interfaces, and serves as a perfect complement to the suite of studies by our group of Ca metal adsorption on organic semiconducting polymers. We also applied our UHV adsorption

calorimetry technique to perform the first-ever study of metal adsorption on the nodes of any MOF, providing a benchmark for validating the energy accuracy of the computational methods used to model metal bonding to the oxide nodes in MOFs, and to oxide clusters in general. Finally, the introduction here of the first calorimeter for measuring heats of adsorption of ALD precursors has vast potential for future applications, as ALD is a uniquely capable technique with wide-ranging applicability, but very little is known about the enthalpies involved during ALD half-reactions. Moreover, the accuracy of computational methods used for calculating these energies, such as density functional theory, is not known without such experimental energies to reference. Thus, our calorimeter will provide valuable benchmark energies for ALD reactions on surfaces, with future applications in syntheses of a broad range of materials, such as catalysts, photovoltaics, microelectronics, sensors, biomaterials and coatings, all of broad interest to the scientific community.

TABLE OF CONTENTS

LIST OF FIGURES

LIST OF TABLES

ACKNOWLEDGEMENTS

I would like to thank Ivan Santos-López and Wei Zhang for their help collecting data for the Ca on NU-1000 project. I would like to thank the groups of Donald Truhlar and Christopher Cramer at the University of Minnesota for their computational work for the Ca on NU-1000 project, specifically Haoyu Yu and Wei-Guang Liu. I would also like to thank Timothy Wang and the groups of Joseph Hupp and Omar Farha at Northwestern University for providing invaluable insight into zirconium MOFs, and of course for providing the NU-1000 samples. For my ALD calorimetry project, I thank Alex Martinson and In Soo Kim at Argonne National Laboratory for their tireless efforts and deep knowledge of ALD processes, and even more for their emotional support during my two trips to Argonne as seemingly everything that could go wrong, did go wrong, including me getting stuck in an elevator. I would also like to thank the brilliant scientists I have been lucky to spend some time with over the years: Peter Sherwood, Ronald Imbihl, Oscar Vilches, George Krizek, Charles Peden, and Charles Mims. I enthusiastically thank Eric Strakbein, Ed McArthur, John Heutink, and Brian Holm from the Chemistry Machine Shop, and Bob Scott in the Physics Machine Shop, for their expertise when building/modifying all the unique parts on my myriad instruments, their advice during design phases, and for basically being available to help whenever I needed them. I should perhaps give the Electronics Shop their own acknowledgements section, as I cannot imagine finishing my degree in the maximum ten years allotted without their combined knowledge. They always seemed to find a way to process my frenzied, inscrutable queries and provide me with cogent advice, and they saved me inestimable hours of troubleshooting troubled electronics. So thanks a million to Lon Buck, Roy Olund, Bill Beaty, and Jim Gladden.

I would like to thank the Campbell group. During my time at the University of Washington, the group has always been made up of very bright, passionate, and funny people from all over the world (refer to the map in our office). I would specifically like to thank Eric Karp for helping me get acclimated early on, Christopher Wolcott, Stephanie Hemmingson, Trevor James, Trent Silbaugh, and Ivan Santos-López for their friendship and straight-talking, and Wei Zhang for being a perfect apprentice and picking up a very complicated instrument exceptionally quickly. And of course, I would like to thank Charlie Campbell, for being a better boss than I could have imagined and helping me navigate these frequently choppy waters. Our group dynamic perfectly reflects Charlie, who works impressively hard, but always seems to have a good time along the way.

Finally, I would like to thank my family, my friends, and especially Mallary. I wouldn't have made it without you.

Chapter 1. Introduction

While coal, oil, and natural gas are projected to dominate the global energy portfolio over the next 100 years, the extensive processes of discovery, extraction, refinement, and combustion of these nonrenewable resources contribute greatly to global climate change.[1] Emissions from the combustion of fossil fuels account for over two-thirds of anthropogenic greenhouse gas emissions worldwide.[2] As the world's population and energy demands continue to grow, the development and implementation of new energy sources which take advantage of abundant renewable resources is imperative. Additionally, robust efforts must be made to mitigate the harmful effects of continued carbon emissions[3] through high volume carbon capture projects and efficiency improvements to catalytic processes *via* the development of catalytic materials with high selectivity and activity.[4] Advanced photovoltaic devices and catalytic materials can be used in concert to address these issues that face our planet today and into the future.

Sunlight is the most promising source of renewable energy as it is clean, free, and abundant mostly everywhere on Earth. In fact, enough solar radiation strikes the Earth's surface every day to meet the world's *annual* energy requirements.[5] Although device efficiency improvements and production refinements have dramatically lowered the electricity cost of photovoltaics (PV) over the last 15 years, solar PV remains expensive when compared to conventional energy sources.[6] Additionally, the best performing single-junction solar cells have either seen their power conversion efficiency (PCE) stagnate (crystalline Si cells topped out twenty years ago at ~25%)[7,8] or rely on the use of relatively rare metals such as indium, tellurium, and gallium, which are only produced as mining byproducts, making their extraction unscalable (for example, in order to double the production of tellurium, we would have to double the production of copper).[9,10] Because of these drawbacks, extensive research efforts have been applied toward the development of

affordable alternatives to established solar technologies.[11-13] Solar cells with active layers composed of organic materials[12] have emerged as one of the most promising "third-generation" photovoltaics. In recent years, efficiencies of organic solar cells have surged upward, finally topping 10% after years of stagnation (as shown in **Figure 1.1**).[7,8] Coupled with relatively low cost and the possibility of large area production, this increased efficiency makes these organic photovoltaics a viable challenger to established silicon solar cells.

Interfaces play an integral role in photovoltaic devices. The active layer absorbs and converts solar radiation into free charge carriers that must be transported effectively to an external circuit for the solar cell to have any meaningful utility, and this is achieved across interfaces between efficient conductors and the absorber layers (see **Figure 1.2**).[14-16] Because active layers in organic electronic and optoelectronic devices are made of "soft", carbon-based materials, mixed interfacial regions tend to form instead of discrete interfaces during vapor deposition of the "hard" conductive materials required to get electrical charge to external circuitry.[17] As metals are deposited onto organic materials they can interact in a variety of ways, such as subsurface diffusion,[18] reaction,[19] wetting the surface or balling up into 3D particles,[20] and charge transfer.[21] Adsorption microcalorimetry (described in detail in Chapter 2) provides direct information about the structure and energetics of these interfaces. Also, because the nature of the interface "evolves" with the amount of metal deposited, adsorption microcalorimetry is perfectly suited for investigating the development of mixed interfacial regions which are critical to all organic electronic devices.

Previous studies by the Campbell group have used calorimetry along with surface analysis techniques to analyze the growth of metal thin films by metal vapor deposition onto polymers used in organic photovoltaics (OPV),[22-25] organic light-emitting diodes (OLEDs),[25,26] and integrated

circuits.[27-30] This combination of techniques allowed our group to characterize the structure and energetics of the evolving metal/polymer interfaces as they are formed during actual device fabrication. In a study of calcium film growth on poly(3-hexylthiophene) (P3HT)—commonly used as light absorber and electron donor in the active layer of model OPV devices along with fullerenes[31]—our group found that Ca abstracted sulfur from the thiophene ring in the repeat unit of the polymer to form clusters of CaS up to 3 nm deep.[22] A similar investigation of Ca on poly(5-(2-(ethylhexyloxy)-2-methoxycyano-terephthalyliden)) (MEH-CN-PPV) showed Ca reacted strongly with the polymer's cyano and oxygen groups ~5 nm below the surface.[25] Calcium was shown to form the Ca carboxylate of poly(methyl methacrylate) (PMMA) up to six lamellar layers deep.[28,29] Finally, Ca growth on poly(9,9-di-*n*-hexyl-2,7-fluorene) (PDHF) and poly(9,9-di-*n*-hexyl-2,7-fluorene vinylene) (PDHFV), two polyfluorenes commonly used in OLEDs, showed very weak interactions between Ca and the underlying polymer films.[26] Both PDHF and PDHFV are polymers composed purely of hydrocarbon groups. These studies conclusively show that Ca reacts strongly with polymers containing heteroatoms such as oxygen, nitrogen, and sulfur.

Chapter 3 of this report describes an extension of this previous work on conjugated polymers to a ubiquitous molecular organic semiconductor, phenyl-C_{61}-butyric acid methyl ester (PCBM). Specifically, it describes Ca film growth on spincoated PCBM with adsorption microcalorimetry, low energy He^+ ion scattering spectroscopy (LEIS), and X-ray photoelectron spectroscopy (XPS) to develop a complete mechanistic and energetic study of this evolving interface. Fullerenes are almost universally used as electron acceptors in planar junction and bulk heterojunction OPV devices,[32-35] and PCBM is by far the most commonly used fullerene.[31] In 1995, Heeger et al.[36] published the first report of a bulk heterojunction solar cell device, using MEH-PPV as an electron donating polymer and PCBM, a soluble derivative of C_{60}, as the electron

acceptor. This paper was revolutionary, with over 6000 citations as of this writing, and a bit serendipitous as well, as PCBM was not selected for the experiments following an extensive survey of possible electron accepting materials. Still, after over two decades of research into new n-type molecules/polymers to replace it, PCBM remains the best choice for high performing donor/acceptor OPV devices,[37] making PCBM a perfect model material for our investigation of cathode interface formation on an electron acceptor. Calcium is a common historically-used metal cathode in OPVs (and OLEDs) due to a very low work function that allows for the formation of an ohmic contact with the lowest unoccupied molecular orbital (LUMO) of PCBM, leading to high open circuit voltages and fill factors.[38,39] Understanding the interfaces of a low-work-function metal like Ca with PCBM is critical in order to gain a fundamental understanding of device performance and stability.

As solar PV technologies become less expensive,[6] more efficient,[8] and continue to expand into exciting new territories,[40-43] solar PV is slowly, but surely increasing its share of the world energy portfolio.[44] However, more work must be done to mitigate the future harmful effects of climate change. This problem can be viewed through another lens: efficiency. The world still relies on catalytic chemical processes to produce everything from the food we eat to the fuels we use for transportation.[45,46] As such, there is tremendous interest in the development of new catalysts offering improved efficiency and selectivity.[47-51] Following in the footsteps of zeolites, already an excellent, broadly-applicable class of high-surface-area catalysts in their own right,[52-54] researchers have invested considerable efforts toward the development of a new class of nanoporous crystalline materials called metal-organic frameworks (MOFs). Due to a unique combination of properties, such as structural homogeneity,[55] large surface areas[56] and pore sizes,[57] and framework flexibility,[58] MOFs hold great promise for applications in heterogeneous catalysis,[59-64]

separations,[65,66] and greenhouse gas storage.[67-70] Perhaps more impressively, these materials provide the opportunity for rational design and tunability[71,72] to the desired application and have nearly limitless compositional diversity,[73] which should yield viable materials much faster than the historically-used guess-and-check method.[74,75]

Chapter 4 details an extension of our group's UHV adsorption calorimetry technique to this exciting new class of materials. MOFs are extremely versatile materials composed of small metal or metal oxide nodes connected by organic linker groups of a fixed length and conformation, forming highly ordered, porous structures with large surface areas.[56] Since the nodes in many MOFs are oxide clusters of controllable sizes near ~1 nm in diameter, they can be thought of as very well-defined and homogeneous oxide "nano-supports" to which catalytic metals can be attached to improve activity or simply to provide a more homogeneous and well-defined structure to facilitate fundamental studies of oxide-supported metal clusters. The organic linker groups effectively isolate these nodes (and the supported metals) from each other, thus possibly preventing sintering of the metal centers. Thus, the binding of metal atoms to the oxide nodes of MOFs is a subject of considerable interest. Chapter 4 presents a comprehensive study of the bonding energetics of Ca atoms to the hydroxyl- and H_2O-terminated Zr_6O_{12} nodes of the MOF NU-1000 (see **Figure 1.3** for structure) using adsorption microcalorimetry, surface spectroscopies, atomic beam/surface scattering, and Kohn-Sham density functional theory (DFT). This is the first study where the interaction of metal atoms with the metal-oxide cluster nodes of any MOF has been characterized in detail with respect to experimental bonding energetics, and it provides an experimental energy benchmark for validating the energy accuracy of the DFT methods used to model metal bonding to the oxide nodes in MOFs, and to oxide clusters in general, a subject of high importance to the future of catalysis research.

Interfaces between metals/metal oxides and organic materials are necessarily ubiquitous in OPV.[16,76] Such interfaces in MOFs are well-researched with the goal of improving their catalytic applicability.[77,78] These interfaces can be formed in a number of ways, such as physical and chemical vapor deposition; however, many of these methods are destructive to organic materials. Additionally, the deposition of uniform films with high conformity is not a facile achievement. Atomic layer deposition (ALD) is a remarkably versatile technique (as highlighted in **Figure 1.4**) for depositing uniform thin films of precision thickness with exceptional conformity to underlying substrates, even when they are very rough or porous.[79,80] Unique to ALD is the sequential, self-limiting surface reactions that are most commonly separated in time by inert gas purging. ALD has been shown to be an effective technique for deposition onto organic substrates at low temperatures, thus avoiding substrate degradation and interpenetration.[81-84] Additionally, ALD in MOFs shows great promise as an effective way to improve the catalytic activity of MOFs *via* deposition of catalytic metals directly onto MOF nodes.[85-87] This technique has exploded in popularity in recent years; according to the ISI Web of Science, the number of papers that have "atomic layer deposition" or "atomic layer epitaxy" (an early name for the technique) in their topic has grown exponentially since the first publication in 1981, from ~400 papers in 2005 to ~1500 in 2015, (see **Figure 1.5**). Still, despite the prevalence of ALD in research and industry, thorough experimental investigations of the (often strongly exothermic) heats released during ALD reactions have yet to be reported.

In Chapter 5, we present the first-ever results of a new adsorption calorimeter designed specifically to measure the heats of adsorption of precursors used in ALD. The most extensively studied ALD reaction scheme is the formation of amorphous Al_2O_3 *via* alternating exposure of

surfaces to trimethylaluminum (TMA) and H_2O vapor.[79] The reaction mechanism is well known to occur by alternating surface hydroxyl- and methyl-termination,[88]

$$*(OH)_x + Al(CH_3)_3 \rightarrow *O_x–Al(CH_3)_{3-x} + x\ CH_4$$

$$*O_x–Al(CH_3)_{3-x} + 1.5\ H_2O \rightarrow *O_{1.5}–Al(OH)_x + (3-x)\ CH_4$$

$$Al(CH_3)_3 + 1.5\ H_2O \rightarrow 0.5\ Al_2O_3 + 3\ CH_4$$

where the asterisks indicate surface species and the variable *x* represents the number of methyls which react in the first step, producing CH_4 gas. Though many theoretical studies of the TMA–H_2O process have been derived from first principles computation (DFT),[89] the calculated heats associated with each reaction scheme remains untested compared to experiment. The ability to experimentally determine the heats of ALD half-reactions, demonstrated in Chapter 5 with a focus on Al_2O_3 ALD, will help to fully elucidate these mechanisms and the detailed structures of the surface intermediates involved, and provide crucial benchmarks for theoretical studies of ALD processes in general.

Taken together, the work presented in this dissertation represents an attempt at deeper understanding of interfaces pertinent to the broad field of energy conversion. Chapter 3 presents perhaps the most fundamentally significant study yet produced by our group on metal-organic interfaces, and Chapter 4 presents the first-ever calorimetric study of metal adsorption on the nodes of any MOF. Finally, as presented in Chapter 5, the development of a new adsorption calorimeter to measured heats of adsorption of precursors during ALD expands the direct calorimetry technique pioneered by the Campbell group into an exciting new territory. This last chapter highlights a surprising lack of available energetic information in a field currently experiencing an

explosion of interest, as shown in **Figure 1.5**, and as such, this work has the potential to be highly impactful in the future.

FIGURES

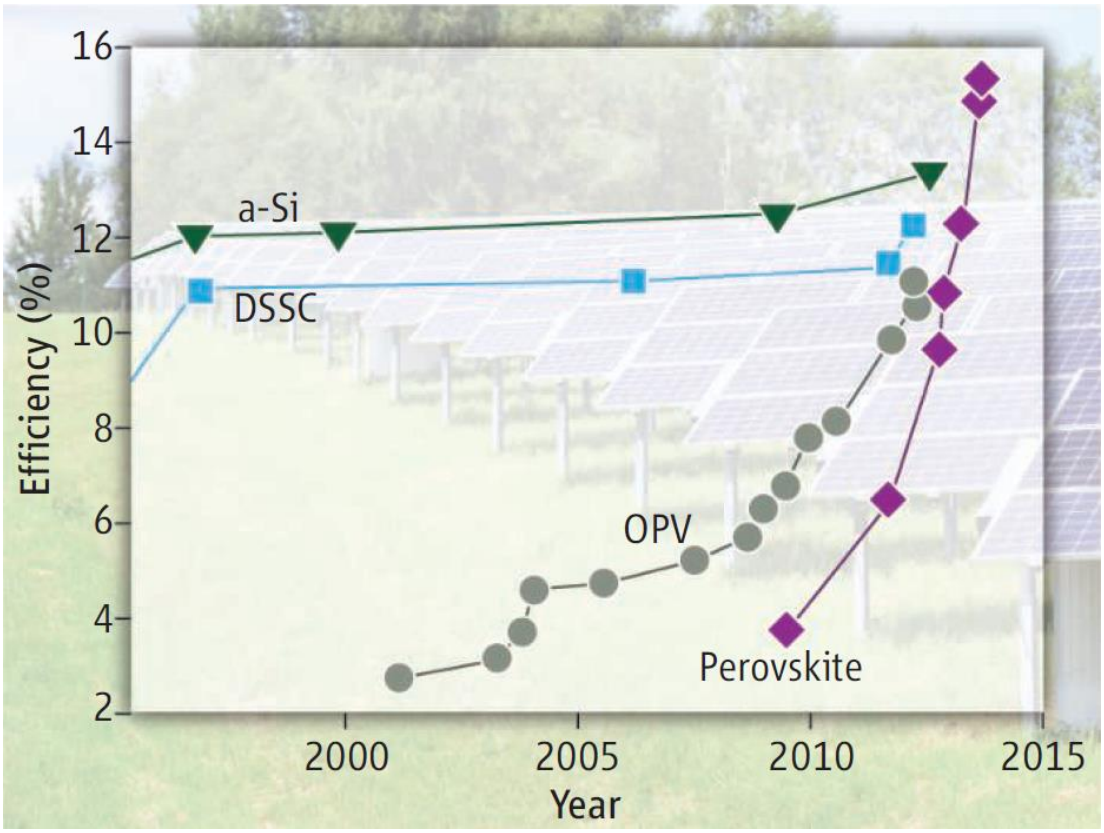

Figure 1.1. Confirmed efficiencies of emerging photovoltaics and amorphous Si (a-Si, green lines and markers) solar cells in recent years. Organic photovoltaics (OPV) are shown in grey, perovskite solar cells are shown in purple, and dye-sensitized solar cells (DSSC) are shown in blue. Reproduced from reference 41. Since this chart's publication in 2013, perovskite solar cell efficiencies have topped 20%.[7]

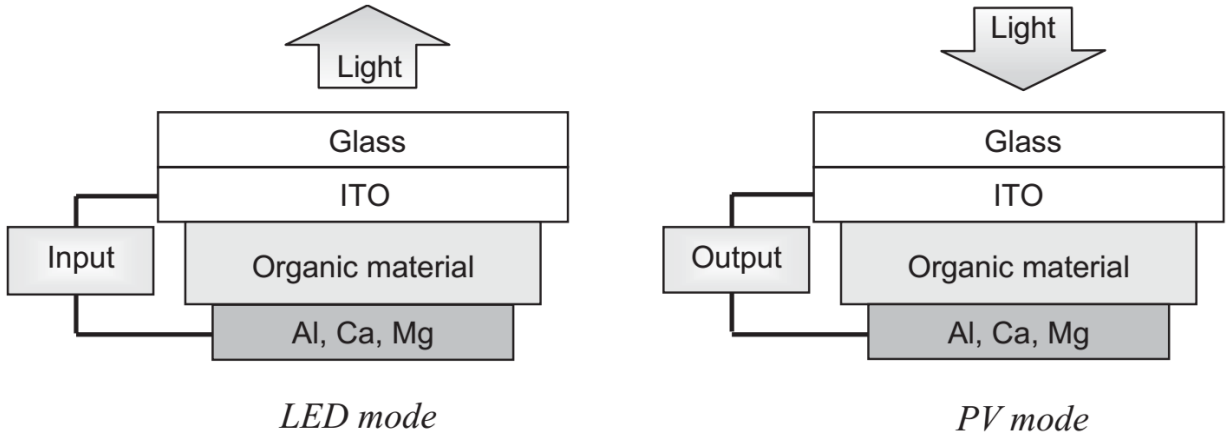

Figure 1.2. Simplified diagrams of OLED (left) and OPV (right) devices, with typical electrode materials. In OPVs, photons pass through the transparent ITO electrode and are absorbed by the organic active layer, producing excitons which can dissociate into free electrons and holes. Electrons are collected at the metal electrode and holes are collected at the ITO electrode. The reverse happens in an OLED device: electrons are introduced at the metal electrode, which recombine in the organic active layer with holes introduced at the ITO electrode, producing photons. Reproduced from reference 90.

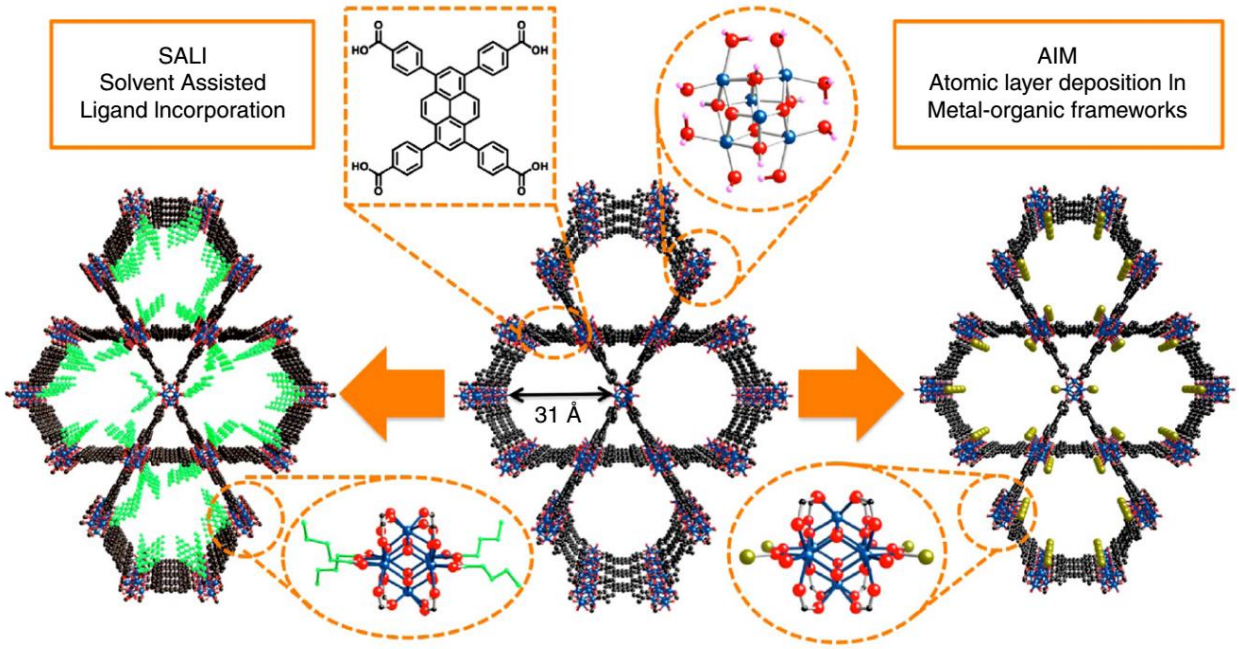

Figure 1.3. Structure of NU-1000, shown in the center, and developed post-synthetic modification methods: solvent assisted ligand incorporation (SALI) and atomic layer deposition in metal-organic frameworks (AIM). Blue, red, black, and white spheres represent zirconium, oxygen, carbon, and hydrogen, respectively. NU-1000 modified by perfluoroalkanes (green lines) *via* SALI[91,92] is shown on the left, and by metal clusters (gold spheres) deposited *via* AIM[85-87] is shown on the right. Reproduced from reference 93.

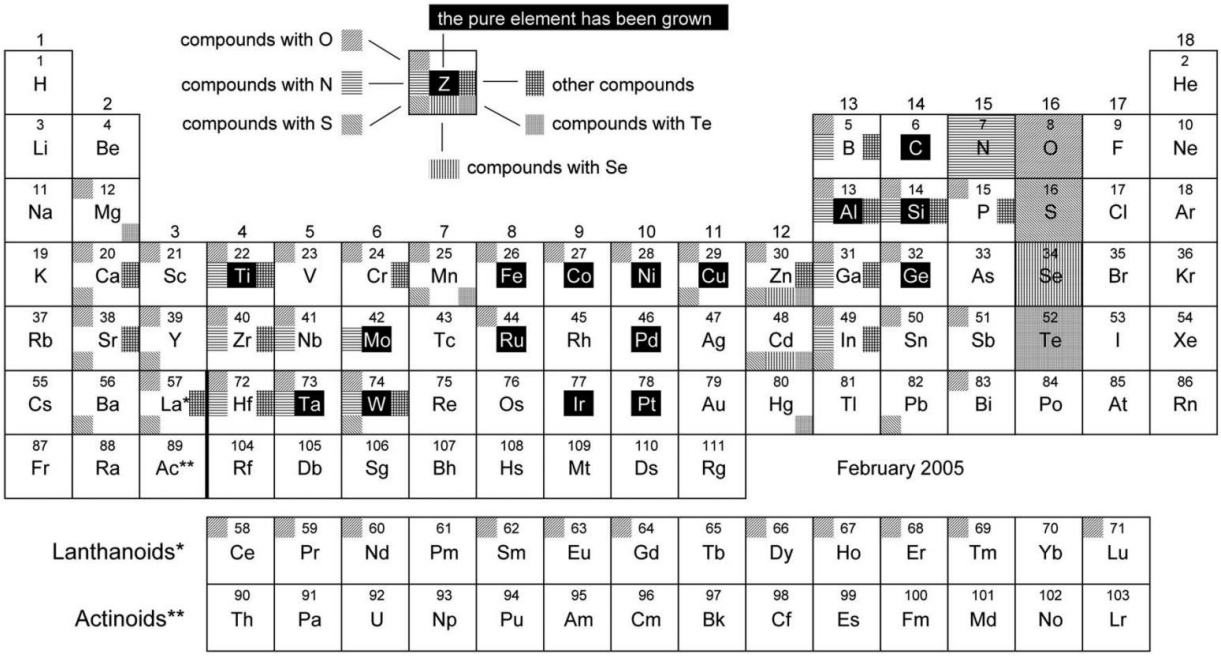

Figure 1.4. Overview of the materials grown by ALD. The growth of pure elements as well as compounds with O, N, S, Se, Te, and other compounds grouped together are indicated through different shadings at different positions (refer to the key at the top of the figure). Reproduced from reference 79.

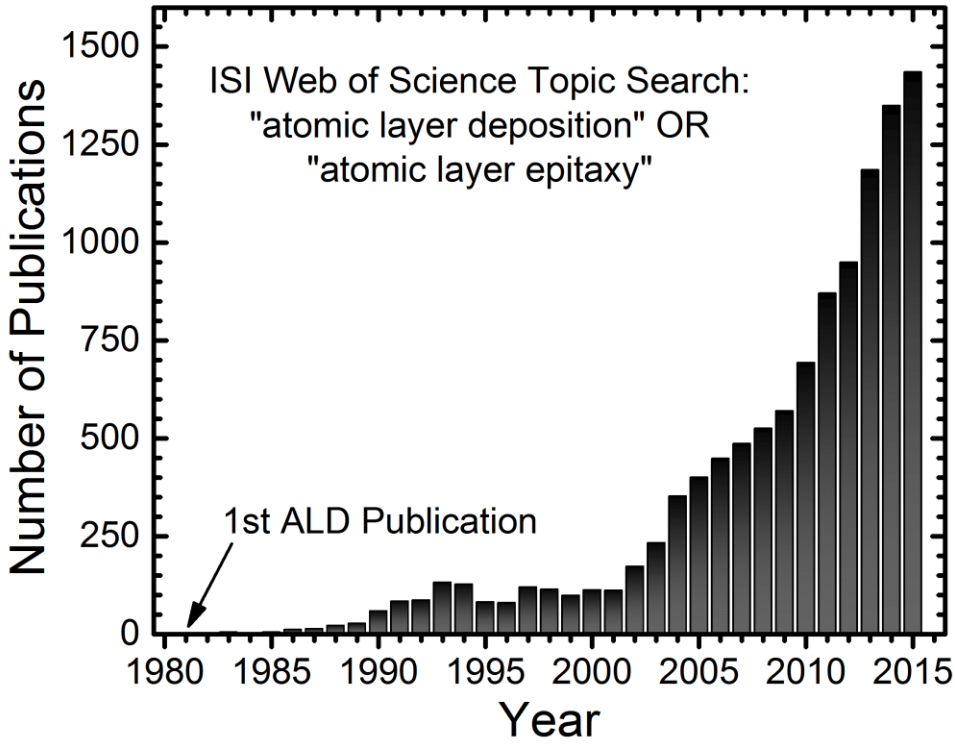

Figure 1.5. The number of publications per year that contain either the phrase “atomic layer deposition” or “atomic layer epitaxy” in the topic, according to the ISI Web of Science. The first such publication came in 1981.

Chapter 2. Instrumentation

Adsorption calorimetry is the measurement of the heat evolved upon adsorption. It is a surface science technique and as such is preferably performed under the clean conditions of ultrahigh vacuum (UHV) to maintain a surface free of foreign species that could adsorb from background gases.

The experiments described in Chapters 3 and 4 of this work have been carried out using an instrument described in detail by Stuckless et al. in a 1998 article published in *Review of Scientific Instruments.*[94] The instrument and sample platens described there were modified for studying thin films of organic materials deposited from solution as described by Diaz et al.[27] In this section, I will briefly describe the adsorption calorimetry technique, the instrument used and its recent modifications.

In our approach, a pulse of metal gas atoms from a 4 mm diameter atomic beam of metal vapor strikes the sample's surface, which is mounted in a UHV surface analysis chamber. The heat released from the exothermic adsorption of a gas pulse onto the sample induces a small temperature rise in the surface, which in turn causes a voltage response from a thin pyroelectric polymer upon which the sample material has been coated, as described below.

The adsorption calorimeter is housed within a UHV chamber with a base pressure below 5×10^{-10} mbar. The chamber is divided into two planes—a lower stage for metal film growth and calorimetry, and an upper plane for surface analysis. The calorimetry plane contains the calorimeter, collimated atomic beam, quartz crystal microbalance (QCM), quadrupole mass spectrometer (QMS), tantalum flag, mirror, and BaF_2 window. The surface analysis plane contains a hemispherical energy analyzer, ion gun for surface sputtering and low energy He^+ ion scattering spectroscopy (LEIS), electron gun for Auger electron spectroscopy (AES), and Al/Mg Kα dual

anode X-ray source for X-ray photoelectron spectroscopy (XPS). These spectroscopies are used to perform compositional analyses of the surface and near subsurface at discrete stages of the experimental process, as well as to check for sample contamination and impurities prior to experiment.

For heat detection, the calorimeter utilizes 28 μm thick β-polyvinylidene fluoride (PVDF), a pyroelectric polymer which is pre-coated on each side with 70 nm Cu and topped with 10 nm Ni for electrical contacts. which is capable of measuring temperature changes of less than 1 mK (purchased from Measurement Specialties).[27] The PVDF is cut into ~1.3 cm diameter disks from large sheets using ceramic scissors to prevent electrically shorting the two electrodes. The heat detector disks are mounted onto sample platens specially designed such that the front and back contacts are electrically isolated from each other by a ceramic bushing, and fixed in place by a thin copper washer with an 8-mm diameter hole, exposing the sample for adsorption (see **Figure 2.1**). An aluminum cup bushing sits within the ceramic bushing and is held in place with a stainless steel bolt which extends from the back of the platen, to serve as the back electrical contact, while the rest of the platen acts as the front contact. Solutions are directly spincoated or dropcast onto the platens, and any built-up material on the platens is carefully removed to prevent excessive outgassing under vacuum. The top copper washer has been modified by beveling the edge of the central hole at a 45° angle to prevent pooling of extra solution on the platen during spincoating.[95] This simple modification resulted in much more uniform and repeatable spincoated thin films. The reflectivity at the HeNe laser wavelength (632.8 nm) of the coated samples is measured *ex situ* using an integrating sphere. (These are representative samples and are not used for experiments in vacuum as they may become contaminated during the process, but they are prepared in the same manner.)

Up to 11 samples are prepared in a nitrogen glovebox and placed inside a specially designed sample transfer suitcase. This suitcase is equipped with a gate valve and a translatable sample carousel with a differentially-pumped linear motion feedthrough for facile sample selection under vacuum. The remaining solvent is typically removed by gently baking the suitcase overnight, after which samples are transferred to the analysis chamber as needed.

With a sample in place in the calorimetry stage, the metal of interest is dosed onto the surface using the pulsed atomic beam with a pulse length of 100 ms and a frequency of 0.5 Hz. The beam is collimated by a series of two apertures which produce a deposition spot 4.15 mm in diameter, and the flux is measured using the QCM. Each pulse deposits heat into the sample, resulting in a very small temperature change which is measured as a transient voltage rise across the PVDF detector. The sticking probability is measured simultaneously with a modified version of the King and Wells method[94] using a line-of-sight QMS positioned at a polar angle of 35° (known as the "magic angle")[96] from the surface normal to measure the fraction of metal atoms which strike the surface but do not stick. (By placing the ion source of the QMS at the "magic angle," i.e. ϕ, in relation to the sample surface, we can minimize the error associated with variations in the angular distribution of the desorbate, which can range widely from a simple $\cos^1\phi$ to $\cos^9\phi$, depending on the desorbate.) A metal grid positioned between the QMS and the sample was biased at -500 V to prevent electron damage from filament emission. The sticking fraction is calibrated by temperature-programmed desorption (TPD) of known amounts of the metal atoms off the Ta flag. We measure the flux repeatedly to confirm the flux does not change over time. The measured heats are calibrated using a HeNe laser of known power (which we measure to confirm the power has stabilized at the known value before each experiment), which is directed down the beam path and pulsed onto the sample surface before and after calorimetry. Contributions to the heat signal

due to line-of-sight infrared radiation from the beam source can be subtracted by measuring this radiation alone by translating a BaF_2 window between the source and the sample. This window physically blocks the impinging atoms from reaching the sample surface, but passes nearly all the radiation (BaF_2 has a transmittance of ~92% in the relevant range of source temperatures). The cleanliness of the BaF_2 window is routinely checked by pulsing the laser through the window onto the sample and comparing to the unobstructed laser pulses. Changes in reflectivity are determined by comparing the magnitude of the heat signal from HeNe laser pulses before and after deposition. Finally, the differential heats of adsorption are determined from the magnitude of the beam and laser calorimeter responses, and the sticking fraction.

Surface analysis techniques allow us to perform complementary experiments which are crucial to understanding the calorimetric results. The growth mode of metal on the sample surface is determined by LEIS using He^+ ions with a primary energy of 1 keV. Because He^+ ions have a small mass the probability of penetrating into the sample surface below the topmost layer is exceedingly small, and even when this does happen the probability of deionization is near 100%.[97,98] Indeed, a large percentage of the He+ ions are neutralized by the sample surface, rendering them undetectable by our energy analyzer (which can only detect charged particles), but those ions that do deflect off the surface carry important information; that is, their remaining *energy* (necessarily below 1 keV) is dictated by the mass of the surface atom involved in the collision process. Therefore, He^+ LEIS is sensitive to only the topmost atomic layer of the solid surface and can tell us the nature of metal film growth on the surface. We use XPS to confirm the composition of the material under investigation and look for any remaining traces of residual solvent which may affect the heats of adsorption. More importantly, XPS provides us with information about the chemical state atoms of the surface and near subsurface. For example, as the

metal atom coverage increases, we look for changes in the centroid binding energy or the width of elemental peaks (such as C 1s and Ca 2p), as this provides evidence of reactions and electron donation/withdrawal by the growing metal surface.

As originally designed, this instrument was the first ever single crystal adsorption calorimeter (SCAC) to utilize PVDF as a heat detector.[94,99] In that form it has published numerous high impact papers of metal adsorption on metal oxides and single crystal surfaces.[100-113] It has inspired additional SCAC instruments designed by our group for studies of catalytic intermediates[114] and low vapor pressure metals[115] on single crystal and metal oxide surfaces, as well as other groups around the world for studying gas adsorption on nanoparticles[116] and electrochemical systems.[117] In its current incarnation it is the only instrument in the world capable of measuring heats of adsorption of vaporous materials onto thin solution-processed films. It has produced a number of studies of metal adsorption on organic films relevant to organic electronics, optoelectronics, and semiconductors[22-30,95,118,119] as discussed above and in Chapter 3. It was again applied to a new frontier in adsorption calorimetry, producing the world's first study of metal vapor adsorption calorimetry on a MOF, as discussed in Chapter 4. It has since been used to study metal adsorption onto layered calcium niobate perovskites for catalysis by my successor on the instrument, Wei Zhang, in collaboration with Prof. Thomas E. Mallouk at Penn State University.[120-122] As evidenced by these repeated forays into entirely new and exciting fields, it is very likely this instrument will be productive for years to come.

Drawing on our group's expertise in UHV adsorption calorimetry, we developed and implemented a novel adsorption calorimeter in collaboration with Alex B. F. Martinson's powerhouse ALD group at Argonne National Laboratory in Argonne, IL. This calorimeter was designed specifically to measure the adsorption of ALD precursors in porous materials in thermal

equilibrium with a pyroelectric $LiTaO_3$ detector surface, as the high surface area of the porous material would increase the overall surface area for adsorption by multiple orders of magnitude, thus increasing the overall heat available to measure. However, during initial tests we found the calorimeter was sensitive enough to measure the heats of adsorption of precursors directly on the detector! This finding vastly expanded the applicability of the device, and we decided to refocus our interest on more fundamental studies, such as Al_2O_3 ALD *via* alternating exposure of surfaces to TMA and H_2O vapor.

A simplified schematic of the ALD calorimeter is shown in **Figure 2.2**. The pyroelectric heat detector is a 50 μm thick $LiTaO_3$ crystal coated on both sides with ~25 nm of gold (Del Mar Photonics). The crystal rests on a stainless steel stand with a spot-welded signal wire. The stand has a hole bored out through its center to reduce its thermal mass. A large thermal mass acts as heat sink for the calorimeter, reducing the signal intensity. The stand is electrically isolated from the rest of the calorimeter fixture by the $LiTaO_3$ crystal on top and a 2.54 cm diameter Macor ceramic disk below. The roughness of the Macor disk allows for trapped gases within the stand to be pumped out gradually, avoiding a large pressure differential across the faces of the brittle crystal, while simultaneously making diffusion of ALD precursor gases to the back face of the detector crystal very slow, so we interpret the heats as being associated with the front surface area. All three pieces are sandwiched between a circular base and annular top constructed of aluminum which are connected together using three screws separated radially by 120°. The top piece has a central 8.66 mm diameter orifice which exposes the $LiTaO_3$ crystal to gases in the ALD chamber. The top face of the crystal is grounded to the chamber through the aluminum housing.

The measured voltage signal is fed from the vacuum side to atmosphere by a KF-to-BNC feedthrough just downstream of the sample chamber, shown in **Figure 2.3**. The measured signal

is amplified by a homebuilt preamplifier with very low input noise, an input impedance of >10 GΩ, and a gain of 100, followed by an amplifier with adjustable settings for the polarity, time constant (τ = 0.5, 5, and 25 s), and gain (1-1000). The 25 s time constant was used for all experiments. These electronics are similar to those previously reported to measure heats of adsorption of metals and molecules on various surfaces in ultrahigh vacuum.[94,99,114,115]

Though the focus in Chapter 5 is on the TMA–H_2O reaction to produce Al_2O_3, we also present some interesting findings, which highlight the calorimeter's remarkable sensitivity, for the following ALD precursors with H_2O vapor: tetrakis(dimethylamino)titanium (TDMAT) and bis(ethylcyclopentadienyl)manganese (ECPDM) to produce TiO_2 and MnO, respectively. As discussed at the end of Chapter 5, there are many interesting systems to be investigated using this calorimeter, including extended studies of the above systems, ALD in MOFs,[85] and thin films of other non-conductive oxides, sulfides, nitrides, etc.[79] Thus, this new ALD calorimeter has the capacity to be very productive in the future.

FIGURES

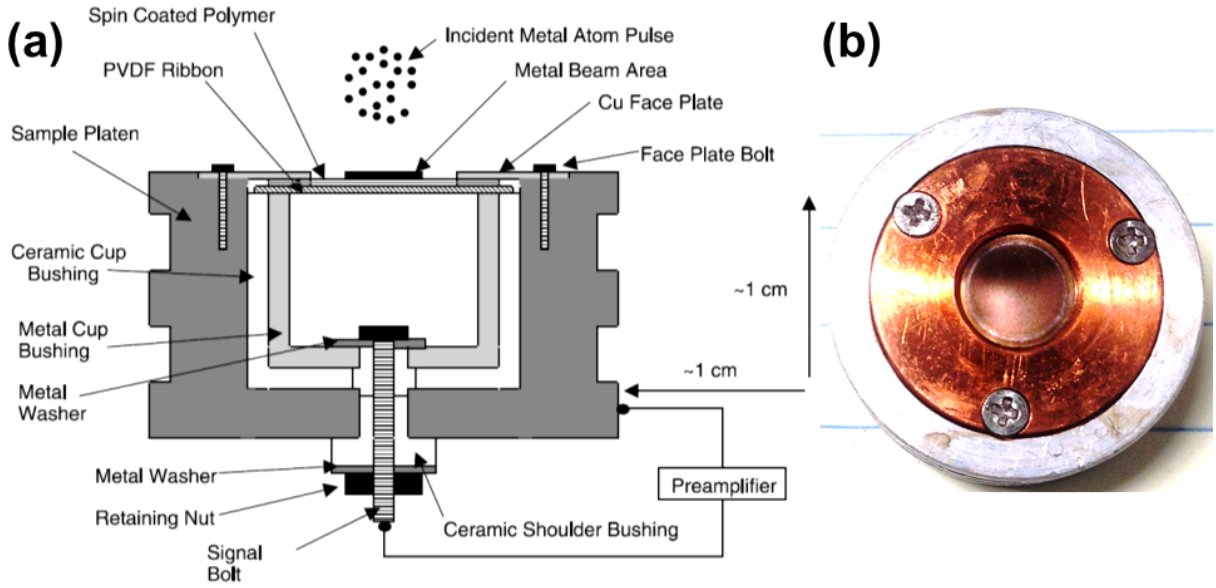

Figure 2.1. (a) Adsorption calorimeter's heat detector for spin-coated polymer and organic samples mounted in a transferrable platen. The entire sample platen is circularly symmetric aside from the face-plate bolts when viewed from above or below. A circular cut-out of β-PVDF precoated on both sides with 70 nm of Cu and topped with 10 nm of Ni for electrical contacts serves as the heat detector. It is clamped between a Cu annular disk (with a beveled inner edge, not shown) and a metal cup bushing (light grey). The metal cup bushing is held in the ceramic cup bushing by a bolt which is isolated from the sample holder (dark grey) and is used as an electrical contact. Thus, the front and back face of the PVDF are electrically isolated from each other and the signal bolt and sample holder act as the electrical leads to the preamplifier. A solution of PCBM in chloroform was directly spincoated onto the detector under nitrogen environment. This produced an ~8-mm diameter area of uniform thickness in the center of the sample platen. In the UHV analysis chamber, a 4-mm diameter area centered on the front face is irradiated by Ca metal pulses from the molecular beam, creating a face-to-face voltage difference across the PVDF film. Reproduced from reference 27. (b) Top face of the sample platen with a spincoated PCBM thin film on PVDF.

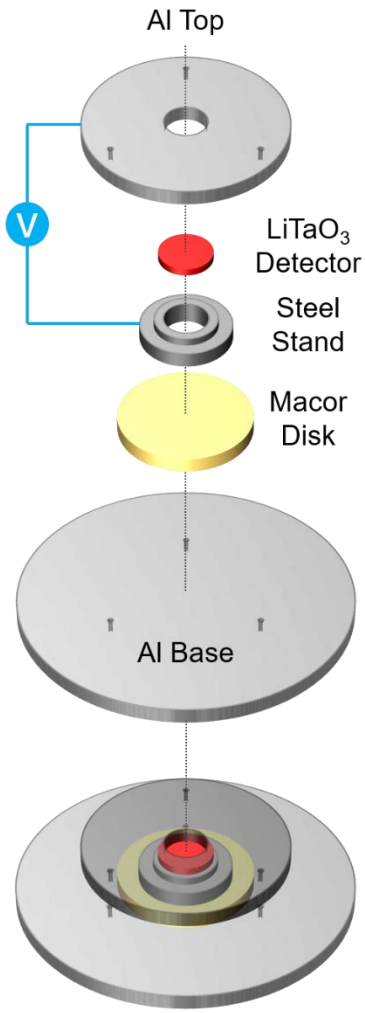

Figure 2.2. ALD calorimeter at 45° perspective. The heat detector (red) is a 50 µm thick $LiTaO_3$ crystal coated on both sides with 25 nm of chromium metal. The detector is placed on top of a stainless steel stand with a spot-welded signal wire (blue). The stand is electrically isolated from the rest of the calorimeter housing by the $LiTaO_3$ crystal and a 2.54 cm diameter Macor ceramic disk (yellow). The above pieces are sandwiched between a circular base and annular top constructed of aluminum which are connected, physically and electrically, using three screws separated radially by 120° (not shown). The top piece has an 8.66 mm diameter orifice in the center which exposes the $LiTaO_3$ crystal to gases in the ALD chamber. The top face of the $LiTaO_3$ crystal is grounded to the chamber through the aluminum housing, and this is used as the reference signal.

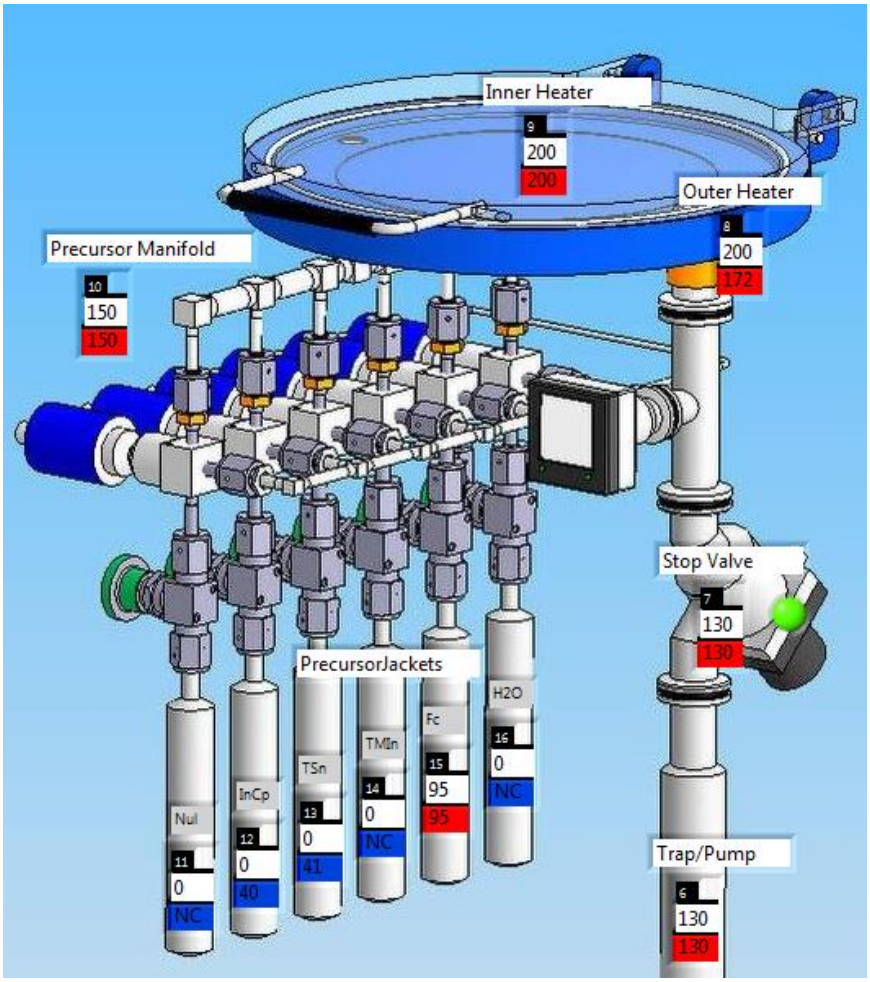

Figure 2.3. Diagram of the Savannah S200 ALD system in which the ALD calorimeter was mounted. Up to six precursor canisters (with a corresponding manual valve) can be attached the chamber at a time. Each precursor canister has its own corresponding computer-controlled three-way actuator valve. When the actuator valve is closed, only N_2 flows through to the chamber. When the actuator valve opens, the ALD precursor gas is swept up into the N_2 flow. The reaction chamber has a single inlet and outlet and the lid can either be equipped with two QCMs (one each near the inlet and outlet) or a window for shining a light into the chamber for calibration. A pressure gauge is attached near the outlet. Separate PID-controlled heaters control the temperature of the precursor canisters, precursor manifold that leads to the reaction chamber, outer region of the reaction chamber, inner region of the reaction chamber, stop valve, and pumping trap. The ALD calorimeter described in **Figure 2.2** is situated in the center of the reaction chamber, midway between the two QCMs (or beneath the window), with electrical leads extending down to a KF-to-BNC feedthrough attached the outlet tubulation.

Chapter 3. Calcium Thin Film Growth on Phenyl-C_{61}-Butyric Acid Methyl Ester: Interface Structure and Energetics

This chapter is reprinted with permission from reference 95: J. M. Lownsbury, J. C. Sharp, E. J. Mann, C. T. Campbell, Calcium Thin Film Growth on Phenyl-C_{61}-Butyric Acid Methyl Ester (PCBM): Interface Structure and Energetics, *Journal of Physical Chemistry C* **2015**, *119*, 18444-18451.

CHAPTER ABSTRACT

The adsorption of Ca vapor on phenyl-C_{61}-butyric acid methyl ester (PCBM) at 300 K has been studied by X-ray photoelectron spectroscopy (XPS), low energy He^+ ion scattering spectroscopy (LEIS), adsorption microcalorimetry, and atomic beam/surface scattering. This interface commonly occurs in some of the highest efficiency organic solar cells. It is found that over 10 nm of the PCBM undergoes aggressive reaction with the Ca vapor to make the Ca carboxylate of PCBM. This thick reacted layer, which was not previously known to be present, lies at the interface between the metallic Ca film and PCBM, and is expected to influence charge transfer across that interface during photovoltaic operation. The heat of Ca adsorption is very high below 0.03 ML (800-850 kJ/mol), due to reaction of Ca with impurities. Between 0.05 and 0.4 ML, the heat of adsorption is 624 kJ/mol and nearly constant. This heat is assigned to the reaction of Ca with subsurface methyl ester groups to form the Ca carboxylate of PCBM. This assignment is supported by the shift of the O 1s XPS peak of PCBM toward lower binding energy (BE) due to this reaction with Ca, and the absence of Ca LEIS signal, below 0.4 ML coverage. Conversely, the C 1s XPS peak shifts toward higher BE due to downward band bending. Beyond 0.4 ML, the heat of adsorption decreases nearly exponentially to the sublimation enthalpy of Ca (178 kJ/mol) by 3 ML, attributed to the formation of Ca(solid) nanoparticles on the surface and eventually a

continuous Ca film. This model is supported by LEIS. Impinging Ca atoms face a kinetic competition between diffusing subsurface to react with methyl ester groups of PCBM and the formation and growth of three-dimensional Ca clusters on the surface. The total extent of reaction of Ca with subsurface ester groups to make the Ca carboxylate of PCBM is equivalent to ~14 layers of reacted PCBM molecules, or ~13 nm of reacted depth.

INTRODUCTION

Interfaces between metals and semiconducting, π-conjugated polymers and fullerenes play an important role in organic electronic devices, such as organic photovoltaics (OPV),[16,123] light-emitting diodes,[14] and field effect transistors.[124,125] Organic solar cells are typically produced from solution by spin-coating a mixture of an electron-donating polymer and an electron-accepting fullerene to form a donor/acceptor bulk heterojunction (D/A BHJ).[12] In conventional device configurations, this active layer is sandwiched between a transparent conducting oxide anode and a low work function metal cathode. One of the best performing model systems for OPV applications is poly(3-hexylthiophene) (P3HT) and phenyl-C_{61}-butyric acid methyl ester (PCBM),[31,126] which can produce devices with power conversion efficiencies (PCE) in excess of 5%[39] with optically thick active layers capable of absorbing >90% of incident light.[32,127] Low work function metal cathodes such as Ca are commonly used in devices due to the formation of an ohmic contact with the LUMO of PCBM, leading to high open-circuit voltages (V_{OC}) and fill factors (FF).[38,39] In recent years, single-junction OPV devices have approached and surpassed 10% PCE[7,37] due to the use of charge selective interfacial layers,[15] inverted device structures,[128] the use of solvent additives,[129] and the development of novel low band gap polymers and block

copolymers,[130,131] but nearly all such devices remain reliant on fullerenes to shuttle free electrons via percolation pathways in the semicrystalline polymer matrix to the cathode where they are harvested.[32-35] After nearly two decades of research into new n-type molecules/polymers to replace PCBM, it remains the best choice for high performing D/A OPV devices.[37] Thus, understanding the interfaces of low-work-function metals like Ca with functionalized fullerenes like PCBM is essential to understanding device performance and stability.

Here, we study the structure of the Ca/PCBM interface and its bonding energetics as Ca is vapor deposited onto a clean PCBM surface in ultrahigh vacuum using surface spectroscopies, atomic beam/surface scattering and adsorption calorimetry. We clarify the structural details of this interface and the morphology of the evolving Ca film using X-ray photoelectron spectroscopy (XPS) and low energy He^+ ion scattering spectroscopy (LEIS). Simultaneous measurement of the heat of adsorption and sticking probability of the metal atoms as a function of coverage provides the first interfacial bonding energies for Ca on PCBM. These results reveal a tendency for the Ca metal to diffuse subsurface and react with oxygen atoms in the methyl ester of PCBM to make the Ca carboxylate, in kinetic competition with Ca(solid) particle nucleation and growth, and eventually Ca(s) film growth across the fullerene surface. Over 10 nm of the PCBM is destroyed by aggressive reaction with the Ca vapor to make the Ca carboxylate of PCBM. This thick reacted layer at the interface between the metallic Ca film and PCBM surely influences charge transfer across this interface during photovoltaic operation. Previous investigations of Ca vapor adsorption onto P3HT yielded strong evidence of Ca atom diffusion subsurface where it abstracts sulfur heteroatoms from the thiophene backbone down to ~3 nm below the surface to make CaS clusters.[22,23]

To our knowledge, no other studies have been reported of the evolving Ca/PCBM interface using any surface spectroscopies or adsorption calorimetry. The XPS spectrum of a clean PCBM surface was reported by Guan et al.[132] XPS studies of vapor deposited Al and LiF on PCBM thin films by van Gennip et al.[133] concluded that Al reacted exclusively with the methyl ester oxygen group in PCBM, while LiF acted as a barrier between the organic film and the impinging Al metal. Studies of Ca growth on poly(methyl methacrylate) (PMMA) have concluded that Ca reacts with the methyl ester group in the repeat unit of the polymer and bridges across two lamellar layers to form the Ca carboxylate.[28-30]

EXPERIMENTAL

The PCBM used in this study was purchased from American Dye Source with >99.5% purity and was used as received (see inset in **Figure 3.1** for structure). Thin films were prepared by spin-coating a PCBM solution in chloroform (1 wt%) directly onto the heat detector, a metal-coated foil of the pyroelectric polymer β-polyvinylidene fluoride (PVDF, see below). Two 30 μL aliquots were spin-coated at 1500 rpm for 60 s to yield uniform films ~90 nm thick. The film thickness was determined by preparing samples on glass substrates in the same manner, removing some of the film with a razor blade and measuring the film height with a profilometer. Up to 10 samples at a time were transferred from the glovebox to the sample transfer chamber *via* a stainless steel "suitcase" equipped with a gate valve. Once attached to the transfer chamber, it was evacuated to its base pressure of 2×10^{-9} Torr and heated at 330 K for ~10 h to outgas the samples and remove trace solvent. The samples were then transferred into the ultrahigh vacuum chamber (UHV) analysis chamber as needed. No remaining solvent was detected with XPS.

The surface analysis chamber and pulsed metal atom beam have been described previously.[94] Briefly, the UHV chamber used for these experiments had a base pressure of 5 x 10^{-10} mbar and was equipped with a hemispherical energy analyzer (Leybold-Heraeus EA 11/100) for LEIS and XPS, ion gun (Leybold-Heraeus IQE 12/38), Mg and Al Kα dual anode X-ray source (VG Scienta XR3E2), quartz crystal microbalance (QCM, Inficon), quadrupole mass spectrometer (QMS, UTI 100C), and adsorption microcalorimeter. The Ca atom beam was chopped into 100 ms long pulses containing 0.009 monolayers (ML) of Ca at a rate of 0.5 Hz. One ML of Ca is defined here as 7.4 x 10^{14} atoms per cm^2, which is the packing density of the Ca(111) crystal face. The heat detectors were ~1.3 cm diameter disks cut from 28 μm thick sheets of PVDF, precoated on each side with 70 nm Cu and topped with 10 nm Ni for electrical contacts (purchased from Measurement Specialties). These heat detector disks were mounted onto sample platens specially designed such that the front and back contacts are electrically isolated from each other by a ceramic bushing, and fixed in place by a thin copper washer, as described elsewhere.[27] The copper washers were modified by beveling the edges of the central hole to prevent pooling of extra solution on the platen during spin-coating. PCBM was directly spin-coated onto these platens, and any built-up material on the platens was carefully removed to prevent excessive outgassing under vacuum.

The sticking probability for Ca on PCBM was determined using the QMS with the modified King-Wells method described previously.[94,96] A metal grid positioned between the QMS and the sample was biased at -500 V to prevent damage to the samples from electrons emitted by the QMS filaments.

The growth of Ca on PCBM was studied by LEIS using He^+ ions with a primary energy of 1 keV and an angle of 45° between the ion gun and analyzer axes (i.e. 135° scattering angle). Ion fluxes were typically 15 nA/cm^2 and the sample was exposed to the He^+ beam for only 30 s to get

a full spectrum at each coverage. For XPS experiments, 260 W Al Kα X-rays (hν = 1486.6 eV) were used and the spectra were referenced to the Cu $2p_{3/2}$ peak measured at a solid Cu part of the sample platen.

RESULTS

Sticking Probability

The amount of Ca which actually adsorbs on the PCBM surface must be known in order to determine the true Ca coverage from the Ca flux, and to convert heats of adsorption and reaction measured by microcalorimetry into units of kJ *per mole adsorbed*. **Figure 3.1** shows the sticking probability of Ca atoms as a function of Ca coverage on PCBM at 300 K. The flux of the Ca atom beam was measured with the calibrated QCM. Coverage was determined by time-integrating the product of the Ca flux and the sticking probability. The fraction of Ca atoms that do not stick on the PCBM surface are either scattered quasi-elastically or are transiently physisorbed before desorbing again. The line shape of the mass spectrometer signal versus time indicates that the nonsticking Ca atoms have a surface residence time shorter than 10 ms, and thus make no contribution to the heat of adsorption if they transiently adsorb (as they probably do, see below). We do assume they change kinetic energy to that characteristic of a Maxwell-Boltzmann distribution of gas atoms at the surface temperature (which is colder than the hot incident beam), and subtract that energy difference from the measured heat, as described previously.[94]

The sticking probability of Ca on PCBM is initially ~0.3, drops quickly to 0.18 at 0.4 ML, and then increases slowly and asymptotically toward unity. The initial transiently high sticking probability could be explained by the presence of just 5% of a ML of species near the surface which have unit sticking probability but are quickly titrated by Ca, with the vast majority of the

PCBM surface having a sticking probability of just 0.18 initially. We discuss below that these special species with high sticking probability could be the ester groups nearest to the surface (whose oxygen atoms correspond to just 3% of the total O+C count in PCBM) and/or impurities in the film near the surface (such as residual solvent or water).

Low-Energy Ion Scattering Spectroscopy

LEIS with He^+ ions is a valuable technique for determining the mechanism of film growth because it is element-specific and probes only the topmost atomic layer.[97] **Figure 3.2** shows the evolution of the normalized Ca LEIS signal on PCBM as a function of Ca coverage, with the inset depicting the low coverage region in more detail. Effects of beam damage by the He^+ ions were determined to be negligible by comparing this signal intensity versus coverage to a control experiment (square points), which exposed the surface to ~8 times fewer ions but yielded identical results within the data scatter. (The ion dose for the more frequent round points totaled ~4 $\mu C/cm^2$ for the points up to 2 ML coverage.) As seen, the Ca signal grows much more slowly with Ca coverage than predicted by a layer-by-layer growth model and even more slowly than on several heteroatom-containing polymers we investigated previously,[22,25,28] although it is notably similar to the Ca signal growth on polyfluorenes PDHF and PDHFV, neither of which contain heteroatoms.[26] In general, this very slow growth of Ca LEIS signal in those cases was due to a combination of (1) Ca diffusing below the surface and reacting with subsurface groups containing heteroatoms with a high heat of reaction, followed by (2) Ca atoms nucleating clusters of Ca(s) on the surface, which grow into thick 3D particles that cover only a small fraction of the surface initially. This second step has a heat of adsorption very similar to the heat of sublimation of bulk Ca(s), 178 kJ/mol.[134] The XPS and heat data presented below show a very similar situation as obtained here: Initially,

Ca diffuses below the surface and binds mainly to ester groups on PCBM. This is followed by the nucleation of 3D Ca(s) islands on the surface, which then grow in size and eventually cover the entire surface.

X-Ray Photoelectron Spectroscopy

Measuring the XPS spectra of PCBM at intervals as Ca is deposited on the surface gives valuable information regarding the chemical state of the evolving surface. **Figure 3.3** shows XPS spectra of the C 1s (left) and O 1s (right) regions of the clean PCBM surface (top) and the PCBM surface with increasing Ca coverage (bottom). All XPS spectra were measured using Al Kα X-rays (1486.6 eV) at 190 eV pass energy, and peak positions are referenced to the ISO standard binding energy (BE) peak position of the Cu $2p_{3/2}$ peak (932.62 eV[135]) measured from the Cu face plate of the sample platen. **Figure 3.3a** shows the C 1s region of pristine PCBM decomposed into five component peaks as shown, following peak position and intensity ratios reported by Richter et al.[136] This gives the following peaks from low to high BE: the component peak at 284.9 eV corresponds to the conjugated C atoms of the C_{60} fullerene and phenyl group, by far the dominant C species in PCBM (80.0% of combined C 1s peak area); the component at 285.7 eV is assigned to the saturated C atoms of the butyl chain (7.3%); the component at 286.8 eV corresponds to methoxy C of the methyl ester group (-O-CH_3, 4.4%); the component at 288.9 eV is assigned to carbonyl C from the methyl ester (4.4%); and the component at 290.8 eV is a broad C 1s shake-up peak (3.8%).

The O 1s spectrum is decomposed into two component peaks pertaining to the methyl ester group, as shown in **Figure 3.3c**. The component at 533.3 eV corresponds to methoxy O (C-O-CH_3) and the component at 531.8 eV corresponds to carbonyl O (>C=O), each 50% of the total O

in PCBM. These peak positions are consistent with findings from XPS studies of PMMA and other materials containing methyl ester groups.[137] The relative C 1s and O 1s peak areas in this clean PCBM surface is 12:1 which compares well to XPS results obtained by the Kahn group on pure PCBM films.[132] The theoretical C:O ratio in bulk PCBM is 36:1. The lower ratio in the XPS spectra shows that PCBM preferentially orients with its methyl ester group closer to the surface. The inelastic mean free path of a C 1s electron through a PCBM film is ~3.14 nm (estimated using the TPP-2M equation;[138] the mean free path through C_{60} is ~3 nm[139]). The thickness of one layer of PCBM is ~0.92 nm. This was estimated by assuming the PCBM molecules are spherical and arranged in FCC packing, and using the interlayer spacing between the nearest <111> planes of spheres. A number density of 10^{21} PCBM molecules per cm^3 was used, corresponding to a bulk density of ~1.51 g/cm^3 which is within the range of reported values for PCBM.[140,141] PMMA, a polymer that contains methyl esters like PCBM, has been shown to spontaneously orient its methyl ester side chains toward the bulk under vacuum in order to minimize its surface energy,[18] though the orientation of PCBM is likely dictated by the C_{60} group rather than the methyl ester.

Figure 3.3b and **d** show the evolution of the C 1s and O 1s spectra, respectively, with increasing Ca coverage, from pristine to 5 ML coverage. With small Ca doses, the O 1s peak loses intensity on the high BE side, due to the selective removal of the C-O-C component. This causes a peak narrowing and shift of its centroid to lower BE, as summarized qualitatively in **Figure 3.4**, which depicts (a) the centroid BE shift and (b) the evolution of the full-width at half maximum (FWHM) of the C 1s and O 1s peaks as a function of Ca coverage. The addition of Ca also causes growth in intensity on the low BE side of the O 1s peak, consistent with the growth of a new component centered at ~531 eV BE. These same two effects were observed upon Ca adsorption onto PMMA, and shown to be due to Ca reacting with its subsurface methyl ester groups to make

its Ca carboxylate, presumably releasing the methyl groups as ethane gas.[28-30] We attribute these same changes in the O 1s lineshape upon Ca adsorption on PCBM to this same reaction with the ester groups of PCBM to make its Ca carboxylate and release its methyls as ethane gas. We show below that the extent of this reaction is so large that it involves ester groups down to a depth of ~13 nm below the surface. The XPS intensities of the C 1s and O 1s peaks are attenuated by 18% at 5 ML Ca coverage. If Ca(s) grew as a uniformly-thick film on the surface instead of as 3D particles, a film thickness of ~1.8 ML would be required to cause this 18% attenuation, only ~36% of the actual 5 ML thickness. This result is consistent with LEIS, suggesting growth of thick 3D Ca particles covering only a small fraction of the surface.

As shown in **Figure 3.4a**, the C 1s peak shifts toward higher BE a total of 0.35 eV as the Ca film is deposited, with 0.15 eV of this shift occurring in the first 0.2 ML. This is attributed to simple Ca-induced band bending, arising from the long-range transfer of electron density from Ca to the bulk of the PCBM film, causing the PCBM bands to bend downward near the surface due to the development of this long-range dipole. A very similar effect was reported for Ca adsorption on semiconducting polymers.[22,25,142] The O 1s peak also shifts considerably, but toward lower BE instead. This is clearly due to the conversion of the methyl ester groups to Ca carboxylates mentioned above, which has a stronger effect on O 1s BEs than band bending, which would also affect the O 1s BEs for any unreacted components of the PCBM in the same way as it does the C 1s BEs.

Heats of Adsorption

Figure 3.5 shows the differential heat of adsorption of Ca on PCBM as a function of coverage, averaged over three experimental runs at 300 K. The pulse-to-pulse standard deviation of the heats

of adsorption at high coverages, where the heat is independent of coverage, is less than 3 kJ/mol for pulses of ~0.009 ML. The heat of adsorption in the limit of zero coverage is ~880 kJ/mol. The heat drops quickly with Ca coverage to ~624 kJ/mol by 0.05 ML, then remains constant until 0.4 ML coverage, and thereafter decays exponentially toward the bulk heat of sublimation of solid calcium (178 kJ/mol[134]).

DISCUSSION

The experimental results can be summarized as follows:

a. The heat of Ca adsorption on PCBM at low coverages (<0.5 ML) is very high (~880 kJ/mol in the limit of zero coverage, ~624 kJ/mol from 0.05-0.4 ML) and much greater than the bulk heat of Ca sublimation (178 kJ/mol).
b. The heat of Ca adsorption approaches the bulk heat of Ca sublimation by ~3 ML.
c. The Ca LEIS intensity increases much more slowly with Ca coverage than is predicted by a layer-by-layer growth model, reaching complete layer coverage by ~30 ML.
d. The C 1s XPS peak shifts to higher BE with increasing Ca coverage while the O 1s peak shifts to lower BE.

In the following, we will describe a model for the formation of the Ca/PCBM interface which is consistent with these results.

As shown in **Figure 3.2**, the Ca LEIS signal grows much more slowly with Ca coverage than expected for layer-by-layer growth or the formation of a continuous first layer followed by 3D particle growth. The Ca signal intensity at coverages below 0.4 ML is negligible and increases logarithmically toward full coverage at ~30 ML. Instead, the data are consistent with subsurface diffusion of nearly all impinging material at low Ca coverages, followed by a kinetic competition

between subsurface diffusion and 3D island nucleation at the surface. If growth were dictated by 3D island nucleation from the beginning, the measured heats of adsorption should be approximately equal to the bulk heat of Ca sublimation of 178 kJ/mol (or less in the case of small clusters, due to the Kelvin effect). However, the measured heats of adsorption are significantly higher than that at low coverages.

The heat curve is indicative of a three-step mechanism: (I) a very exothermic initial reaction (heat ≥ 880 kJ/mol) which is limited to very few reaction sites (<5% of a ML), followed by (II) a more extensive reaction with a heat of ~624 kJ/mol that persists from 0.05 ML up to >0.4 ML, and finally (III) growth of Ca(s) on the surface with a heat of ~178 kJ/mol. The dominant changes in the XPS spectra which we attributed to Ca carboxylate formation above occurs in the same coverage range where reaction II dominates the heat, so we attribute its 624 kJ/mol heat to this conversion of methyl ester groups to Ca carboxylates.

A similar exponential decay as that seen here between the heats for reactions II and III has always been observed for Ca adsorption on polymers that contain heteroatoms[22,25,28] and we attribute it to the same type of kinetic competition here as was used to explain those data. It thus reflects the decreasing probability for an incoming Ca atom to diffuse further subsurface to find unreacted heteroatoms (ester groups here) and its increasing probability to instead find a growing cluster of Ca(s) to which it attaches. Reaction II gets slower as the reacted thickness increases, and reaction III gets faster as the fraction of the surface covered with Ca(s) increases. The heat for reaction III already dominates strongly by 1 ML coverage, at which point the LEIS data of **Figure 3.2** show that only 5% of the surface is covered by Ca(s). At this coverage, the sticking probability is only 0.3, so that 70% of the Ca atoms desorb again before finding a Ca(s) cluster to which it can

add (or a subsurface ester group to attack). We show below that the ester groups have already been reached down to a depth of ~10 nm at this 1 ML coverage.

We propose that reaction II above, which occurs between Ca and the methyl ester groups of PCBM, is similar to the following reaction:

$$Ca(g) + 2\ R\text{-}COOCH_3(s) \rightarrow (R\text{-}COO)_2Ca(s) + CH_3\text{-}CH_3(g) \qquad (3.1)$$

where R represents the remainder of the PCBM molecule. The standard enthalpy of reaction 3.1 at 298 K ($\Delta H°_{rxn}$) can be estimated using thermodynamic tables of heats of formation,[134,143] for the simplified example where R is replaced with a CH_3 group, and the heat of formation for solid methyl acetate is approximated as that reported for its liquid. This gives the standard enthalpy of reaction 3.1 to be -855 kJ/mol. The heat of adsorption of Ca on PCBM in the coverage range 0.05-0.4 ML is 624 kJ/mol, reasonably close to this reaction's heat. This suggests that the Ca atoms predominantly react in this coverage range to form the Ca carboxylate of PCBM, with two PCBM molecules reacting per Ca atom. As reported previously, the heat of adsorption of Ca on PMMA similarly goes through a long, nearly constant heat regime at low coverages with a heat of 780 kJ/mol that was attributed to Ca reacting predominantly with subsurface methyl ester groups *via* the same reaction shown above (albeit with a different R), to form the Ca carboxylate of PMMA.[28] The heat for this same reaction regime for Ca on PCBM is 156 kJ/mol lower than Ca on PMMA, and 231 kJ/mol lower than for the simplified case of reaction 3.1 when R = CH_3. Since PCBM has far fewer reaction sites (esters) per volume than these other two methyl ester systems, one expects less stable packing of the resulting Ca cations and carboxylate anions in the solid than in the Ca carboxylate of PMMA or in Ca acetate, which may explain these differences in heats.

In the first two Ca pulses, the impinging Ca atoms that stick to the surface react with a higher heat of 800-850 kJ/mol. We attribute this to Ca reacting with remaining chloroform solvent or other impurities in the PCBM film. Although XPS shows no evidence of Cl, the reaction of Ca with chloroform to form $CaCl_2$ solid and acetylene gas would have a heat of 809 kJ/mol. Thus, a small amount of remaining chloroform below the XPS detection limit (when spread through a depth of >10 nm) could explain this high heat. The Ca(g) reaction with water impurity to make $Ca(OH)_2$(s) would give a reaction heat of ~680 kJ/mol.

If we neglect this high initial heat due to impurities, and assume that the heat below 0.05 ML is also equal to 624 kJ/mol as it is from 0.05 ML to 0.4 ML, we may use a simple two-state model to fully explain the heat data in **Figure 3.5**, and from this estimate the extent of reaction by Ca to make the Ca carboxylate of PCBM. This model assumes that the measured heats in **Figure 3.5** have two contributing reactions, one due to reaction II (with heat = 624 kJ/mol), and the other due to formation of Ca(s) (reaction III) with a heat equal to the bulk heat of Ca sublimation (178 kJ/mol). In this model, the measured differential heat of adsorption at any Ca coverage (ΔH_{ad}) is a sum of the fraction of Ca atoms (*f*) in the pulse that reacts via reaction II multiplied by 624 kJ/mol and the remaining fraction (1 - *f*) multiplied by 178 kJ/mol,

$$\Delta H_{ad} = f\left(624\frac{kJ}{mol}\right) + (1-f)\left(178\frac{kJ}{mol}\right) \tag{3.2}$$

Solving for *f* results in a curve identical in shape to the heat curve in **Figure 3.5** except *f* = 1 corresponds to 624 kJ/mol and *f* = 0 corresponds to 178 kJ/mol. Multiplying *f* by the added Ca coverage per pulse gives the amount of reacted Ca per pulse in ML which makes the Ca carboxylate of PCBM. Summing pulses from zero coverage up to any other coverage gives the

total amount of "reacted Ca" at that coverage. This is plotted versus coverage in **Figure 3.6**. As seen, this amount increases with unit slope up to ~0.4 ML, but then flattens out and eventually saturates at a value of 0.85 ML of "reacted Ca" at coverages above 3 ML.

We converted this "reacted Ca" coverage to the effective "reacted depth" by assuming that PCBM molecules pack like spheres in an FCC close-packed crystal, and assuming a number density of 10^{21} PCBM molecules/cm^3, which corresponds to a mass density within the reported range of values for PCBM (1.3-1.631 g/cm^3).[140,141] Using the Ca ML definition of 7.4 x 10^{14} atoms/cm^2 and the reaction stoichiometry of 2 PCBM : 1 Ca atom, we thus calculated the reacted depth of PCBM from the reacted Ca coverage. At saturation, this reaches ~13 nm (~14 layers of PCBM molecules). The progression of this reaction depth with coverage is also shown in **Figure 3.6**.

It is notable that Ca diffuses/reacts much deeper here than for the cases of Ca/P3HT (~3 nm reacted depth),[22] Al/P3HT:PCBM in a 1:1 ratio by weight (~4 nm estimated by high resolution TEM),[17] and Ca/MEH-CN-PPV (~6 nm).[25] This is likely driven by the very small number of reaction sites per unit volume and open diffusion pathways between sphere-like PCBM molecules. PCBM itself has been shown to diffuse through polymer matrices over distances on the order of 100 nm even at low annealing temperatures.[144]

The disparity in diffusion/reaction depth for reactive metals on different organic thin films is relevant for understanding the complex processes of interface formation during device fabrication. Vertical phase separation in P3HT:PCBM BHJ solar cells has been extensively studied and the species which separate toward the cathode interface are dependent on preparation method and interfacial effects.[37] In as-cast P3HT:PCBM blends prepared on PEDOT:PSS, P3HT tends to be more abundant at the air interface due to its relatively lower surface energy.[145,146] Using

variable-angle spectroscopic ellipsometry on P3HT:PCBM blends spincoated on PEDOT:PSS and fused silica, Campoy-Quiles et al.[147] reported a concentration gradient which varies from PCBM-rich at the underlying PEDOT:PSS or fused silica interface to P3HT-rich at the air interface. Solvent vapor annealing was shown to increase PCBM concentration at the air interface of the P3HT:PCBM/PEDOT:PSS films. Chen et al.[17] used SIMS on P3HT:PCBM blends prepared on PEDOT:PSS to confirm that P3HT is more concentrated at the cathode interface in as-spun devices, but found that thermal annealing before or after cathode deposition dictated the cathode interface composition, with this interface becoming enriched in P3HT for devices thermally annealed *before* metal vapor deposition and enriched in PCBM for devices thermally annealed *after* vapor deposition. Since electrons are primarily transported via C_{60}, the reaction of Ca atoms with methyl ester groups in PCBM should have little effect on electron transport near the cathode. Aside from the benefits of the low work function of Ca for charge extraction, subsurface diffusion might allow Ca(s) dendrites to access underlying PCBM domains to form more percolation pathways for electrons to exit the active layer and generate power.

CONCLUSIONS

The interface formation of Ca onto PCBM was studied by microcalorimetry, LEIS, and XPS. Calcium gas physisorbs to the surface and either desorbs again or binds to one of two population sites: (1) subsurface methyl ester groups, releasing a heat of ~624 kJ/mol and dominating the heat of adsorption up to 0.4 ML coverage, or (2) 3D Ca(s) particles at the surface and near subsurface with a heat of adsorption equal to the bulk heat of Ca sublimation (178 kJ/mol). The proposed reaction with ester groups is the formation of the Ca carboxylate of PCBM, with two PCBM molecules reacting per Ca. At saturation of the first reaction, Ca has reacted with PCBM down to

~13 nm below the film surface, with ~80% of this occurring in the first 1 ML of Ca coverage. The heat of adsorption reaches the bulk heat of Ca sublimation by 3 ML. The surface is fully covered by Ca(s) at ~30 ML, suggesting extensive 3D particle growth after the reaction sites are exhausted. Shifts in the O 1s XPS peak toward lower BE is evidence of the reaction between Ca and O which is enough to overcome the band-bending seen in the C 1s peak shift (0.35 eV toward higher BE). At very low coverage (<0.05 ML), there is a high heat reaction (800-850 kJ/mol) attributed to Ca reacting with impurities in the PCBM.

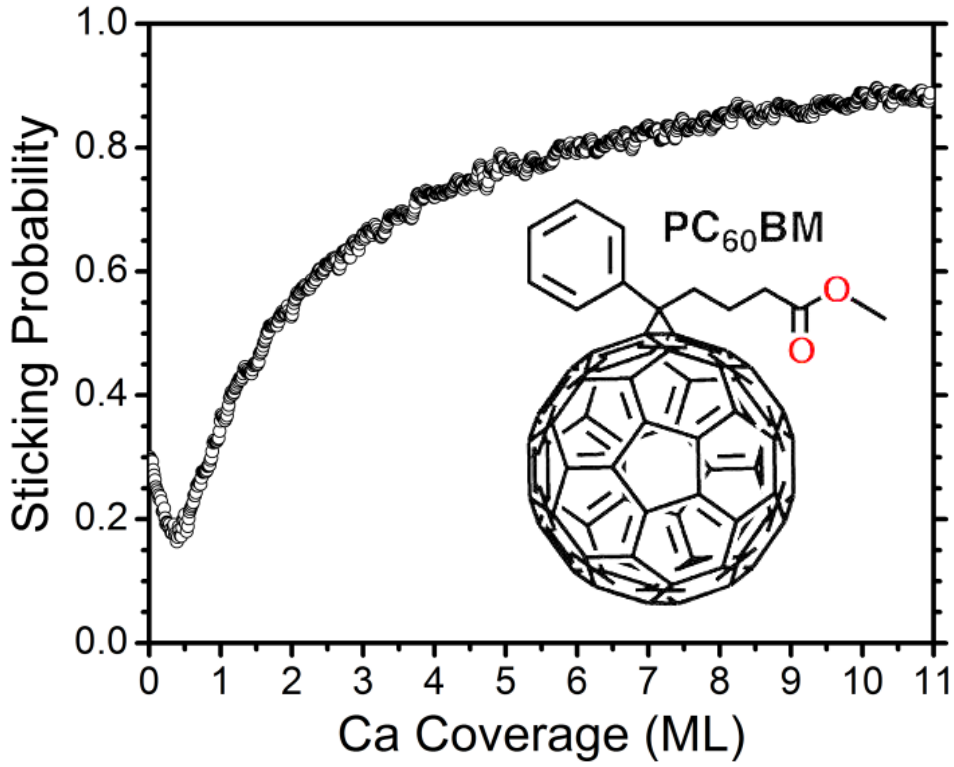

Figure 3.1. The measured sticking probability of Ca gas atoms on pristine PCBM as a function of Ca coverage at 300 K. Each data point represents a pulse of approximately 0.009 ML with a pulse frequency of 0.5 Hz. This plot is the average of three experimental runs, each of which alone showed nearly identical coverage dependences. The inset shows the PCBM molecular structure. Monolayer coverage (1 ML) is defined as the Ca(111) packing density (7.4×10^{14} Ca atoms per cm^2).

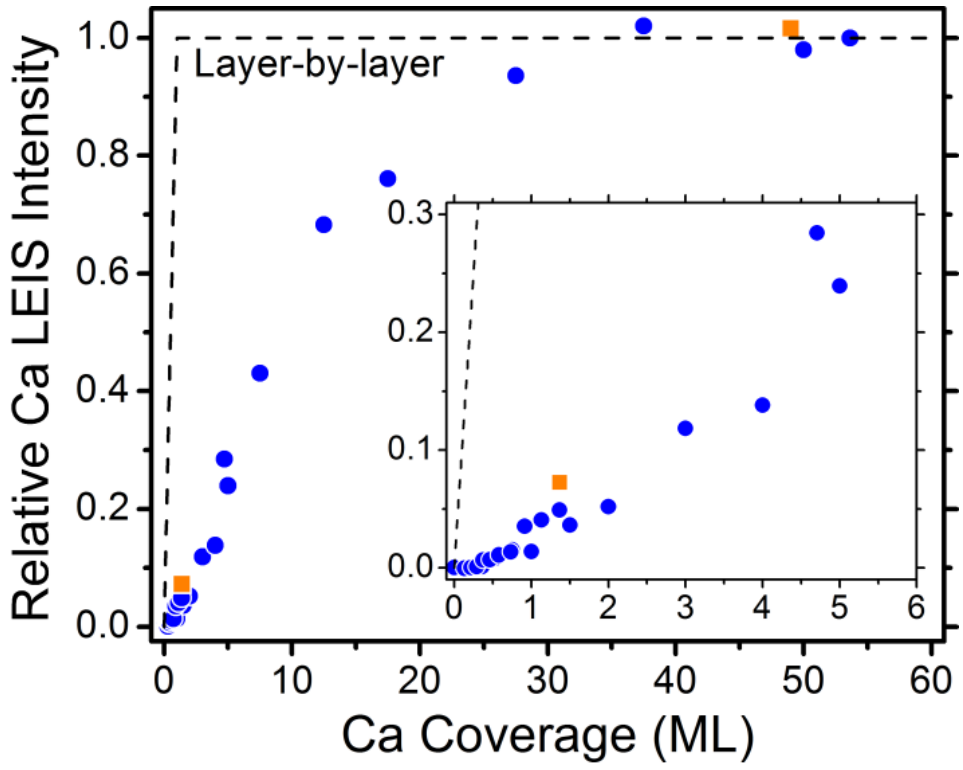

Figure 3.2. He^+ LEIS measurements of Ca on PCBM at 300 K. The relative integrated Ca LEIS peak intensity is displayed as a function of Ca coverage (round points). All intensities are normalized with respect to the saturation signal obtained for very high Ca coverages. The dashed line indicates the expected trace for the layer-by-layer growth model. The inset shows a close-up of the low-coverage region. Square points were measured using 8-fold larger Ca coverage steps than the round points, so that only 1/8 of the total He^+ ion dose was required. Their agreement shows that ion damage does not affect the data.

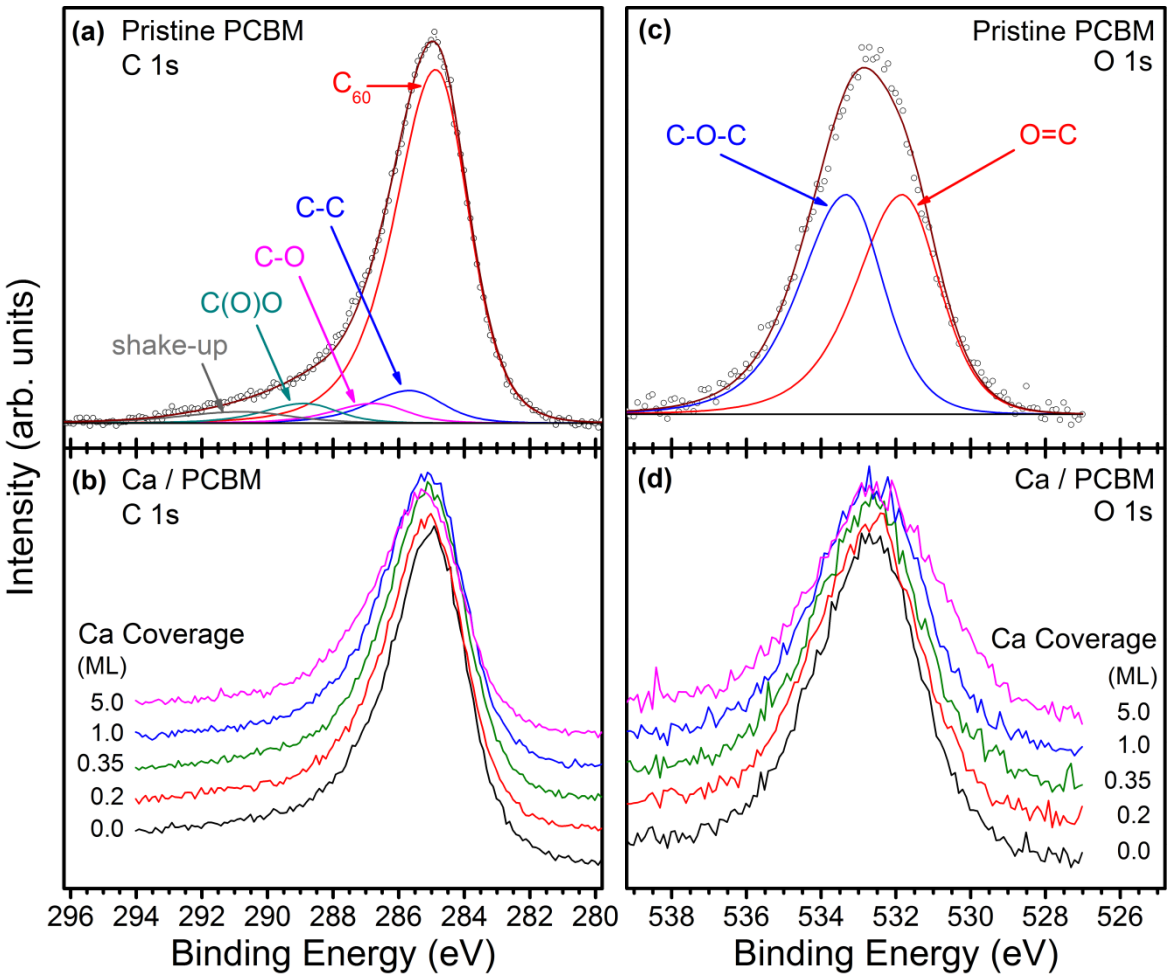

Figure 3.3. XPS spectra of the C 1s (a,b) and O 1s (c,d) regions of PCBM measured with Al Kα X-rays (1486.6 eV) at 190 eV pass energy. (a) The C 1s region decomposed into five component peaks, starting from lowest BE: conjugated C of C_{60} and the phenyl group (284.9 eV); saturated C of the butyl chain (285.7 eV); methoxy C (286.8 eV); carbonyl C in the methyl ester group (288.9 eV); and a broad peak at high binding energy attributed to shake-up satellites (290.8 eV). (b) The evolution of the C 1s region upon Ca adsorption on pristine PCBM at 300 K up to 5 ML Ca coverage. (c) The O 1s region decomposed into carbonyl O (531.8 eV) and methoxy O (533.3 eV) peaks. (d) The evolution of the O 1s region upon Ca adsorption on pristine PCBM at 300 K up to 5 ML Ca coverage.

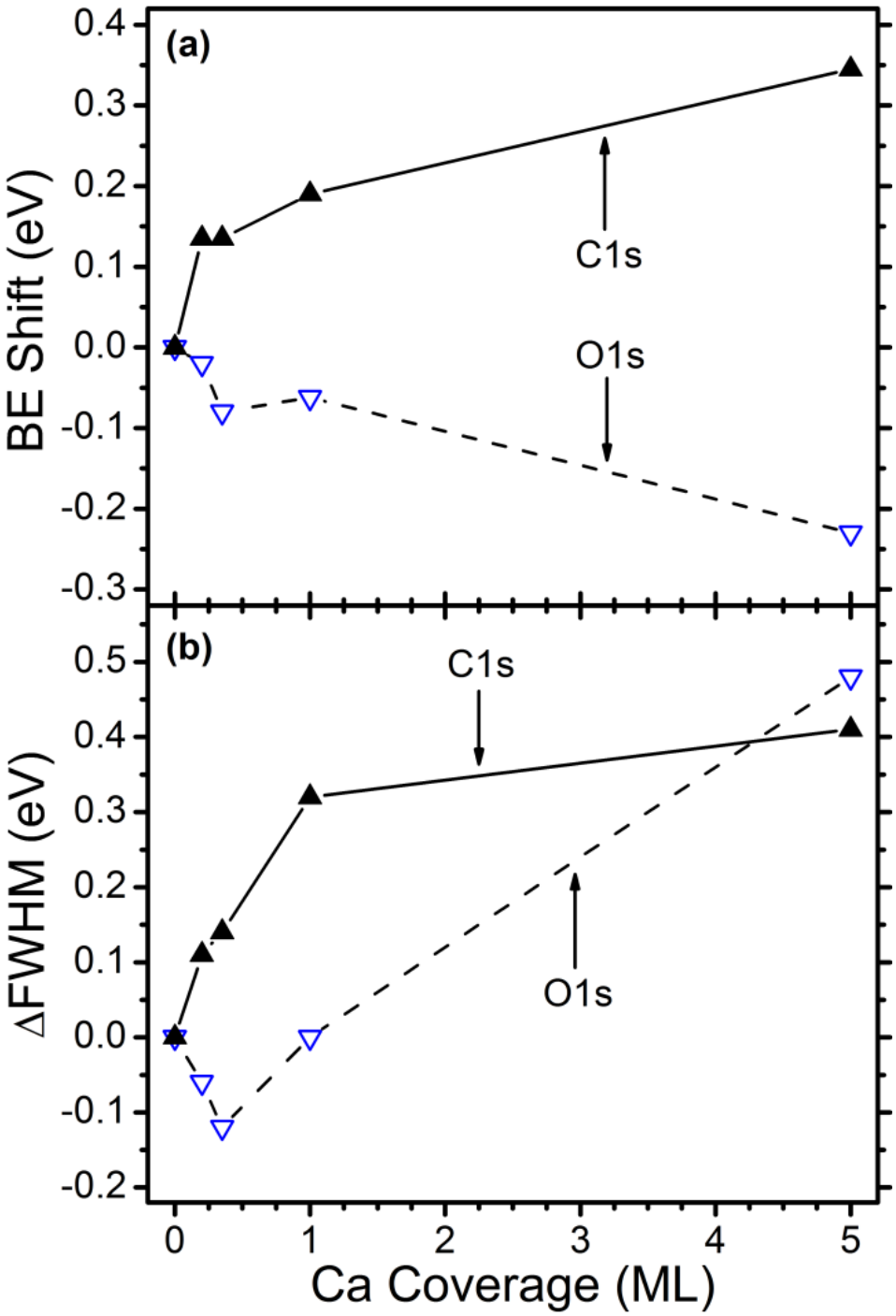

Figure 3.4. (a) Centroid XPS binding energy (BE) shifts and (b) changes in the peaks' full-width at half-maximum (ΔFWHM) for the C1s (▲, solid lines) and O1s (▽, dashed lines) XPS peaks, all plotted as a function of Ca coverage at 300 K.

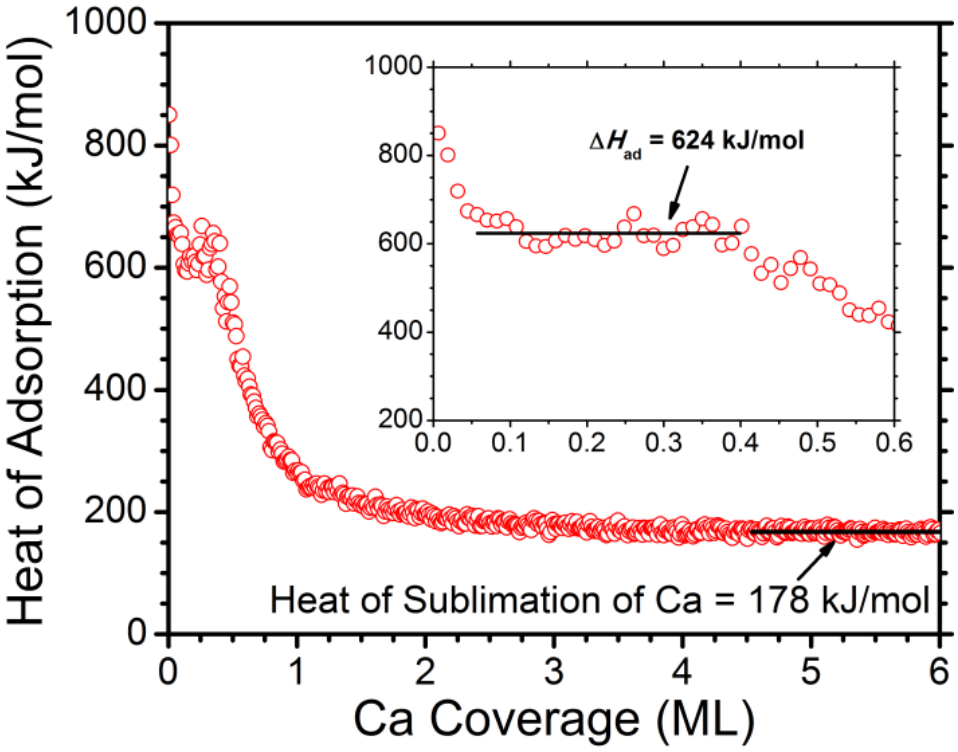

Figure 3.5. The differential heat of adsorption of Ca on PCBM as a function of Ca coverage at 300 K. The inset shows a close-up of the region up to 0.6 ML Ca coverage.

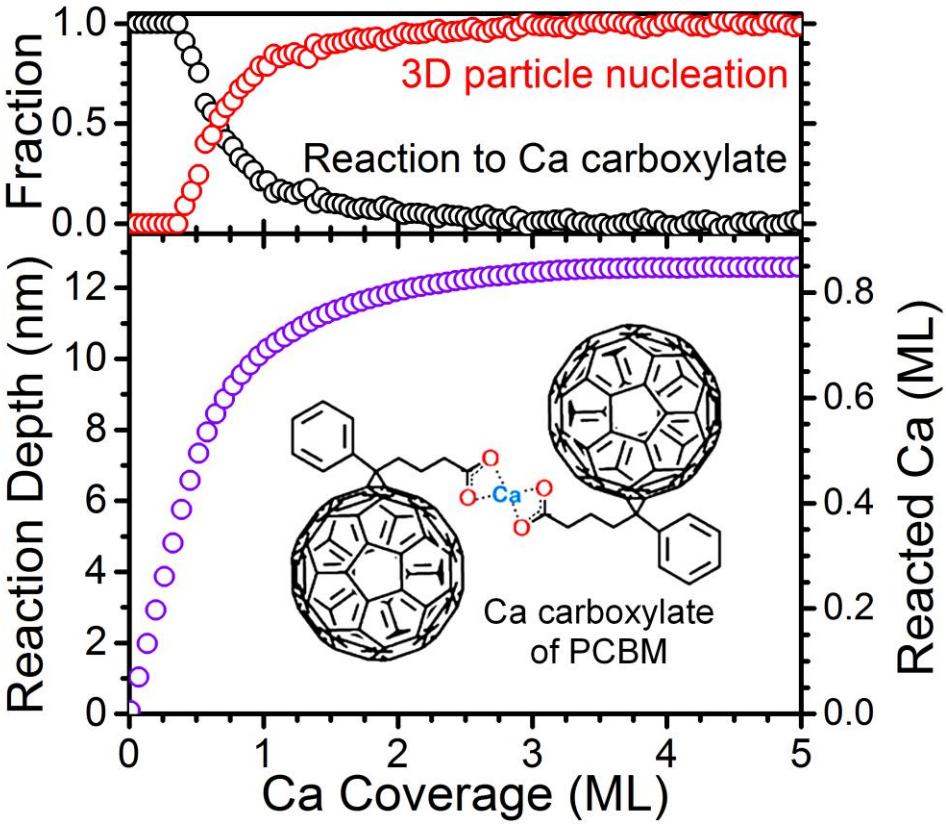

Figure 3.6. Top graph shows the fraction of Ca atoms that react with high heat with subsurface methyl ester groups of PCBM (*f*, black points) and the fraction that grow as 3D Ca(solid) particles on the surface and near subsurface (1-*f*, red points) as a function of total Ca coverage at 300 K, estimated from the heat versus coverage data as analyzed with a simple two-state model (see text). The left axis of the bottom graph shows the cumulative depth of reaction of Ca with PCBM, plotted as a function of Ca coverage at 300 K, and saturating at 12.6 nm. The right axis shows the cumulative depth of reacted Ca in ML as a function of Ca coverage. The inset shows the proposed reaction product: the Ca carboxylate of PCBM.

Chapter 4. Calcium Vapor Adsorption on the Metal-Organic Framework NU-1000: Structure and Energetics

This chapter is reprinted with permission from reference 148: J. M. Lownsbury, I. A. Santos-López, W. Zhang, C. T. Campbell, H. S. Yu, W.-G. Liu, C. J. Cramer, D. G. Truhlar, T. Wang, J. T. Hupp, O. K. Farha, Calcium Vapor Adsorption on the Metal-Organic Framework NU-1000: Structure and Energetics, *Journal of Physical Chemistry C* **2016**, DOI: 10.1021/acs.jpcc.6b05707.

CHAPTER ABSTRACT

The nature and energy of the reactions between calcium vapor and the internal surfaces of the metal−organic framework (MOF) NU-1000 have been studied by adsorption microcalorimetry, low energy He^+ ion scattering spectroscopy (LEIS), X-ray photoelectron spectroscopy (XPS), and Kohn−Sham density functional theory (DFT). NU-1000 is one of the most stable MOFs with transition-metal-oxide nodes, and thus it is of interest as a potential catalyst or catalytic support when modified with other metals. The reaction heats of Ca with NU-1000 are high below 2 monolayers (ML) Ca coverage (570−366 kJ/mol), attributed (based on DFT) to Ca reacting first with free benzoic acid functionalities or water impurities, then with H_2O and OH groups on the Zr_6 nodes to produce $Ca(OH)_2$ clusters. With higher Ca doses, the heat of Ca reaction decreases asymptotically to the sublimation enthalpy of bulk Ca (178 kJ/mol), attributed to the formation of Ca(solid) nanoparticles on the external surface, which only occurs after all of the H_2O and OH groups are titrated deeply enough (∼20 nm) such that slow Ca diffusion prevents further reaction.

INTRODUCTION

Metal−organic frameworks (MOFs) are an extensive class of nanoporous crystalline materials composed of small metal, metal oxide, or mixed-metal−oxide nodes connected by organic linker groups of a fixed length and conformation; the linkers bind to nodes via reactive binding sites such as ionized carboxylic acid groups.[51,72,73] MOFs have attracted great research interest due to a unique combination of properties, such as structural homogeneity that makes MOFs amenable to X-ray diffraction,[55,149] large surface areas[56,150] and pore sizes,[57,151] framework flexibility,[58,151] opportunities for rational design and tunability,[72,152,153] and almost limitless compositional diversity.[73] Predictive modeling has been used effectively to screen vast numbers of node/linker combinations to select high-performance MOFs for experimental study.[71,154] MOFs have numerous current and potential applications, including gas separation[65,66] and storage,[67-70] catalysis,[59-64] sensing,[155,156] and drug delivery.[157] The Zr-based NU-1000[92,158] is a particularly promising MOF for catalysis because it is water- and temperature stable,[159] has a BET surface area of >2000 m^2/g,[92,159] and has 31 Å hexagonal pores that allow large molecules to penetrate into the bulk of the MOF crystallites. See **Figure 4.1** for the structure of NU-1000.

Because MOF nodes can be oxide clusters of controllable sizes near ~1 nm in diameter, they can be thought of as very well-defined and homogeneous oxide "nano-supports" to which catalytic metals (like Pt, Ag, Pd, etc.) could be attached to achieve improvement in activity or simply to provide a more homogeneous structure to facilitate fundamental studies of supported metal clusters. The organic linker groups effectively isolate these nodes (and the supported metals) from each other, thus possibly preventing sintering of the metal centers. Additionally, due to the highly ordered nature of MOFs, their structures can be easily determined with X-ray diffraction

(XRD).[55,85,149] Thus, the binding of metal atoms and metal clusters to the oxide nodes of MOFs like NU-1000 is a subject of considerable interest.

Loading MOF nodes with metals has been demonstrated *via* chemical vapor deposition,[77] solution phase impregnation,[160,161] and even solid grinding.[78] The large pore size and water/temperature stability of NU-1000 also allows for metal loading *via* atomic layer deposition (ALD)[85-87] and metal exchange[162] that would otherwise be severely limited by framework degradation and vapor-phase mass transport. Mondloch *et al*.[85] used XRD to show that the crystallinity of NU-1000 was not significantly altered by loading the nodes with Al and Zn *via* ALD, and they used diffuse reflectance infrared Fourier transform spectroscopy to confirm that Al and Zn react with free hydroxyl groups on the Zr_6 nodes. Kim *et al.*[86] used XRD and X-ray pair distribution function analysis to show similar results for loading NU-1000 nodes with indium *via* ALD.

Here, we study the bonding energetics of calcium vapor adsorption onto clean NU-1000 at 300 K in ultrahigh vacuum using adsorption microcalorimetry, surface spectroscopies, atomic beam/surface scattering, and Kohn−Sham density functional theory (DFT). As shown below, the Ca atoms are transiently adsorbed in a weakly held precursor state that allows them to diffuse deeply (∼10−20 nm) into the NU-1000. Thus, we probe here mainly the internal surfaces of the NU-1000. These have a BET surface area of 2040−2320 m^2/g.[92,159] Calcium is chosen as the probe metal here to study the metal-binding properties of NU-1000 since we already know a lot about how Ca binds to the surfaces of bulk metal oxides,[102,163] pure hydrocarbon surface functionalities,[26] and organic carboxylate and ester groups in the surfaces of polymers.[28-30,95] Specifically, Ca has a very weak interaction with pure hydrocarbon groups,[26] so it is not expected to interact strongly with the fused benzene rings of the linkers. Thus, it is expected to react only at the zirconium oxide

nodes or at the carboxylate groups that bind the linkers to these nodes. We elucidate the film-growth mechanism and surface morphology of the evolving Ca film using low-energy He^+ ion scattering spectroscopy (LEIS) and X-ray photoelectron spectroscopy (XPS). Simultaneous measurement of the heat of adsorption and sticking probability of the metal atoms as a function of coverage provides the interfacial bonding energies for Ca on NU-1000 as a function of Ca coverage. The reactions are modeled with DFT and interpreted in that light. These results show a strong tendency for Ca metal to diffuse into the pores of NU-1000 and react either with –OH and $–OH_2$ groups on the Zr_6 node, free carboxylic acid on the external surface, or residual weakly-bonded water in kinetic competition with Ca(solid) particle nucleation and growth on the surface and in the pores, and eventually Ca(s) film growth across the MOF surface. These reactions occur extensively to a depth of ~20 nm beneath the NU-1000 surface.

EXPERIMENTAL METHODS

NU-1000 was prepared solvothermally and then activated, as described previously.[85] Activation removes synthesis solvent and replaces benzoate ligands (nonstructural ligands) on the nodes with aqua and hydroxo ligands. ^{1}H NMR of the digested material confirmed that activation was complete, with the only carbon-containing component being the tetra-acid of the MOF organic linker, pyrene-tetraphenylcarboxylate. Nitrogen adsorption measurements of the activated MOF yielded the BET surface area, the pore volume, and the isotherm shape expected for a clean and undamaged sample. Powder X-ray diffraction measurements yielded the pattern expected for NU-1000, with no evidence of the formation of polymorphs such as NU-901.[164] The MOF crystallites are necessarily terminated with linkers, nodes, or both, with the identity of the terminating units possibly being crystal-face dependent. A linker-terminated face will present unreacted carboxylic

acid groups. We have been unable to observe these by diffuse reflectance infrared Fourier transform spectroscopy (DRIFTS), which is not unexpected even if they are present, as the detection limit is about 1%. A node-terminated face will present excess aqua and hydroxo ligands. These additional ligands, if present, are likely to be indistinguishable by DRIFTS from aqua and hydroxo ligands present within the crystallites.

Thin NU-1000 films were prepared by drop-casting from an agitated NU-1000 solution (0.5 wt% in acetone) directly onto the heat detector, a metal-coated foil of the pyroelectric polymer β-polyvinylidene fluoride (PVDF, see below). Three ~6 μL aliquots were drop-cast onto the substrates which were covered by a small upturned cup with a hole in the center to slow the evaporation rate of acetone. This yielded NU-1000 films ~1.5 μm thick that uniformly coat the PVDF with low surface roughness confirmed using a microscope. We typically prepared ten NU-1000-coated heat detectors at a time, and transferred them to the sample preparation chamber *via* a stainless steel "suitcase" equipped with a gate valve. With the suitcase attached, the preparation chamber was evacuated to its base pressure of 2×10^{-9} mbar and heated at 348 K for ~10 h to outgas the samples and remove trace solvent and physisorbed water. The samples were then transferred into the ultrahigh vacuum (UHV) analysis chamber for surface characterization and calorimetry as needed.

The heat detectors were ~1.3 cm diameter disks cut from 28 μm thick sheets of PVDF, pre-coated on each side with 70 nm Cu and topped with 10 nm Ni for electrical contacts (purchased from Measurement Specialties). These heat detector disks were coated with NU-1000 as described above. After coating with NU-1000, these "samples" were mounted onto sample platens specially designed such that the sample disks are fixed in place by a thin copper washer and the front and back contacts are electrically isolated from each other by a ceramic bushing, as described

elsewhere.[27,95] The reflectivity of these NU-1000 films at the He-Ne laser wavelength (632.8 nm) was measured *ex situ* using an integrating sphere and was found to be 0.737 ± 0.018. The standard deviation of the reflectivity measurement for an individual sample was less than 3%.

The surface analysis chamber, its adsorption calorimeter, and its pulsed metal atom beam have been described previously.[94] Briefly, the UHV chamber used for these experiments had a base pressure of 3×10^{-10} mbar and was equipped with a hemispherical energy analyzer (Leybold-Heraeus EA 11/100) for LEIS and XPS, ion gun (Leybold-Heraeus IQE 12/38), Mg/Al Kα dual anode X-ray source (VG Scienta XR3E2), quartz crystal microbalance (QCM, Inficon), quadrupole mass spectrometer (QMS, UTI 100C), and adsorption microcalorimeter.

The calorimetric method used here has been described previously.[27,94] Briefly, the NU-1000-coated sample platens were heated in the preparation chamber vacuum at 348 K for at least 1 hour prior to each experiment, then transferred to the analysis chamber. The sample platen was then mounted on a large Cu thermal reservoir where electrical connections were made to its heat-detector electrodes. A collimated 4 mm diameter beam of Ca gas atoms was chopped into 100 ms long pulses containing 0.009 monolayers (ML) of Ca at a rate of 0.5 Hz. One ML of Ca is defined here as 7.4×10^{14} atoms per cm^2 of geometric (projected flat) area, which is the packing density of the Ca(111) crystal face. The energy from gas adsorption generates a transient temperature rise in the NU-1000 sample, which is transferred by thermal diffusion to the pyroelectric PVDF detector it coats. The resulting peak-to-peak voltage response was calibrated using the voltage response to pulses of known energy from a stabilized He-Ne laser with 632.8 nm wavelength. A sensitivity of ~350 volts per joule of heat absorbed by NU-1000 was commonly found. Since the calorimeter sensitivity and laser power at the sample are constant throughout the experiment, we can determine the change in optical reflectivity of the samples at the He-Ne wavelength due to addition of Ca by

measuring the heat signal of the laser before and after dosing Ca. The heat signal for the laser increased by an average of 29% to ~450 V/J. That is, more light was absorbed by the sample after Ca was adsorbed on the NU-1000 surface. The average calculated reflectivity after experiments was 0.663 ± 0.020. This is approximately the reflectivity of 632.8 nm light reported for thick Ca films.[165] The operating temperature of the Ca beam source was ~923 K, which generates thermal optical radiation that impinges on the sample along with the Ca metal atoms. This thermal radiation was measured by translating a BaF_2 window into the path of the beam, allowing ~95% of the optical radiation to pass through to the sample, while blocking the metal atoms. This radiation contribution was subtracted from the total measured signal. To convert the measured internal energy changes into the standard heat change at the surface temperature (300 K), the excess translational energy of the metal gas atoms at the oven temperature above that for a 300 K Maxwell-Boltzmann distribution was subtracted, and a small pressure-volume work term (RT) was added, as described elsewhere.[94]

The sticking probability for Ca on NU-1000 was determined using the QMS with the modified King-Wells method described previously.[94,96] A metal grid positioned between the QMS and the sample was biased at -500 V to prevent damage to the samples from electrons emitted by the QMS filaments. The growth of Ca on NU-1000 was studied by LEIS using He^+ ions with a primary energy of 1 keV and an angle of 45° between the ion gun and analyzer axes (i.e. 135° scattering angle). Ion fluxes were typically 15 nA/cm^2 and the sample was exposed to the He^+ beam for 2 min to measure the C and Ca signal at each coverage. A two-point experiment also confirmed that beam damage is not a significant factor during LEIS. For XPS experiments, 260 W Mg Kα X-rays (hν = 1253.6 eV) were used and the spectra were referenced to the C 1s peak of NU-1000. The samples used in LEIS, XPS, and calorimetry experiments were baked at 348 K in

the preparation chamber vacuum for at least 1 hour prior to experiments to ensure the samples were free of water. Calorimetry was also performed on samples baked for 10 minutes at 378 K in the preparation chamber vacuum, then cooled to 348 K prior to experiments. Baking to higher temperatures removes any remaining physisorbed water in the MOF channels, as well as structural $–OH_2$ groups from the Zr_6 node.[86] All experiments were performed at 300 K.

COMPUTATIONAL METHODS

The experimental crystal structure of NU-1000[85] was used as the initial structure in our study. We also built a cluster model ($Zr_6C_{56}O_{32}H_{56}$, see below) that has one Zr_6 core and eight benzoates attached to it; the geometry of the cluster was optimized with all carbons fixed to their positions that were optimized in a periodic calculation from previous work.[158] The *Gaussian 09*[166] and *CRYSTAL14*[167] software suites were used for the cluster and periodic calculations, respectively. All theoretical calculations, both cluster and periodic, were performed with Kohn-Sham density functional theory (DFT) with atom-centered Gaussian basis functions. We used the M06-L[168] exchange-correlation functional for geometry optimization (and Hessian calculation in the case of clusters), followed by a single-point energy with the M06-2X[169] functional, which has been previously validated as giving an accurate energy for the formation of a Ca-O bond.[170] We used the 6-31G(d,p)[171-175] basis set for H, C, and O. The SDD effective core potential and corresponding basis set were used for Zr[176,177] and Ca.[178]

An ultrafine integration grid was used for all cluster calculations. Enthalpies were calculated at 300 K. The vibrational contributions were calculated by the quasiharmonic approximation, which means using the harmonic oscillator formulas but with scaled frequencies that account for anharmonicity and systematic errors in the density functional calculations, as

explained elsewhere.[179] The scale factor used was 0.978 for M06-L, as calculated by the *Freqscale* program.[180]

In periodic calculations, the lattice constants and atomic positions were both optimized except in the slab calculations, in which the lattice constants were fixed to values optimized in the bulk calculations. For geometry optimization in the periodic model, the Gaussian basis functions with exponents smaller than 0.06 and the polarization p function of H were removed. In the following single-point calculation, the basis functions of Ca with exponent smaller than 0.06 but greater than 0.03 and the polarization p functions of H were added back to better describe the reactions involving H and Ca. Default settings were used in *CRYSTAL14* except that ITol5 was increased to 35 to facilitate convergence of the M06-2X calculations. All enthalpies from periodic calculations are approximated by adding the reaction energy at 0 K (neglecting zero-point energies) from the periodic calculation to the difference from the cluster calculations between the enthalpy of reaction at 300 K and the energy of reaction at 0 K (neglecting zero-point energies).

RESULTS

Sticking Probability

The amount of Ca vapor that actually adsorbs on the NU-1000 surface must be known to determine the true Ca coverage from the Ca flux and to convert enthalpies of adsorption/reaction measured by calorimetry into units of kJ per mole adsorbed. **Figure 4.1** shows the sticking probability of Ca atoms on NU-1000 (outgassed at 348 K) as a function of Ca coverage at 300 K. In the limit of zero coverage, the sticking probability of Ca on NU-1000 was 0.91 and increased steadily to within 1% of unit sticking by 3 ML coverage. Multilayer Ca films are known to have near unit sticking probability for Ca at 300 K.[102] The flux of the Ca atom beam was measured with the calibrated

QCM at 300 K, pre-coated with a multilayer of vapor-deposited Ca to ensure unit sticking probability. Coverage was determined by time-integrating the product of the Ca flux and the sticking probability.

Low-Energy Ion Scattering Spectroscopy

LEIS with He^+ ions is useful for determining the location of the adsorbed Ca because it provides element-specific information while probing only the topmost atomic layer of the solid.[97,98] **Figure 4.2** shows the evolution of the Ca and C LEIS signals, both normalized to their maximum values, as a function of Ca coverage on NU-1000 at 300 K, with the inset depicting the low coverage region in more detail. Effects of beam damage by He^+ ions were determined to be negligible by comparing the signal intensity versus coverage to a control experiment which exposed the surface to ~5 times fewer ions but yielded identical results within the data scatter. The Ca signal grows much more slowly with Ca coverage than predicted by a layer-by-layer growth model on a flat substrate, and even more slowly than on flat films of several polymers and organic semiconductors we investigated previously,[22-26,28-30,95] where the Ca was shown to diffuse deeply below the external surface at 300 K (down to at least 3 nm and up to 12 nm, depending on the material) before reacting with internal surface functional groups that contain heteroatoms. However, the curve is similar in shape to the Ca growth curves on phenyl-C_{61}-butyric acid methyl ester (PCBM)[95] and the polyfluorenes poly(9,9-di-*n*-hexyl-2,7-fluorene) (PDHF) and poly(9,9-di-*n*-hexyl-2,7-fluorene vinylene) (PDHFV),[26] which contain very few heteroatoms (none in the case of the polyfluorenes). In general, the very slow growth of Ca LEIS signal in those cases was due to a combination of (1) Ca diffusing below the surface and reacting with internal surface groups, followed by (2) Ca atoms nucleating clusters of Ca(solid) on the surface, which grow into thick

3D Ca particles that cover only a small fraction of the surface initially (but eventually make a continuous over-coating). This second step has a heat of adsorption very similar to the heat of sublimation of bulk Ca(s), 178 kJ/mol.[134] It appears in **Figure 4.2** that a similar behavior occurs here, so that Ca initially (up to >5 ML here) is reacting with sites below the external surface and thus is binding to the internal surfaces of the NU-1000, where it is invisible to LEIS.

The C LEIS signal increased in intensity and shifted to lower kinetic energy over the course of the first 2 ML, where the Ca signal was still negligible. As the Ca signal appears and begins to rise, the C signal starts to drop, finally approaching zero as the Ca signal approaches its high-coverage limit.

X-Ray Photoelectron Spectroscopy

Due to the insulating nature of NU-1000, sample charging made analysis of the chemical state of NU-1000 with XPS peak energies and their changes with increasing Ca coverage impossible. The ratio of the integrated areas of the Ca 2p XPS peak at increasing Ca coverage to the initial C 1s peak at 300 K is shown in **Figure 4.3**. This Ca/C^0 ratio increases very slowly below 1 ML Ca coverage, consistent with the diffusion of Ca below the XPS probe depth. The growth of the Ca/C^0 ratio is much slower than is predicted by the layer-by-layer growth model on a flat surface, also shown in **Figure 4.3**. The tabulated inelastic mean free path of C 1s electrons (λ_C) is 26.2 Å when excited with Mg Kα X-rays ($h\nu$ = 1253.6 eV).[139] For the layer-by-layer model calculations, following Ertl and Küppers,[181] we increased λ_C by a factor of 1.8 to account for the large void density in NU-1000. The density of NU-1000 was estimated to be 0.85 g/cm^3 (i.e., 1.8-fold smaller than 1.5 g/cm^3, a typical density for materials of similar composition used to determine λ_C). The sensitivities for C and Ca were taken from Wagner *et al.*[182] The experimental peak area ratio also

grows more slowly than was found previously for Ca deposition on PCBM (a functionalized C_{60} buckyball), where Ca was shown to diffuse and react at depths greater than 10 nm below the PCBM surface.[95]

Calorimetric Enthalpies of Adsorption

Figure 4.4 shows the differential enthalpy of adsorption of Ca on NU-1000 samples that had been outgassed in vacuum at 348 K and 378 K as a function of total Ca coverage at 300 K. For pulses containing ~0.009 ML of Ca, the pulse-to-pulse standard deviation of the enthalpies of adsorption at high coverages, where the enthalpy is independent of coverage, is approximately 10 and 32 kJ/mol for samples baked at 348 K and 378 K, respectively. The increase in noise may be due to the fact that the pyroelectric response of PVDF begins to degrade at temperatures above ~333 K, and this degradation increases with temperature.[183] Additionally, three experiments were averaged on samples baked at 348 K, compared to only two experiments on samples baked at 378 K. For samples baked at 348 K, the enthalpy of adsorption in the limit of zero coverage is ~-513 kJ/mol. Outgassing the NU-1000 to 378 K for 10 minutes increased the initial enthalpy of adsorption to ~-570 kJ/mol. Note that the sticking probability (S) versus coverage was not measured for the samples outgassed at 378 K. Since S was so close to unity at all coverages for NU-1000 samples outgassed at 348 K (**Figure 4.1**), and the enthalpy versus coverage was so similar for both outgassing temperatures, we assumed it was the same for 378 K as at 348 K.

Figure 4.4 shows that the very negative reaction enthalpies (<-250 kJ/mol) extend to Ca coverages of >2 ML, or 1.48×10^{15} Ca atoms per cm^2. The DFT calculations below, and the general trend from our earlier measurements that Ca does not react strongly with pure hydrocarbon moieties,[26,95] show that the high-enthalpy-release reactions are due to reactions with nodes and

reactive, dangling carboxylic acid groups. Given the low density of these node sites, this 2 ML Ca coverage corresponds to a reacted depth of >10 nm (see below). This means that, just as with Ca adsorption on polymer films,[22,23,25,26,28,95] Ca is initially bound in a weakly held state that diffuses rapidly into the NU-1000 and thus can react quite deeply within the internal surface area.

Computational Results

In this section we discuss the results from periodic and cluster calculations and compare them to experiment. To make the presentation unambiguous and easier to follow, we adopt the convention of following each numerical value for energies or enthalpies by "[C]" if it is an enthalpy from a cluster calculation, by "[P]" if it is an approximated enthalpy from a periodic calculation, and by "[T]" if it is an enthalpy from tabulated experimental numbers in references.

As shown in **Figure 4.5**, the cluster model of the nodes studied here ($Zr_6C_{56}O_{32}H_{56}$) has one Zr_6 core and eight benzoates attached to it, in the geometry optimized from previous periodic calculations.[158] As a strong reducing agent, Ca reacts with acidic hydrogens to produce H_2. In the absence of protons, Ca can also react with H_2 to give calcium hydride.[184] In NU-1000, the possible sources of protons are uncoordinated benzoic acid moieties on the external surface, $–OH_2$ or –OH groups of the Zr_6 nodes, and residual water that is solvating nodes otherwise fully saturated with aquo and hydroxo ligands. We show below that the dominant reactions are with $–OH_2$ and –OH groups of the Zr_6 nodes (i.e., on the internal surfaces of the MOF), as shown for the cluster model in **Figure 4.5**. We calculated the energies and enthalpies of Ca reacting with these and the other types of functional groups on the internal and external surfaces of NU-1000 by both cluster and periodic DFT, as listed in **Table 4.1**.

There are terminal uncoordinated carboxylic acid sites at the external surface of the NU-1000. Thus, the following reaction between Ca and unreacted carboxylic acid groups of the linkers may occur:

$$Ca(g) + 2\ RCOOH \rightarrow (RCOO)_2Ca + H_2(g) \qquad (4.1)$$

Since the external surface has ~3.5 x 10^{13} nodes per cm^2 of area (see below) and each such surface node may contribute two such benzoic acid groups, this reaction could occur for a maximum of 3.5 x 10^{13} Ca atoms per cm^2, or less than 0.05 ML of Ca. The calculated enthalpy of reaction in the gas phase for R = Ph (benzoic acid) is -531 kJ/mol [C]. (For comparison, the experimental reaction enthalpy for R = methyl is -695 kJ/mol, from thermodynamic tables of heats of formation [T].[134,143]) To calculate the reaction between Ca and uncoordinated benzoic acid moieties on the surface, we built a periodic slab model of the [001] surface of NU-1000 containing a single layer of three Zr_6 nodes (1 unit cell), terminating with 12 pyrene linkers in total, each of which has two benzoic acids on either the top or bottom surface, as shown in **Figure 4.6a**. We considered Ca reacting with different percentages of surface benzoic acid to form H_2: 50% (one benzoic acid reacted per pyrene) and 100% (two benzoic acids reacted per pyrene). For the 50% case, we found two benzoate and one unreacted benzoic acid groups to coordinate Ca^{2+}, as shown in **Figure 4.6b**, with the net reaction energy per Ca being -538 kJ/mol [P]. The extra coordination from the C=O bond of an unreacted benzoic acid to Ca^{2+} may account for the slightly more exothermic reaction compared to the gas-phase reaction 4.1. The large exothermicity also agrees with the high initial enthalpy release measured experimentally, because the external surface of NU-1000 is the first to make contact with deposited Ca. For the 100% case, we found that each Ca^{2+} is chelated by two

benzoates, as shown in **Figure 4.6c**. The enthalpy of reaction (-500 kJ/mol [P]) is not only lower than the 50% case, but also lower than the enthalpy of Ca reacting with two free benzoic acids, i.e. benzoic acids in the gas phase (-531 kJ/mol [C]); this may be attributed to the more constrained geometry for two benzoates binding to Ca at the surface.

There is one unsatisfactory feature of a model where the initial reaction of Ca is with dangling benzoic acid-type groups on the external surface of the MOF, as discussed above. The Ca LEIS signal is undetectable in the first 1 ML of coverage (see **Figure 4.2**), and certainly far below that expected for 10% of a ML of Ca bound on the external surface to benzoic acids. If this reaction does occur to the extent of 10% of a ML of Ca (twice the maximum estimated above), the reacted Ca must somehow get below the benzene rings so they are hidden from the He^+ ions.

The Zr_6 node in NU-1000 has 16 protons distributed on four faces: three each on two faces in the large pore (diameter d = 31 Å), three each on two faces in the small pore (d = 10 Å), and four present as -OH groups of the node itself.[63] Each face has the most stable proton topology[158] as shown in **Figure 4.7**. To model Ca reacting with an OH_x groups on a Zr_6 node, we replaced different numbers of H atoms for OH_x functionality on the Zr_6 node by Ca in the unit cell. We surveyed the reactions shown in **Figure 4.7** to assess the following cases in **Figure 4.8**: (**a** and **b**) one Ca in the large or small pore, (**c**, **d**, **e**, and **f**) two Ca in the large or small pore, (**g**, **h**, **i**, **j**, **k**, and **l**) four Ca, one Ca per face or two Ca per face in the large or small pore, and (**m**) eight Ca replacing all H atoms on the node. To reduce the computational cost, C_2 or C_i node symmetry is imposed on these geometries where possible; further differentiation of the cases is provided in the caption of **Figure 4.8**, which shows the optimized structures.

The calculated enthalpies of reaction per Ca for the reactions leading to the products in **Figure 4.8** are given in **Table 4.1**. The first Ca has similar exothermicity to react with the OH_x

groups in the large pore or small pore (-421 kJ/mol [P]), and this value is greater than found for the cluster calculation (-395 kJ/mol [C]), indicating the effect of relaxation of linkers that are fixed in the cluster calculation. A higher enthalpy of reaction per Ca atom (-436 kJ/mol [P]) is found for placing two Ca atoms in the large pore with C_i symmetry. In this optimized structure, two benzoates dissociate one O atom from a Zr ion and coordinate the two Ca ions with the PhC(O)O–Ca distance being 2.23 Å. The dissociation and re-coordination of benzoate are more prominent for cases with C_i symmetry, such as two Ca in the large or small pore, as shown in **Figure 4.8c** and **e**, and for cases with high Ca loading (equal to or greater than 4 Ca per node). The most exothermic case (per Ca) is when four Ca react with the most acidic protons ($-OH_2$) and μ^3-OH on each face (-459 kJ/mol [P]); Ca reacting with the remaining protons releases less enthalpy, as reflected by the smaller enthalpy of reaction per Ca in the case of 8 Ca per node (-393 kJ/mol[P]). This type of reaction should account for the middle range of the experimentally measured enthalpies of reaction as Ca diffuses into the pores of NU-1000.

Another proton source is from the residual weakly bonded water that may remain within the NU-1000 samples after outgassing. We estimated the reaction enthalpy between Ca and residual water by checking tabulated heats of formation for the following reaction at 298 K:[134]

$$Ca(g) + 2\ H_2O(g) \rightarrow Ca(OH)_2(s) + H_2(g) \qquad (4.2)$$

which has an enthalpy of reaction of -679 kJ/mol [T]. To estimate the amount of physisorbed water remaining in the MOF under UHV, we calculated the bonding strength between the water and the node. Two different conformations were examined, as shown in **Figure 4.9**.

Let us estimate the coverage of surface sites by weakly-held residual water by assuming that every water molecule that strikes the surface sticks and equate that adsorption rate at 300 K and 2×10^{-9} mbar water with a desorption rate given by the product of a typical desorption prefactor for water (10^{13} s^{-1}), the saturation number of water sites per unit area (~10^{15} cm^{-2}), the fractional coverage of water sites (θ) and $\exp(-E_{des}/RT)$, where E_{des} is the activation energy for desorption. We estimate E_{des} from the binding enthalpy for conformation **a** in **Figure 4.9** to be -66.7 kJ/mol. These values give a steady-state population of $\theta = 3 \times 10^{-5}$. If such residual water molecules and the Ca itself were so rapidly diffusing that incoming Ca atoms could be found by water molecules that diffused from ~60 nm below the surface, this could explain 0.1 ML of reacting Ca with the very high initial heat observed. We show evidence below that diffusing Ca atoms probe down to >20 nm below the surface in their reaction with immobile water and –OH groups that are intrinsic to the nodes.

In the absence of other protons, Ca might react with a Zr–OH group in a single step to form a hydride (in the form of Zr–O–Ca–H). This hydride can exist as a reaction intermediate for Ca reacting with an –OH group or as a stable product when protons are almost depleted. We calculated the enthalpy of reaction for one representative case to form a Ca–H bond, as shown in **Figure 4.8n**; this reaction has an enthalpy of reaction of -311 kJ/mol [P], which is less than the one to produce H_2 but still comparable.

Calcium gas can also react with the gaseous H_2 product of the above reactions to produce calcium hydride (presumably as solid clusters within the NU-1000 pores) with an enthalpy of -359 kJ/mol [T] based on standard enthalpies of formation.[134] This would need to occur before the H_2 escapes the NU-1000 (as it would otherwise be pumped away), and may even occur with the H atoms they release before any H-H bond is formed. If some of the Ca reacts with H_2, the heat

released per mole of Ca would be some average of this 359 kJ/mol with the calculated heat from one or more of the above reactions that produce H_2.

Once all protons are consumed, the incoming Ca nucleates and grows nanoparticles of solid Ca in a pore of NU-1000 at or near its external surface; therefore the reaction enthalpy approaches the negative of the enthalpy of sublimation of bulk Ca(solid). To study the nucleation step, we first placed two Ca on 1,3,6,8-tetrakis(phenyl)pyrene in the cluster model. After optimization, the flat pyrene becomes slightly bent toward two Ca, and the enthalpy of reaction per Ca is -62 kJ/mol [C]. The CM5 partial atomic charge[185] on each Ca in this case is 0.37 and the Mulliken partial atomic charge[186] is 0.39; these values indicate that Ca dimer donates electrons to pyrene to form a charge-transfer complex [$Ca_2^+\cdots pyrene^-$]. To study how the geometry constraint on pyrene in NU-1000 affects the enthalpy of reaction, we also placed two Ca on pyrene in a periodic calculation (inside or outside the triangular channel, as shown in **Figure 4.10a** and **b**, respectively). For the in-channel and out-of-channel configurations, the Ca–Ca distance is 3.81 and 3.87 Å, respectively, with Mulliken charges on each Ca of 0.52 and 0.46, respectively, indicating more charge transfer in the condensed phase. The enthalpies of reaction for both conformations are slightly lower (-49 and -45 kJ/mol [P]) than the ones in the gas-phase calculations (see **Table 4.1**), reflecting the condition that both linker conformations in the periodic calculation are constrained. When protons are depleted, this reaction can make the first Ca–Ca bond for the nucleation step in forming Ca(solid) clusters.

DISCUSSION

The experimental results can be summarized as follows: (a) the exothermicity of Ca adsorption on NU-1000 is initially very high (~513 and ~570 kJ/mol in the limit of zero coverage for samples

baked at 348 K and 378 K, respectively) and much greater than the bulk enthalpy of Ca sublimation (ΔH_{sub} = 178 kJ/mol); (b) the exothermicity of Ca adsorption approaches ΔH_{sub} by ~5 ML coverage; (c) the Ca LEIS intensity increases much more slowly with Ca coverage than is predicted by a layer-by-layer growth model, only reaching complete layer coverage by ~40 ML; (d) the Ca/C^0 XPS peak area ratio increases much more slowly on NU-1000 than is predicted for a layer-by-layer growth model.

In the following, we will describe a model for the progress of the reaction of Ca with the NU-1000 interface/film that is consistent with these results.

As shown in **Figure 4.2**, the Ca LEIS signal intensities remain near zero for the first ~2 ML of Ca coverage, where the exothermicity of Ca adsorption drops slowly from its initial value (above 500 kJ/mol) to ~280 kJ/mol, still ~100 kJ/mol larger than ΔH_{sub}. This, together with the very weak Ca XPS signal, is consistent with nearly all of the adsorbing Ca atoms diffusing below the external surface at coverages below 2 ML, where they undergo much more exothermic reaction(s) than depositing pure Ca(solid). Above 5 ML, however, the Ca LEIS signal starts to grow rapidly, and the exothermicity has dropped to within 20 kJ/mol of that for formation of Ca(s) and continues to asymptotically approach that value. In this regime, Ca must be mainly forming Ca(s) nanoparticles on or near the topmost atomic layers of the NU-1000. Between these low- and high-coverage regimes, the exothermicity and Ca LEIS signals make a transition wherein there is kinetic competition for incoming Ca atoms. They can either diffuse below the external surface to undergo a highly exothermic reaction on internal surfaces, or they can nucleate and grow 3D Ca(s) nanoparticles on or near the external surface with a much lower heat. If growth were limited only to the formation of 3D Ca(s) particles from the beginning, the measured exothermicity of adsorption should be approximately equal to the bulk enthalpy of Ca sublimation of 178 kJ/mol

(or less in the case of small clusters, due to the Kelvin effect[187]). The high exothermicity below 1 ML (570 to 350 kJ/mol) indicates a much more aggressive reaction initially at internal surface sites within the MOF. Since Ca has only very weak interactions with pure hydrocarbon polymers and hydrocarbon functional groups in polymers,[26] but reacts highly exothermically with oxygen-containing functional groups,[25,28,95] we attribute this high exothermicity to Ca reacting in some way with oxygen atoms associated with the Zr_6 nodes, either at their terminal –OH or H_2O groups, at the impurity of unreacted benzoic acid groups on linkers, or with non-crystalline residual water.

The DFT calculations above show that these large enthalpies below 1 ML (-570 to -350 kJ/mol) could include any combination of Ca reactions with RCOOH groups on the external surface or with -OH_x on the nodes. **Figure 4.4** can be explained by a kinetic competition between three reactions. (1) Initially (up to 0.05 ML of Ca), Ca reacts with RCOOH on the external surface to account for the high initial heat release (520-570 kJ/mol). (2) Next, Ca reacting with -OH_x on the nodes becomes most important, which accounts for the intermediate amount of heat released (~420-500 kJ/mol). (3) Finally, the nucleation and formation of Ca(s) dominates, with heats approaching the final exothermicity of ~178 kJ/mol.

It is not obvious why the exothermicity of reaction(s) with the initially deposited Ca atoms is slightly greater for those samples outgassed at higher temperature compared to lower temperature. However, it has recently been shown that local node structural changes, that do not affect overall crystal order, can occur in bulk NU-1000 as temperatures are elevated above roughly 400 K.[188] It may be that in the thin films, such changes can also occur in the samples heated to only 378 K, and that such local node structural changes generate sites that are still more exothermic in their reactions with Ca than are those described and computed above. As detailed structural data are not available for these local node distortions, we cannot construct specific examples—

particularly as they are likely associated with the dangling carboxylic acid functionalities at the film terminus and their potential changes in orientation associated with node distortions—but we speculate that this is a reasonable explanation for the reproducible variation in initial enthalpies of reaction/adsorption as a function of outgassing temperature.

The carbon LEIS signal increases over the first 2 ML of Ca coverage. This could be explained by changes to the amount of C exposed at the surface due to Ca reacting within the pores of the MOF, perhaps releasing aromatic groups that segregate to the surface, or a decrease in the He^+ ion neutralization probability at the surface due to adsorption of Ca, which probably lowers the work function, or both. Beyond 2 ML of Ca coverage, the Ca LEIS increase is mirrored by a slow decrease in the C signal toward zero.

The XPS Ca/C^0 peak area ratio increases to only a very small ratio over the first 1 ML of Ca coverage, indicating that Ca atoms diffuse below the external surface to react in NU-1000 beyond the XPS probe depth ($\lambda_C \approx 4.7$ nm). The Ca/C^0 peak area ratio increases even more slowly than seen for Ca growth on PCBM,[95] a system which saw diffusion of Ca atoms to a depth of >10 nm below the surface. Sample charging precluded a more thorough XPS analysis of the chemical state of NU-1000 with increasing Ca coverage, but there was qualitative evidence of oxygen being involved in some reaction as the O 1s peak shape was altered much more than the C 1s and Zr 3d peaks with increasing Ca coverage. These pieces of evidence suggest that the porous structure of NU-1000 promotes extensive diffusion of Ca below the external surface and its reaction with internal surfaces, prior to nucleation of Ca(s) at or near the external surface.

The enthalpy curve in **Figure 4.4** can be interpreted in terms of a simple two-step mechanism:

(I) a highly exothermic reaction of Ca with oxygen-containing species associated with the Zr_6 nodes within the MOF, and

(II) growth of Ca(s) clusters and nanoparticles on or near the external surface with an enthalpy change of about –178 kJ/mol.

A similar exponential-like decay in enthalpy with coverage as that seen here has always been observed for Ca adsorption on organic semiconductors and polymers,[22,23,25,26,28,30,95,119] and we attribute it to the same type of kinetic competition here as was used to explain those data. It reflects the decreasing probability for an incoming Ca atom to diffuse further below the external surface to find unreacted sites (oxygen-containing species) and its increasing probability to instead find a growing cluster of Ca(s) to which it attaches. Reaction I slows as these oxygen-containing groups near the surface get titrated by Ca. The density of nodes is very small (~0.23 nodes per nm^3), so the reaction proceeds to >10 nm depth (see below) before diffusion becomes too slow to compete effectively. Meanwhile, reaction II gets faster as the fraction of the external surface and near-surface covered with Ca(s) clusters increases. The enthalpy for reaction II dominates after 5 ML, and perhaps already by ~2 ML. The LEIS data in **Figure 4.2** show that only ~1% of the surface is covered by Ca(s) by 2 ML. We show below that nodes have already been reacted down to a depth of >10 nm at this 2 ML coverage.

We use this simple two-state model to explain the enthalpy data in **Figure 4.4** for samples baked to 348 K, and from this estimate the extent of reaction with internal-surface oxygen-containing groups on the nodes. This model assumes that the measured enthalpy changes in **Figure 4.4** result from only two contributing reactions: one with an enthalpy change equal to the initial enthalpy release of 513 kJ/mol and the other due to the formation of Ca(s) with an enthalpy release equal to ΔH_{sub} (178 kJ/mol). In this model, the measured differential enthalpy of adsorption at any

Ca coverage (ΔH_{ad}) is the sum of the fraction of Ca atoms in the pulse that reacts *via* node oxygen (*f*) multiplied by –513 kJ/mol and the remaining fraction, (1 - *f*), which makes Ca(s) particles, multiplied by $-\Delta H_{sub}$ (-178 kJ/mol):

$$\Delta H_{ad} = f\left(-513\frac{kJ}{mol}\right) + (1-f)(-178\frac{kJ}{mol}) \quad (4.3)$$

Solving for *f* at every Ca coverage results in the curve of *f* versus coverage shown in the top graph of **Figure 4.11**, which is identical in shape to the enthalpy curve in **Figure 4.4**, except $f = 1$ corresponds to -513 kJ/mol and $f = 0$ corresponds to –178 kJ/mol. Multiplying *f* by the Ca coverage *added* per pulse gives the amount of reacted Ca per pulse in ML which reacts at the node oxygens. Summing pulses from zero coverage up to any other coverage gives the total amount of "reacted Ca" (i.e., the amount that reacts with oxygen-containing groups at the nodes) at that coverage. This is plotted versus Ca coverage in the bottom graph of **Figure 4.11**. As seen, this amount increases gradually until saturating at 1.77 ML of "reacted Ca" at coverages above 7 ML.

We converted this "reacted Ca" coverage to the effective "reacted depth" by calculating the volume of the unit cell of NU-1000 (one hexagonal pore plus two triangular pores, two layers deep) to be 12.8 nm^3. Each unit cell contains 3 nodes, which gives the number density of nodes mentioned above (0.23 nodes per nm^3). Using the Ca ML definition of 7.4 x 10^{14} atoms/cm^2 and assuming a reaction stoichiometry of 4 Ca per node, we thus calculated the reacted depth of NU-1000 from the reacted Ca coverage, which saturates at ~14 nm. The progression of this reaction depth with coverage is also shown in the bottom graph of **Figure 4.11**. If instead we assume a reaction stoichiometry of 8 Ca per node, as seen for Al deposition *via* ALD,[85,86] we calculate a total reaction depth of ~7 nm.

Of course, there are several types of oxygen-containing functional groups at each node, so there may be a range of reaction enthalpies for Ca with these nodes, and not just this single value of –513 kJ/mol, equal in magnitude to the maximum (initial) enthalpy change assumed in equation 4.3. If we instead assume that the enthalpy for the "reacted Ca" has a range of values between –513 kJ/mol and –366 kJ/mol, which is the average enthalpy for the first 2 ML of Ca coverage and very close to the DFT enthalpies for reactions 4.1 and 4.2, the "reacted Ca" amount and depth increases. Replacing -513 kJ/mol in equation 4.3 with a value greater than or equal in magnitude to -366 kJ/mol leads to the results in **Figure 4.12**. This is quite similar to **Figure 4.11**, but extends to higher coverages and larger reacted amounts and depths (saturating instead at ~23 nm depth). Based on the DFT calculations, this modified two-state model in **Figure 4.12** better represents the real situation, with Ca reactions with RCOOH occurring initially (with exothermicity of 520 kJ/mol), followed by Ca reactions with $–OH_x$ on the nodes (with exothermicity of ~400 kJ/mol).

Based on its bulk crystal structure, the density of nodes in NU-1000 is 2.34×10^{20} nodes per cm^3. This gives a density of roughly 3.5×10^{13} nodes per cm^2 in the closest-packed layer (assuming close-packed spheres) and a layer-to-layer separation (layer thickness) of ~1.5 nm. Thus, the reacted depth of 23 nm corresponds to ~15 layers of nodes whose water and –OH groups react highly exothermically with Ca at saturation, after which the Ca only grows as Ca(solid) on the external surface.

CONCLUSIONS

Calcium vapor reacts initially with a high exothermicity (~-513 and ~-570 kJ/mol for samples outgassed at 348 K and 378 K, respectively), attributed to Ca reacting with carboxylic acid groups, free water, or both on the internal surfaces. The exothermicity slowly drops to -280 kJ/mol by 2

ML, attributed to a gradual switch to reaction of Ca with -OH_x on Zr_6 nodes deep below the external surface, with an average enthalpy of reaction equal to –366 kJ per mole of Ca. These reactions with the internal surfaces of the MOF nodes produce calcium salts. The very slow growth of Ca LEIS and XPS signals show that these reactions proceed to ~20 nm below the external surface before the diffusion of transiently adsorbed Ca atoms becomes too slow to find unreacted sites on the internal surfaces. Beyond 2 ML, the exothermicity of adsorption decreases exponentially to the sublimation enthalpy of Ca (178 kJ/mol), reaching this limit by 5 ML; this is attributed to the formation of Ca(solid) nanoparticles near and on the MOF's external surface.

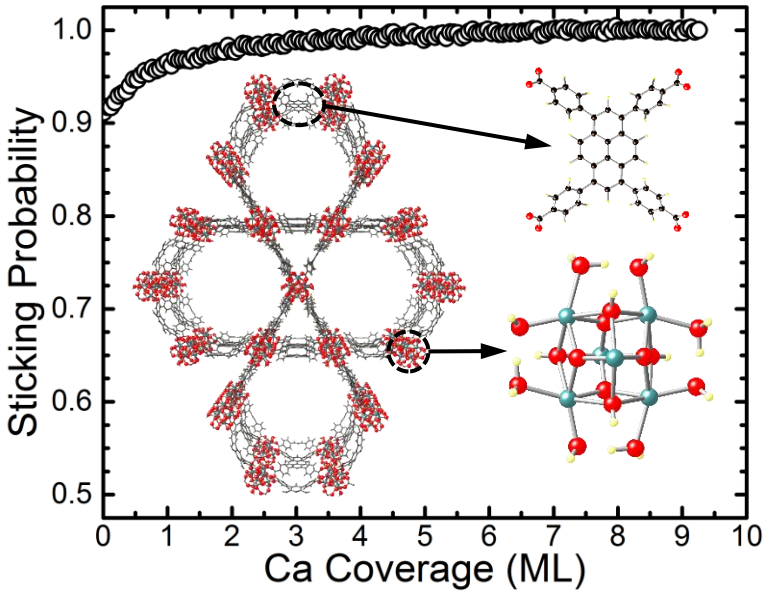

Figure 4.1. Measured sticking probability of Ca gas atoms on NU-1000 (outgassed at 348 K) as a function of Ca coverage at 300 K. Each data point represents a pulse of ~0.009 ML with a pulse frequency of 0.5 Hz. Monolayer coverage (1 ML) is defined as the Ca(111) packing density (7.4 × 10^{14} Ca atoms per cm^2). The inset shows the NU-1000 structure with the following color scheme: Zr, turquoise; O, red; C, black; H, cream.

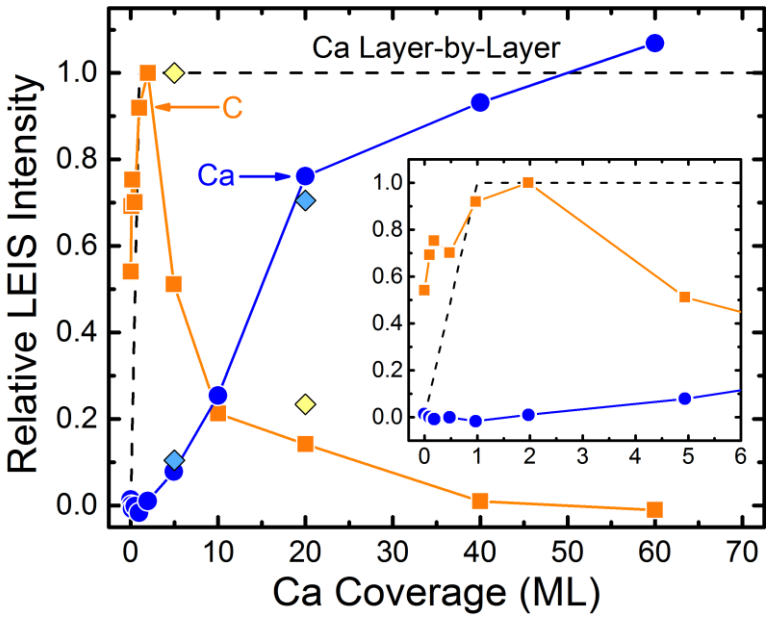

Figure 4.2. He^+ LEIS measurements of Ca growth on NU-1000 (outgassed at 348 K) at 300 K. The relative integrated LEIS peak intensities for Ca (blue circles) and C (orange squares) are displayed as a function of Ca coverage. Calcium intensities are normalized with respect to the saturation signal obtained for very high Ca coverages. Carbon intensities are normalized with respect to the signal obtained from a pristine NU-1000 sample. The dashed line indicates the Ca signal growth curve expected for a layer-by-layer growth model on a flat surface, such that the signal saturates at completion of the first ML. The inset shows a close-up of the low-coverage region. Diamond points were measured using 5-fold larger Ca coverage steps than round points, so that the sample was exposed to only 20% of the typical He^+ dose. Their agreement shows that ion-beam damage does not affect the data at the low ion doses used for normal data acquisition.

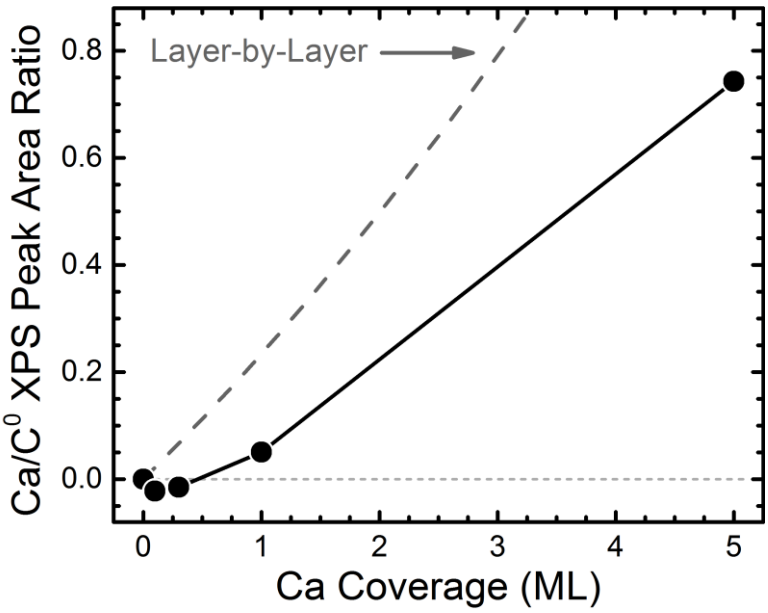

Figure 4.3. The ratio of the integrated area of the Ca 2p XPS peak to the initial C 1s peak as a function of Ca coverage on NU-1000 (outgassed at 348 K) at 300 K. The dashed line indicates the Ca/C^0 peak area ratio expected for layer-by-layer growth on a flat surface.

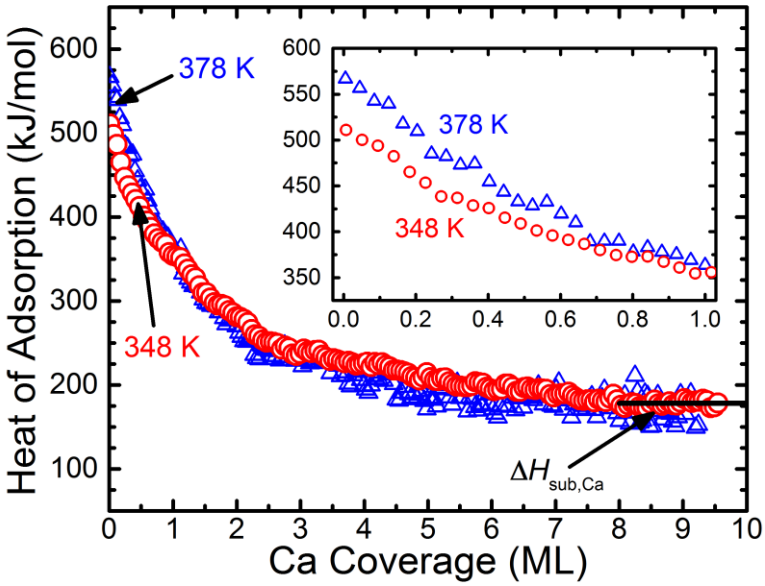

Figure 4.4. The differential heat of adsorption of Ca on NU-1000 at 300 K after baking at 348 K and 378 K in a preparation chamber with a base pressure of 2×10^{-9} mbar, plotted as a function of total Ca coverage. The heat of adsorption plotted here is the negative of the standard enthalpy of adsorption at 300 K. The inset shows a close-up of the region up to 1 ML Ca coverage.

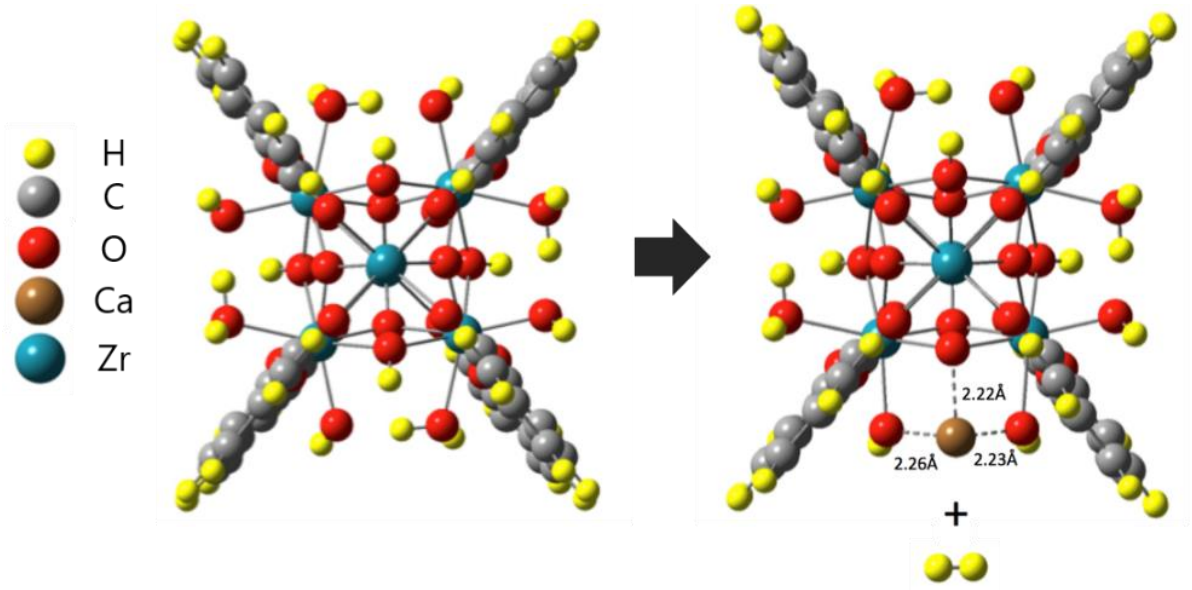

Figure 4.5. Predicted structures optimized in the cluster calculations but with the carbon coordinates frozen at their values from reference 158. (Left) The initial Zr_6 node with 8 attached benzoates (to model linkers), giving the cluster formula $[Zr_6(\mu_3\text{-}O)_4(\mu_3\text{-}OH)_4(OH)_4(OH_2)_4]^{8+}$. (Right) Final product, $[Zr_6(\mu_3\text{-}O)_5(\mu_3\text{-}OH)_3(OH)_5(OH_2)_3Ca]^{8+}$, formed during the reaction of Ca with a node-bound water-hydroxyl complex, which releases hydrogen, shown here in the form of dihydrogen (similar to the reactions in **Figure 4.8a** and **b**, see below). The released hydrogen may instead react with another Ca to make CaH_2 clusters (see text).

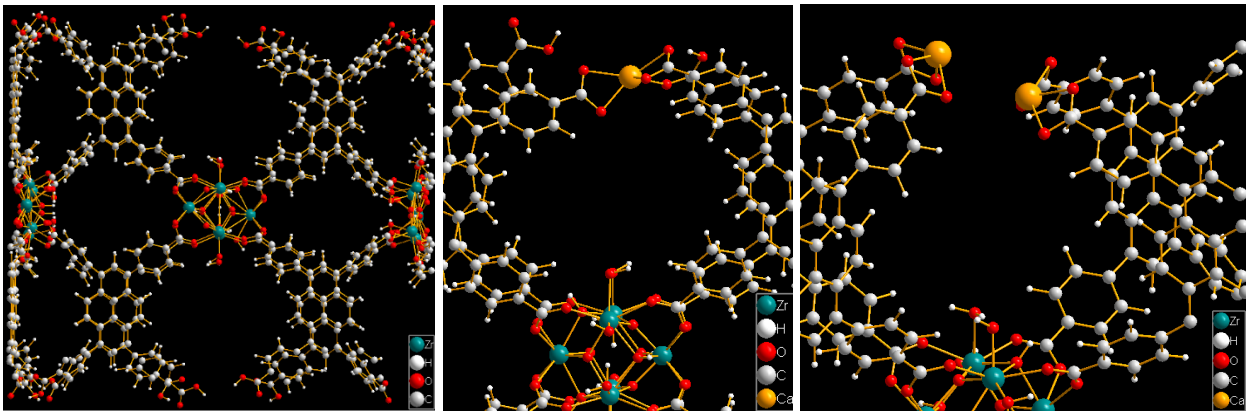

(a) (b) (c)

Figure 4.6. (a) The slab model of (001) surface of NU-1000 optimized in the periodic calculation with lattice constants constrained at bulk values. (b) 50% of surface benzoic acid reacting with Ca. (c) 100% of surface benzoic acid reacting with Ca.

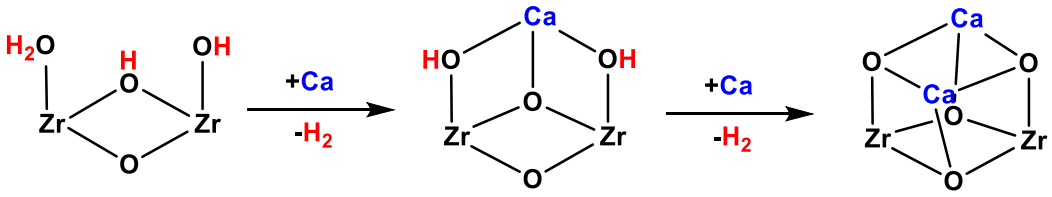

Figure 4.7. The most stable proton topology on the face of the Zr_6 node of NU-1000 and the proposed products of Ca reacting with protons. Only one of four faces of the Zr_6 node with $–OH_x$ is shown.

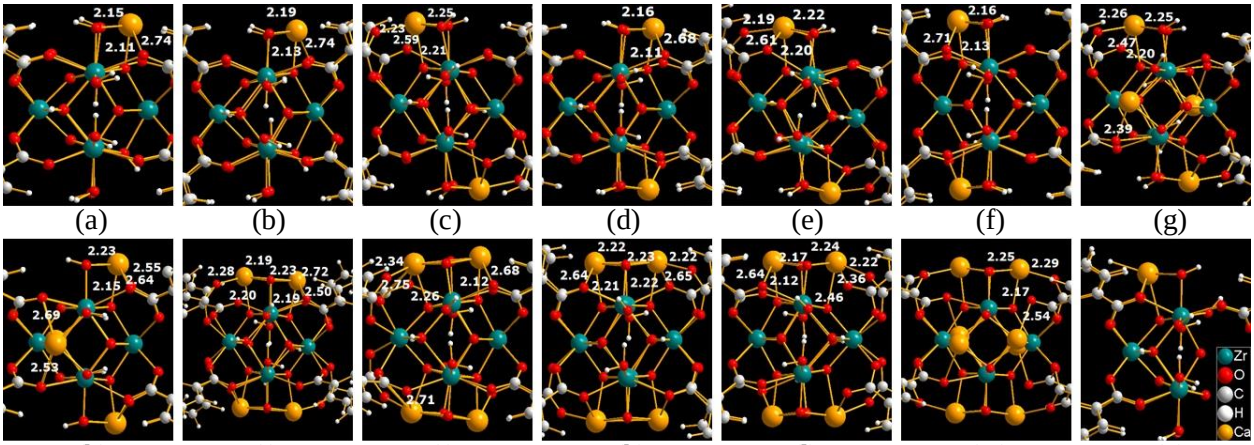

Figure 4.8. The product of Ca reacting with different numbers of protons on the Zr_6 node optimized in the periodic calculation (as listed in **Table 4.1**). Some Ca-O distances are marked. (a) 1 Ca in the large pore; (b) 1 Ca in the small pore; (c) 2 Ca in the large pore with C_i symmetry; (d) 2 Ca in the large pore with C_2 symmetry; (e) 2 Ca in the small pore with C_i symmetry; (f) 2 Ca in the small pore with C_2 symmetry; (g) 4 Ca, 1 Ca per face with C_i symmetry; (h) 4 Ca, 1 Ca per face with C_2 symmetry; (i) 4 Ca in the large pore with C_i symmetry; (j) 4 Ca in the large pore with C_2 symmetry; (k) 4 Ca in the small pore with C_i symmetry; (l) 4 Ca in the small pore with C_2 symmetry; (m) 8 Ca in both pores; (n) hydride formation in large pore.

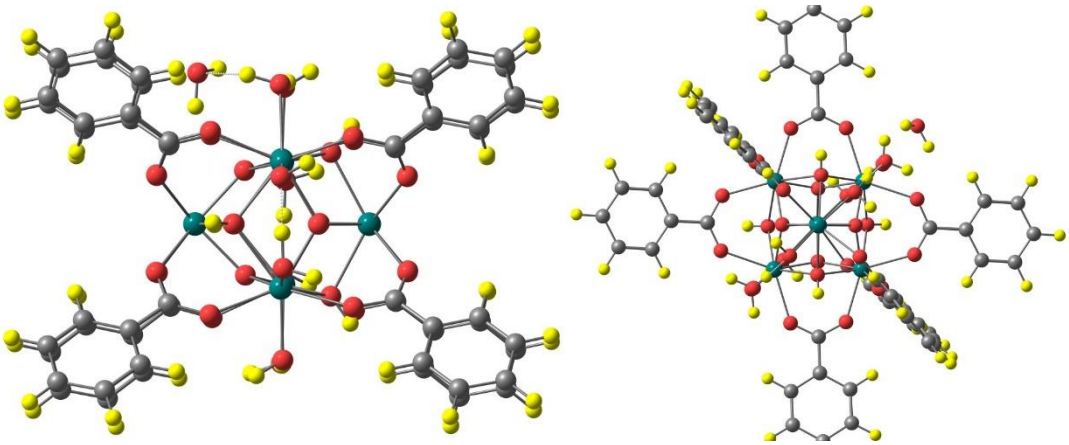

(a) (b)

Figure 4.9. The optimized cluster models of water making hydrogen bonds with Zr_6 nodes.

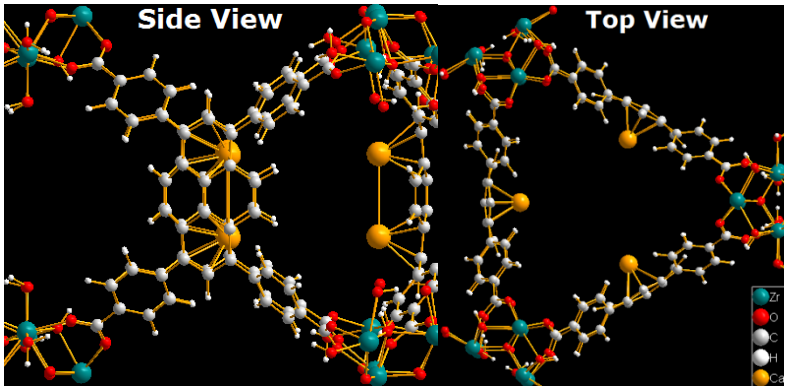

(a)

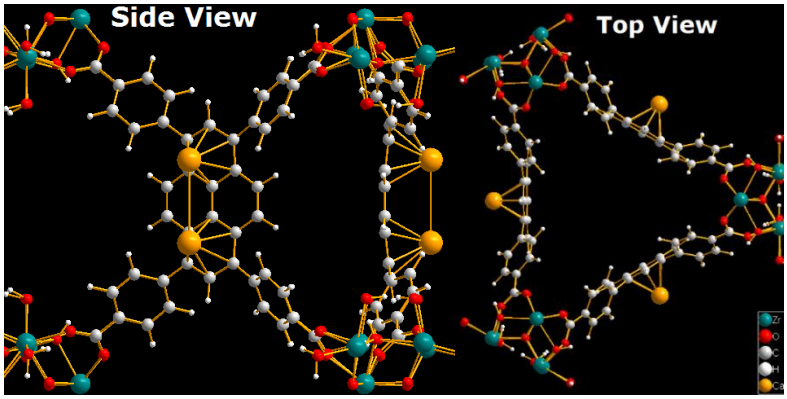

(b)

Figure 4.10. Two Ca deposited on pyrene optimized in the periodic calculation (as listed in **Table 4.1**): (a) inside the triangular pore; (b) outside the triangular pore.

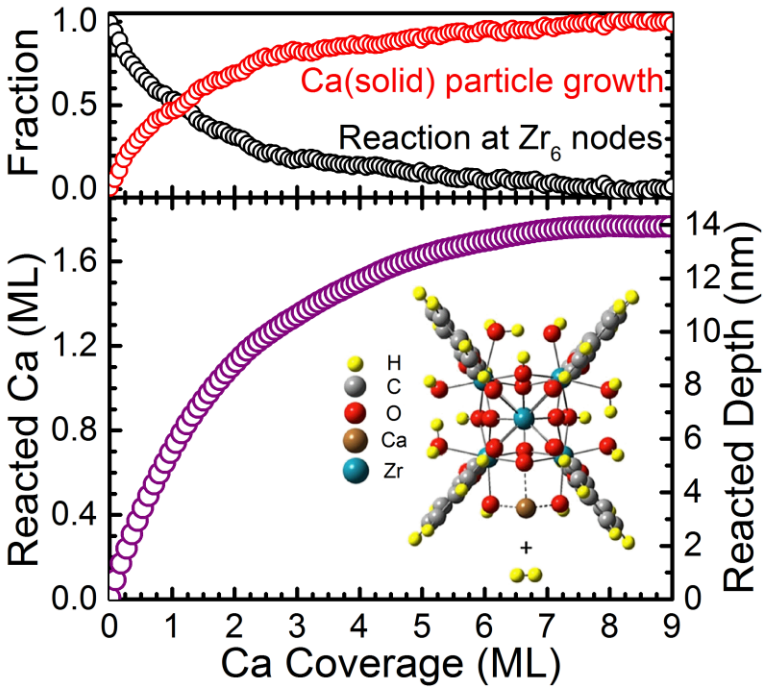

Figure 4.11. Top graph shows the fraction of Ca atoms that react with high heat (513 kJ/mol) within NU-1000 outgassed at 348 K (*f*, black points) and the fraction that grow as 3D Ca(solid) particles as a function of total Ca coverage at 300 K (1-*f*, red points), estimated from the heat versus coverage data as analyzed with a simple two-state model (see text). The bottom graph shows the corresponding cumulative amount of Ca that reacts with the Zr_6 node of NU-1000; it is plotted as a function of total Ca coverage at 300 K, shown in ML of Ca (left axis) and reacted depth in nm (right axis), which is calculated by assuming that 4 Ca atoms react per Zr_6 node. These values for the "reacted" amount and depth are clearly lower limits since many reaction heats less exothermic than -513 kJ/mol are seen in the highly exothermic "reactions."

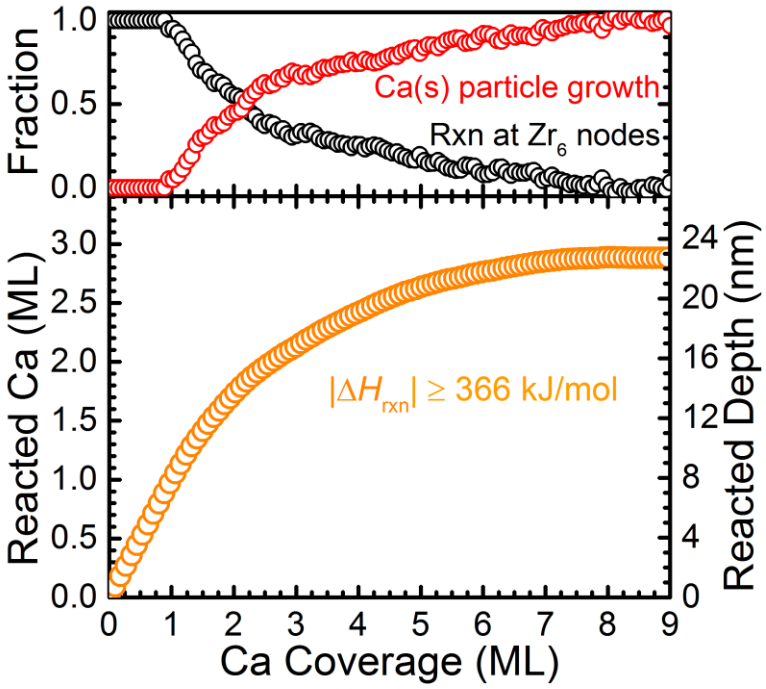

Figure 4.12. The top graph shows the fraction of Ca that react at –OH and H_2O groups on the Zr_6 nodes with a reaction heat of $|\Delta H_{rxn}| \geq 366$ kJ/mol (the average heat of adsorption over the first 2 ML of Ca coverage) within NU-1000 at 348 K (*f*, black points) and the fraction that grow as 3D Ca(solid) particles as a function of Ca coverage at 300 K (1-*f*, red points), as estimated from the heat versus coverage data analyzed with the same two-state model used for **Figure 4.11**, except the reaction heat was changed from 513 kJ/mol to ≥ 366 kJ/mol (see text). The bottom graph shows the corresponding cumulative amount of Ca that reacts with the Zr_6 node of NU-1000 with a reaction heat of ≥ 366 kJ/mol plotted as a function of total Ca coverage at 300 K, shown in ML of Ca (left axis) and reacted depth in nm (right axis) assuming 4 Ca atoms react per Zr_6 node.

TABLE

Table 4.1. Heats of Reaction at T = 0 K for Ca Vapor Reacting with Different Functional Groups on the External and Internal Surfaces of NU-1000,[a] as Calculated with Periodic and Cluster-Based DFT Methods[b]

reactant	description	model type (figure number for product structure)	product	reaction enthalpy (kJ/mol)
benzoic acid	50% surface H	periodic (6b)	H_2+Ca^{2+}	-538
benzoic acid	100% surface H	periodic (6c)	H_2+Ca^{2+}	-500
benzoic acid	gas phase	cluster (none)	H_2+Ca^{2+}	-531
-OH_x	1 Ca in large pore	periodic (8a)	H_2+Ca^{2+}	-421
-OH_x	1 Ca in small pore	periodic (8b)	H_2+Ca^{2+}	-421
-OH_x	1 Ca in large pore	cluster (5)	H_2+Ca^{2+}	-395
-OH_x	2 Ca in large pore, C_i sym.	periodic (8c)	H_2+Ca^{2+}	-436
-OH_x	2 Ca in large pore, C_2 sym.	periodic (8d)	H_2+Ca^{2+}	-419
-OH_x	2 Ca in small pore, C_i sym.	periodic (8e)	H_2+Ca^{2+}	-424
-OH_x	2 Ca in small pore, C_2 sym.	periodic (8f)	H_2+Ca^{2+}	-417
-OH_x	4 Ca, 1 Ca per face, C_i sym.	periodic (8g)	H_2+Ca^{2+}	-459
-OH_x	4 Ca, 1 Ca per face, C_2 sym.	periodic (8h)	H_2+Ca^{2+}	-417
-OH_x	4 Ca in large pore, C_i sym.	periodic (8i)	H_2+Ca^{2+}	-382
-OH_x	4 Ca in large pore, C_2 sym.	periodic (8j)	H_2+Ca^{2+}	-388
-OH_x	4 Ca in small pore, C_i sym.	periodic (8k)	H_2+Ca^{2+}	-370
-OH_x	4 Ca in small pore, C_2 sym.	periodic (8l)	H_2+Ca^{2+}	-379
-OH_x	8 Ca in both pores	periodic (8m)	H_2+Ca^{2+}	-393
-OH_x	hydride formation in large pore	periodic (8n)	Ca-H	-311
-OH_x	hydride formation in large pore	cluster (none)	Ca-H	-349
pyrene	2 Ca inside small pore	periodic (10a)	Ca_2^+···pyrene$^-$	-49
pyrene	2 Ca outside small pore	periodic (10b)	Ca_2^+···pyrene$^-$	-45
pyrene	2 Ca on 1,3,6,8-tetrakis-(phenyl)pyrene in gas phase	cluster (none)	Ca_2^+···pyrene$^-$	-62

[a]Thermocorrections obtained from the frequency calculation in the cluster model were applied to the energy calculated in the periodic model to obtain the approximated reaction enthalpy. All results are in kJ per mole of Ca. [b]All of the groups represent internal surface sites except benzoic acid, which represent unreacted linkers on the external surfaces of MOF particles.

Chapter 5. Direct Measurement of Half-Cycle Reaction Heats during Atomic Layer Deposition by Calorimetry

This chapter is reprinted with permission from reference 189: J. M. Lownsbury, J. A. Gladden, C. T. Campbell, I. S. Kim, A. B. F. Martinson, **2016**, *in preparation.*

CHAPTER ABSTRACT

We present a new calorimeter that approaches the ideal limit of a heat detector whereby the signal at any time is proportional to the heat power being delivered to the sample, and prove its sensitivity for measuring heats of ALD half-reactions. The heat dynamics of amorphous Al_2O_3 growth via sequential self-limiting surface reaction of trimethylaluminum (TMA) and H_2O is clearly resolved. Calibration enables quantitation of the exothermic TMA and H_2O half-reactions with high precision, -413 kJ/mol and -181 kJ/mol, respectively. Simultaneous quartz crystal microbalance measurements provide an overall mass gain of 40.0 ng/cm^2 with 35.3 ng/cm^2 gained during the TMA half-reaction. These heats versus extent of reaction show that TMA preferentially reacts to first to produce two methanes and form monomethylaluminum bound to the surface through four oxygen atoms, but near saturation, it produces only a single methane and dimethylaluminum bound to the surface through a single oxygen. The broad applicability of this novel calorimeter is further demonstrated through excellent signal-to-noise ratios of less exothermic ALD half-reactions to produce TiO_2 and MnO_x.

INTRODUCTION

Atomic layer deposition (ALD) is now a versatile and ubiquitous technique for depositing uniform thin films of precision thickness with exceptional conformity to underlying substrates, even when they are exceedingly rough or porous.[79,80,190,191] ALD has been used to deposit thin films of oxides,[79,80] sulfides,[192] nitrides,[193] and pure metals,[193] among other compounds,[79,194] and has been applied to a wide range of fields including semiconductors,[80,195-197] batteries,[198-202] photovoltaics,[203-206] and catalysis.[85-87,207-209] According to ISI Web of Science, the number of citations to papers that have "atomic layer deposition" or "atomic-layer deposition" in their topic is growing exponentially, from ~1000 in 2005 to >32,000 in 2015. As a chemical vapor deposition technique, ALD benefits from the development of several families of volatile and reactive metal-organic and metal-halide precursors that span the periodic table. Unique to ALD is the sequential, self-limiting surface reactions that are most commonly separated in time by inert gas purging.[79] By cycling a [precursor A–purge–precursor B–purge] process, each vapor phase chemical is reacted, in turn, with a precisely functionalized surface that remains from reaction with the previous precursor. Once all relevant surface functional groups have been reacted, any excess precursor purged away, limiting the growth per cycle to a precise—typically sub-monolayer—atom addition during each half-cycle. Although its acronym brands it a "deposition" method like its distant physical vapor deposition cousins, the self-limiting covalent attachment scheme is more accurately described as a surface synthetic technique. As such, deductions of detailed reaction mechanisms are accessible *via* the traditional toolbox of a chemist—*in-situ* mass spectrometry and surface analysis techniques like infrared spectroscopy, and *ex situ* methods including X-ray photoelectron spectroscopy. Here, we extend the list of chemically-relevant characterization techniques for ALD to include *in situ* adsorption calorimetry for the first time, and demonstrate its

high sensitivity, excellent signal-to-noise and fast time response (~1 ms) by probing the heats of ALD half-reactions during the growth of three different oxide films (Al_2O_3, TiO_2, and MnO), and in calibration experiments with fast light pulses.

We further demonstrate the utility by of this new calorimeter by quantitatively determining the heats associated with each of the half-cycle reactions during the growth of thin Al_2O_3 films *via* alternate dosing of the two precursors, trimethylaluminum (TMA) and H_2O, at 125°C, providing new insight into the half-reaction mechanisms. We analyze these calorimetric results as a detailed function of coverage below, where we show that they reveal unprecedented detail regarding the nature of the adsorbed intermediates and how they change with coverage in each half cycle as the reaction proceeds toward saturation.

The ALD adsorption calorimeter developed here is inspired by the techniques developed by the groups of D. A. King[210] and C. T. Campbell[27,94,99] for using pyroelectric heat detection in adsorption calorimetry.

The most extensively studied ALD reaction scheme is the formation of amorphous Al_2O_3 *via* alternating exposure of surfaces to TMA and H_2O vapor, and we use it here to demonstrate the mechanistic information content of this new calorimetry method. The reaction mechanism is well known to occur by alternating surface hydroxyl and methyl termination,[79,80,88,211-213] which can be approximately written as:

$$(*OH)_x + Al(CH_3)_3 \rightarrow *O_x–Al(CH_3)_{3-x} + x\ CH_4 \quad \text{(A)}$$

$$*O_x–Al(CH_3)_{3-x} + 3/2\ H_2O \rightarrow *O_{3/2}–Al–(*OH)_x + (3-x)\ CH_4 \quad \text{(B)}$$

$$Al(CH_3)_3 + 3/2\ H_2O \rightarrow ½\ Al_2O_3 + 3\ CH_4 \quad \text{(NET)}$$

where the asterisks indicate surface species, and in the case of "*****$O_{3/2}$–Al", a surface oxygen of the alumina lattice. We will refer to Reactions A and B as the TMA and H_2O half-reactions, respectively. The variable *x* represents the extent of the methane-releasing reaction that occurs in Reaction A with values typically between 1.5 and 1.7 (estimated experimentally).[79,88,214] Reaction B includes a rearrangement of oxygen in the newly formed surface to maintain Al_2O_3 stoichiometry.[88] We have omitted here specifically designating any bonds between the aluminum atom and oxygen atoms of the alumina lattice's surface (but analyze the number of those below). This NET Reaction for the ALD of Al_2O_3 has a very large exothermicity, which enables exergonic reactions at low temperatures (even as low as 33°C[213]) without a large effect on growth rate or film integrity.[88] The extent of reaction that occurs during Reaction A can be determined using a quartz crystal microbalance (QCM) to measure the mass gain per reaction step.[88,213-215] Gröner *et al.*[213] found that an ideal temperature for Al_2O_3 ALD growth was near 125°C, but very little change in growth rate was observed between 102 and 177°C.

An idealized scheme of the Al_2O_3 ALD reaction, under our reaction conditions, is shown in **Figure 5.1**. Briefly, gaseous TMA is introduced to an OH-terminated surface where it reacts to produce a surface-bound dimethylaluminum (DMA) or monomethylaluminum (MMA) species, gaseous CH_4, and heat. Upon saturation of this reaction, the surface is methylated.[79] Following a nitrogen purge step to remove excess TMA and CH_4 byproduct, water vapor is introduced where it reacts with the methylated surface to produce OH-terminated alumina, more gaseous CH_4, and more heat. After purging the chamber of H_2O and CH_4, this cycle may be repeated until the desired film thickness is achieved.

Figure 5.1 shows an example case where $x = 5/3 = 1.67$ in Reaction A for simplicity. The hydroxyl density is not to scale. The surface concentration of hydroxyls affects the value of *x*.[216]

Under typical conditions (T = 200°C, surface hydroxyl concentration = ~8.7 OH/nm^2), TMA molecules will lose 1.5 CH_3 ligands on average (releasing x = 1.5 CH_4) during the surface reaction,[214,216] and we find an average value at 125˚C of 1.7 below, which has also been seen experimentally.[214] Steric hindrance has been shown to limit the reaction to between 70-80% of the theoretical maximum packing density of dissociatively-adsorbed TMA *via* Reaction A.[79]

The details of bonding of the adsorbed intermediates (e.g., MMA and DMA) to the surface are not known experimentally, but they have been studied theoretically.[217-224] Widjaja and Musgrave[217] used cluster density functional theory (DFT) to estimate both half-reaction and transition state energies. Using periodic DFT, the Elliott group[218-220] modeled the TMA half-reaction on various Al_2O_3 surfaces to determine the effect of surface hydroxyl concentration on reaction energetics. Shirazi and Elliott[221] studied the effects of adjacent surface-bound TMA intermediates on proton transfer during both TMA and H_2O half-reactions. Weckman and Laasonen[222] used periodic DFT to study the TMA and H_2O half-reaction intermediates on α-Al_2O_3 with a surface hydroxyl concentration similar to that observed experimentally. Sandupatla *et al.*[223] published a similar study on the γ-Al_2O_3 surface, which better represents the amorphous surface produced during ALD than α-Al_2O_3. These studies found the TMA half-reaction to be more highly exothermic than the H_2O half-reaction, consistent with our calorimetry results below.

Although some mechanistic details of the ALD growth of Al_2O_3 *via* alternating exposures of TMA and H_2O are well understood, the heats of reaction during ALD half-reactions have never been quantified experimentally, nor have any heats been measured to date for any of the scores of other ALD processes known. There has been one report of a prior attempt to calorimetrically measure reaction heats during ALD using a thermopile to measure transient temperature rises.[225] However, the sensitivity and precision of that instrument was not sufficient to provide meaningful

heats, so that, to our knowledge, there have been no follow-up papers using it in the 5 years since it was reported.

Though many theoretical studies of the TMA–H_2O process and other ALD processes have been derived from first principles computation (DFT),[217-224] the calculated heats associated with each reaction scheme remains untested compared to experiment. The ability to experimentally determine the heats of ALD half-reactions, which we demonstrate here for the first time, will help to fully elucidate these mechanisms and the detailed nature of the surface intermediates produced. This will also provide crucial benchmarks for theory studies of ALD processes in general, as we show here for this specific ALD reaction, and may prove useful in ALD process monitoring and control. Reliable measurements of ALD half-reaction heats will also provide very practical insight into the potentially damaging effect of transient temperature spikes on high surface-to-volume ratio structures[85-87] as well as many intrinsically temperature-sensitive substrates.[81,213,226-230]

EXPERIMENTAL

Experiments were performed in a Savannah S200 ALD system (Cambridge Nanotech), a basic thermal ALD tool designed for wafers that we have modified to accommodate *in situ* QCM[215] and the coating of powders[86] Nitrogen was used as a carrier gas after passing through an in-line Entegris inert gas Ni filter and through the inlet manifold at a continuous flow rate of 20 sccm to maintain a base pressure of ~0.3 Torr, as measured by a BOC Edwards APGX-H linear convection pressure gauge. Trimethylaluminum (TMA, 97%, Sigma Aldrich), tetrakis(dimethylamino)-titanium (TDMAT, 99.998%, Sigma-Alrich), bis(ethylcyclopentadienyl)manganese ($Mn(CpEt)_2$, min. 98%, Strem) (see **Table 5.1** for structures) and water (ultrafiltered) were loaded into 50 mL stainless steel cylinders. The liquid precursors were housed beneath the ALD chamber, variably

heated—with the exception of TMA [Danger: TMA can decompose and pressurize upon heating in a sealed vessel]—and volatilized under their own vapor pressure to mix with the N_2 carrier gas in stainless steel tubing upon ALD valve actuation. The inlet manifold, which combines six channels to a single inlet to the substrate and sensor chamber, was heated to 125°C. All experiments were performed with the ALD chamber heated to 120°C, except for the TMA–H_2O experiments which were performed at 125°C (and 130°C in one set of control experiments). All experiments were carried out in normal pulse mode with continuous N_2 flow into uninterrupted rough vacuum pumping. The deposited mass of the precursors was monitored using two quartz crystal microbalances (QCM, Inficon SQM-160 monitor) mounted on the chamber lid with one situated near the inlet and one near the exhaust, as described previously.[215]

A schematic of the custom calorimeter fixture is shown in **Figure 5.2**. The pyroelectric heat detector is a 50 μm thick $LiTaO_3$ crystal coated on both sides with ~25 nm of gold (Del Mar Photonics). The crystal rests on a stainless steel stand with a spot-welded signal wire. The stand has a hole bored out through its center to reduce its thermal mass. A large thermal mass acts as heat sink for the calorimeter, reducing the signal intensity. The stand is electrically isolated from the rest of the calorimeter fixture by the $LiTaO_3$ crystal on top and a 2.54 cm diameter Macor ceramic disk below. The roughness of the Macor disk allows for trapped gases within the stand to be pumped out gradually, avoiding a large pressure differential across the faces of the brittle crystal, while simultaneously making diffusion of ALD precursor gases to the back face of the detector crystal very slow. Thus, we interpret the measured heats as being associated with the front surface area only. All three pieces are sandwiched between a circular base and annular top constructed of aluminum which are connected together using three screws separated radially by 120°. The top piece has a central 8.66 mm diameter orifice which exposes the 10 mm diameter

$LiTaO_3$ crystal to gases in the ALD chamber. The top face of the crystal is grounded to the chamber through the aluminum housing.

The measured voltage signal is fed from the vacuum side to atmosphere by a BNC feedthrough in the form of a KF adapter on the outlet plumbing approximately 20 cm downstream of the sensor. The measured signal is amplified by a homebuilt preamplifier similar to that used in our earlier adsorption calorimeters[27,94,99,114,115] with very low input noise, an input impedance of >10 GΩ, and a gain of 100, followed by an amplifier with adjustable settings for the polarity, time constant (τ = 0.5, 5, and 25 s), and gain (0-1000). The total combined gain from these amplifiers in series can range from 0 to 100,000. The 25 s time constant was used for all experiments. These electronics are similar to those previously reported to measure heats of adsorption of metals and molecules on various surfaces in ultrahigh vacuum.[27,94,99,114,115]

The calorimeter was calibrated *in situ* by shining ~25 ms light pulses onto the alumina-pre-coated heat detector through a custom chamber lid with a glass window, and measuring the heat signal. The true voltage is determined by dividing by the total gain (100 from the preamplifier times 30 from the adjustable amplifier), as plotted in **Figure 5.3**. All heat signals presented below are converted to true voltages by dividing by the total gain used during the experiment. As this paper describes our first proof-of-concept experiments, a simple white light flashlight was used as the calibration light source. Absolute calibration would be much more accurate using a stabilized, single-wavelength light source such as the HeNe laser used to calibrate previous adsorption calorimeters,[27,94,99,114,115] as the absolute power is easier to measure with a photodiode and the sample's optical reflectivity does not vary at a single wavelength (see below).While an intensity-stabilized HeNe laser (with the beam expanded to match the detector surface area) is preferred, lasers are not permitted in the lab housing this *in situ* experiment. The calorimeter was exposed to

20 consecutive, nearly square-wave light pulses with a repeat period of 10 s, controlled by an electronic shutter with a 6 mm aperture (Uniblitz LS6T2). The intensity of the light source was attenuated by a glass slide which added ~6% reflectivity, and neutral density filters, ND 0.03 and ND 1.0 (Thorlabs), which have rated transmissions of 50.1% and 10%, respectively. The detector response is also nearly a square wave with pulse width equal to the electronic shutter, showing the very fast time response of this detector and associated preamplifier circuit. *This means that it approaches the ideal limit of a heat detector whereby the signal at any time is proportional to the heat power being delivered to the sample*. This is, however, complicated by the fact that after the heat pulse, the signal goes negative, but at such a low intensity that it cannot be seen in **Figure 5.3**. This negative signal decays exponentially back to baseline with a time constant equal to that of the preamplifier (set at 25 s here) and, when integrated for a time that is very long compared to 25 s, the negative-going area equals the positive-going area seen at short times (during the light pulse). This is expected based on the preamplifier design; we also proved it by using shorter time constants which makes the negative-going signal increase in magnitude but decay more quickly, so it is easier to integrate.

Since the positive signal is proportional to the heat power at the sample, one can integrate it versus time to get the net heat energy absorbed by the sample. The inset in **Figure 5.3** shows the integrated heat signals versus the absorbed heat calculated from the light intensity and optical absorbance of the sample. The heat signal for each light intensity is integrated only up to the time where it went negative. However, the exact termination of this integral is not crucial, as the calculated integrals decrease by only ~8-12% when integrated for 0.5 s after the light pulse has clearly ended (short compared to the 25 s time constant).

The reflectivity of the detector surface (i.e., gold-coated $LiTaO_3$ with a ~7 nm thick Al_2O_3 overlayer) over the wavelength range of the light pulses was measured with a variable angle spectroscopic ellipsometer (Woolam M-2000, wavelength range 380-1000 nm) operating in reflectivity mode. The wavelength-averaged reflectivity is ~0.70. The power of the light source was measured by a photodiode (Ophir PD300-3W) in place of the calorimeter in the same configuration and using the same filters. The light pulse energy is obtained by multiplying the photodiode power by the aperture open time of 24.7 ms (i.e., the full-width at half-maximum of the signals in **Figure 5.3**). Multiplying the energy by the wavelength-averaged absorptivity (i.e., one minus the reflectivity, 0.30) gives the approximate energy absorbed by the calorimeter detector in joules. The calorimeter "sensitivity" is determined by plotting the time-integrated voltage signals from **Figure 5.3** vs. the light energy absorbed by the sample for each filter, as shown in the inset of **Figure 5.3**. The slope is 0.1092 ± 0.0015 Vs/J. This ~1.5% standard deviation reflects on the precision of the calibration, dictated by error in the unfiltered pulses (1.4%). (The precision in the energy (x-axis) is 0.6%.) The absolute accuracy is much worse (~24.7%, see below), due to the errors in measuring the white light's power and wavelength-averaged reflectivity of the sample. As noted above, this will be improved in future work using a stabilized HeNe laser instead of a white light source. This slope (sensitivity) can be used to convert the time-integrated voltage signals measured during ALD into absorbed energy.

Another way to calibrate the absolute sensitivity of the heat detector is to use a reaction of known net heat. We do this below using the ALD of Al_2O_3 from TMA and H_2O and get a sensitivity of 0.145 Vs/J, which is 24.7% lower than that estimated using the flashlight above.

For comparison, we can calculate a theoretical sensitivity of the $LiTaO_3$ crystal using its pyroelectric coefficient (1.9×10^{-8} C/cm^2 K), heat capacity (424 J/kg K), density (0.00746 kg/cm^3)

and thickness (0.005 cm), giving 1.2 x 10^{-6} C/J. The measured capacitance of our system at the electrical feedthrough (i.e., the signal fed into the preamplifier) is 0.57 nF. Dividing the above sensitivity in C/J by the capacitance gives a sensitivity of 2109 V/J. Multiplying this by the unfiltered, absorbed energy plotted in the inset of **Figure 5.3** (121 μJ) gives 0.255 V. This is the theoretical maximum voltage rise that would be measured by the calorimeter (with no cooling or current drain) when 16.2 mW of light is shined for 24.7 ms on the detector surface with an absorptivity of 0.30. The rise of this theoretical signal with time would be linear up to 255 mV while the pulse is on, and after the light is shut off, the heat signal would remain at 255 mV. However, the sample is efficiently cooled by its contact with the sample holder and surrounding gases, so its temperature and resulting voltage do not rise near this much. As shown in **Figure 5.3**, during a 24.7 ms unfiltered light pulse, our experimental signal rises quickly to a steady state voltage of only 0.57 mV, or 400-fold smaller. That is, the heating and cooling of the sample already balance each other when the sample temperature has increased to only ~1/400th of the hypothetical value with no cooling, due to the strong cooling by the heat sink of the calorimeter housing and the continual N_2 flow. This strong cooling also returns the signal to baseline quickly after the end of the light pulse.

For all ALD experiments, the reaction chamber (including fixture and crystal) was prepared prior to calorimetry by many cycles of the selected ALD process in order to build up a continuous multilayer coating of the film material and thus achieve homogeneous and steady state growth during each cycle. Several identical micro-doses (i.e., pulses) of the same precursor were used to fully saturate each surface half-reaction prior to moving to the alternate precursor, following a $(t_1–t_2)_n–(t_3–t_4)_n$ routine where t_1 is the metal precursor pulse time, t_2 is the metal precursor purge time, t_3 is the H_2O pulse time, t_4 is the H_2O purge time, and n is the number of micro-doses of the

same precursor. All times are in seconds. For example, one cycle of TMA–H_2O to produce Al_2O_3 followed a $(0.1–15)_{10}$–$(0.1–15)_{10}$ sequence. All experimental growth conditions are listed in **Table 5.2**.

We describe "open-valve" and "closed-valve" experiments below which refer to the manual valves that separate the precursors from the computer-controlled pneumatic (ALD) valves. The primary TMA–H_2O experiments discussed here were performed with these manual valves temporarily closed to allow a controlled volume of headspace to be delivered during each pulse. In detail, the manual valve (for the precursor that is to be pulsed) was opened to allow precursor equilibration in the headspace just upstream of the ALD valves, and closed again just prior to opening the ALD valve for each pulse, thereby limiting precursor delivery to only that vapor in the small constant volume between the manual valve and the ALD valve. This practice has the benefit of decoupling the precursor dose size from the timing precision of the ALD valves. This practice resulted in more reproducible pressure pulses and heat signals as well as achieving a smaller pulse than is possible with a high vapor pressure precursor and ALD valve pulse with a reproducible lower limit of 15 ms. Under normal operation these manual valves are usually fully open (i.e., "open-valve"), such that the number of precursor molecules delivered in a single pulse is controlled by the actuation time of the ALD valve and, for long pulse lengths, the rate of evaporation of the precursor and its flow rate through the tubes connecting the liquid source to the ALD chamber. We tested the effect of this difference in valve position, and found no differences in heat signal beyond that expected from a larger dose size per pulse in the valve-open mode (see below).

To also test for any effect that the opening of each actuated ALD valve itself may have on the calorimeter signal (i.e., due to its detector's piezoelectric response to mechanical noise), the

ALD valves were repeatedly opened and closed without any precursor gas in the headspace, with no observed signal on the calorimeter detector.

ALUMINA FILM GROWTH *VIA* ALD OF TMA AND H_2O

Quartz Crystal Microbalance

The mass adsorbed on the calorimeter during each half-cycle must be known in order to determine the molar enthalpy of each half-cycle. We also must confirm that each half-cycle has fully saturated the surface before moving onto the next half-cycle. Both of these tasks are accomplished by averaging the measurements from two *in-situ* QCMs located slightly upstream and downstream from the detector surface, the details of which have been described previously.[215] This QCM average approximates the growth behavior on the calorimeter, which presents the same surface chemistry and is exposed to the same precursors simultaneously. The average of five consecutive cycles of TMA and H_2O deposition at 125°C, measured on both QCMs, is shown in **Figure 5.4**. The mass gain over the course of 10 TMA pulses saturates at ~35.3 ng/cm^2, indicated by a flattening of the curve. The moderately lower QCM signal quality relative to previously published results[215] from the same system is a result of the long time over which each ALD cycle is completed (300 sec vs. typical 20 sec), the numerous pressure transients (20 pulses) that produce a temporary but reversible deviation in the apparent mass, and the "closed-valve" routine itself, which produces vibrations that are picked up by the QCMs. Upon averaging, these artifacts are largely removed and the overall mass gain per half cycle can be accurately determined. The TMA reacts with surface hydroxyls to add aluminum and methyl to the surface and release CH_4, which leaves as a gas (see Reaction A). The H_2O half-cycle releases the remaining methyls as CH_4 gas and re-hydroxylates the surface with a net mass gain of ~4.7 ng/cm^2. The overall mass gain per cycle is

~40.0 ng/cm^2. These QCM results are similar to previous experiments we performed at 100°C, 125°C, and 130°C, and agree well with previous experiments in the literature.[88,213]

The extent of methyl loss that occurs during each half-reaction is defined for the value of the stoichiometric coefficient *x* in Reactions A and B as written above. As shown previously[88,214]

$$\frac{\text{mass gain in Reaction A}}{\text{mass gain overall}} = \frac{72\ \left[\frac{\text{g TMA}}{\text{mol Al}}\right] - 16\,x\ \left[\frac{\text{g CH}_4}{\text{mol Al}}\right]}{51\left[\frac{\text{g Al}_2\text{O}_3}{\text{mol Al}}\right]} = \frac{35.3\ \left[\frac{\text{ng}}{\text{cm}^2}\right]}{40\ \left[\frac{\text{ng}}{\text{cm}^2}\right]} \Rightarrow x = 1.7 \qquad (5.1)$$

Therefore, on average 1.7 of the three CH_3 groups per TMA molecule react to form CH_4 during the first half-cycle in our system at 125°C. This number agrees well with literature reports, which typically give values of 1.5-1.7.[79,88,214]

Pressure

The pressure in the ALD chamber of ~0.31 Torr is a result of the pumping speed and the N_2 carrier flowrate (20 sccm) only between precursor pulses. The pressure read by the thermocouple gauge shows pressure pulses above this N_2 baseline with the additional vapor pressure of each TMA and H_2O pulse, as shown in **Figure 5.5** (upper panel) for a typical train of 10 TMA and 10 H_2O pulses. The average maximum pressure increase above baseline during TMA pulses is 0.049 ± 0.014 Torr and during H_2O pulses is 0.036 ± 0.004 Torr. The small apparent shift in baseline pressure after several TMA pulses is due to reproducible and reversible offset in the thermocouple gauge that is sensitive to chemical environment. The average integrated precursor pulse for open valve experiments was ~7 times larger than closed valve experiments.

Calorimetric Heats of Adsorption

A raw voltage signal measured by the calorimeter simultaneously with this pressure measurement is shown in **Figure 5.5** (lower panel). The first heat signal in each 10-pulse half-cycle is much more intense than subsequent signals, due to near saturation of surface sites during the first pulse of each half-cycle (see QCM, **Figure 5.4**). The average heat signal during the first, second, third, as well as seven "saturation" TMA pulses (all averaged over five complete ALD cycles) are overlaid and shown over a 300x smaller time window in **Figure 5.6**. The signal upon the first TMA pulse has a rise time of ~7 ms and is dramatically more intense than subsequent pulses. The second pulse's signal has an initial sharp feature which is similar in shape and rise time to the first, but only ~5% as intense. The sharp feature is followed by a broad, low-intensity feature that has a maximum ~150 ms after the precursor pulse. By the third pulse, this broad peak is the dominant feature, although there remains a small initial peak that is only ~1% as intense as the first peak maximum. After the third dose, the only signal measured is the broad peak. The signals for the final seven pulses (doses 4 to 10) do not vary significantly, so the subsequent pulses were averaged together over each of the five cycles (35 pulses total). This signal is referred to as the "saturation" signal. The QCM data shows that ~63% of the mass gain during the TMA half-reaction occurs in the first pulse, and ~11% in the second pulse. Though the calorimeter's sharp heat signal has decreased to near zero after the third TMA dose, the QCM data suggests there is still a slow increase in deposited mass until saturation occurs by the eighth pulse. As shown below using a simple bond-additivity model, this nonlinear relationship between heats and mass gain is due to preferential reaction of TMA to form adsorbed MMA ($x = 2$) at low coverage, which has a much higher heat than the reaction to form adsorbed DMA ($x = 1$). The later reaction, which requires only one –OH group, dominates at high coverage due to lack of reaction sites for TMA that offer

two unreacted –OH groups needed to make MMA. When integrated from zero coverage up to saturation, the average *x* value is 1.7, consistent with the QCM data. This non-linearity in the relationship between heat and mass gain results in part from the fact that the mass gain per Al is 40% larger when $x = 1$ than when $x = 2$ due to the extra CH_3 that remains on the surface.

Figure 5.7 shows the second half-reaction (Reaction B), wherein H_2O is pulsed to the methylated surface and acts as the O source, releasing more CH_4 and regenerating a hydroxyl-terminated surface. Similar to the TMA half-reaction, the first pulse is by far the most intense. The peak maximum is only 0.45 mV using the same amplification—approximately 29% as intense as the first dose of TMA. The shape of the first H_2O pulse is very similar to that of the first TMA pulse. The second pulse also has a sharp initial feature which gives way to a broad, low-intensity secondary peak. Unlike the TMA series, even at saturation, there remains a sharp initial feature that is ~25% as intense as the first dose. The QCM measurements suggest that saturation is achieved after the first pulse of H_2O, even as the calorimeter signal shows a steady decay in the sharp peak intensity, with saturation achieved after the third pulse.

As seen in **Figure 5.8**, during TMA pulsing, the cumulative heat grows rapidly with mass gain initially, but then, after ~2/3 of the saturation mass gain, it grows much more slowly, and almost stops growing completely as saturation mass gain is approached. The same occurs but to a less dramatic extent during H_2O pulsing. It is commonly observed that both molecular and dissociative adsorption reactions become less and less exothermic as the surface coverage grows toward saturation due to both preferential titration of the most stable surface sites and adsorbate-adsorbate repulsions which increase as the adsorbates pack closer together, and similar effects occur here (see below). At saturation mass gain, the cumulative heats during the TMA and H_2O half-reactions saturate at 413 and 181 kJ/mol, respectively. The sum of these heats is 594 kJ/mol,

consistent with the literature value for the standard-state reaction enthalpy for this NET Reaction to produce amorphous Al_2O_3 (which we grow here[231]) and CH_4. This NET Reaction enthalpy is -594 kJ per mol Al, as calculated using tables of standard heats of formation[232] and the knowledge that amorphous Al_2O_3 is 38.4 kJ/mol less stable than corundum (α-Al_2O_3),[233] which has a standard heat of formation of -1675.7 kJ/mol.[232] (We actually added a small correction factor to the heat-signal calibration sensitivity measured using light-pulses in order to get this perfect agreement at 594 kJ/mol, for the reason described previously.[189])

The ratio of cumulative heats at saturation for the TMA to H_2O half-reactions from **Figure 5.8** is (413 kJ/mol) / (181 kJ/mol) = 2.28, consistent with several DFT calculations that predicted the TMA reaction to be more exothermic than the subsequent H_2O reaction.[217,222,223]

We attribute the broad, secondary heat signal to heating of the sample as precursors (and products from reaction upstream) with different thermal conductivities than the N_2 carrier gas pass the sample surface, and show evidence to support this assignment below, including correlation of this peak's time with the arrival time of the precursor's pressure pulse. This behavior is reminiscent of *in situ* ALD mass spectrometry data in which the reaction product is fast relative to the precursor dose.[234] The sharp, fast heat pulse at saturation during the H_2O half-cycle is may be due to weak, physical adsorption of the precursor onto the fully-saturated surface, which slowly desorbs again before the next pulse arrives.

We also performed experiments with the manual valves left open to simulate conventional ALD tool "open-valve" operation. The pressure pulses after saturation were approximately 6-fold larger than in the closed-valve experiments above, indicating that the doses were approximately 6-fold larger. The changes in the heat signals due to this were as expected for the larger dose. The peak maximum of the first open-valve TMA pulse was ~38% more intense than the closed-valve

peak. The broad signal after saturation due to less gas cooling was ~2-fold larger. We focus primarily on the closed-valve results presented from **Figure 5.3** to **5.8** above (and analyzed in detail from **Figure 5.12** to **5.14** below), as they represent a more incremental approach to saturation and better reproducibility.

In the limit of saturating precursor doses, no further heat of surface reaction is anticipated. As previously noted a heat of physisorption is possible, although this value is expected to be exceedingly small. Since pyroelectric materials are also piezoelectric, a voltage may be generated by a pressure differential across the crystal. The change in gas composition and flow upon dosing may also cool or heat the crystal. To investigate these effects, we introduced pulses of N_2 gas—which will not adsorb to the sample surface—in a similar manner to the pulses of TMA and H_2O. The average maximum pressure differential during these N_2 pulses was 0.73 Torr, approximately 18 times higher than the differential pressures measured during the ALD precursor pulses. In spite of this 18-fold larger dose size, the N_2 pulses produce a heat signal that is only ~14% of that for the first TMA pulse, but of similar lineshape on every pulse. Correcting this for the pressure ratio (dose ratio), the heat signal for N_2 is only ~0.8% of that for TMA. This proves that there no significant contribution to the heat signal due to the heating or cooling of the sample simply by collisions with pulsed gas that is possibly at slightly different temperature than the sample. However, we pulsed here the same gas as the carrier gas (N_2), so the gas's thermal conductivity (which is independent of pressure) is not affected. We show below that when a gas with a different thermal conductivity than N_2 is pulsed, it transiently affects the sample temperature, resulting in a slow and broad heat signal which is also present after saturation.

To investigate the effect of temperature we performed similar experiments at 130°C to those shown above at 125°C, as shown in **Figure 5.9**. This comparison was done in the open-valve

approach. In the first TMA pulse at 125°C, there is a shoulder on the main heat signal peak that occurs ~24 ms after the main peak. This shoulder shifts to ~14 ms at 130°C. We attribute this shoulder to slower kinetics of the irreversible adsorption of TMA (i.e., Reaction A), which gets slower as it approaches saturation due to the lower availability of free surface sites or –OH groups for reaction. At higher temperatures, the TMA reacts faster, shifting this shoulder peak to shorter times (and making it higher). The integrated areas of this shoulder is very similar at 125 and 130°C, indicating that this small temperature difference is not enough to reduce the amount of TMA that reacts, but is enough to modify the time constant of reaction. The kinetic half-lives ($t_{1/2}$) for this shoulder at 125°C to 130°C are ~24 ms and ~14 ms, respectively (see above), corresponding to first-order rate constants (i.e., $k = \ln(2)/t_{1/2}$) of 0.034 s^{-1} and 0.021 s^{-1}, respectively. Arrhenius analysis of these rate constants gives an apparent activation energy of ~136 kJ/mol and a prefactor of 10^{19} s^{-1}. These are very rough estimates since this uses only two points that are very close in temperature. They correspond to the rate constant for some activated elementary step that is part of the net Reaction A which gets slow at high coverage. This value of 136 kJ/mol can be compared to the sublimation enthalpy of bulk TMA(solid), 60 kJ/mol.[232]

GROWTH OF OTHER OXIDE FILMS BY ALD

Titanium dioxide is one of the most well-studied metal oxides in surface science,[235,236] and a material of great interest to the fields of photocatalysis[237,238] and solar cells.[239,240] We studied its formation by ALD using repeated cycles of 10 pulses of $Ti(NMe_2)_4$ (TDMAT), where Me = CH_3, followed by 10 pulses of H_2O, as reported previously *via* the overall reaction[241]

$$Ti(NMe_2)_4 + 2\ H_2O \rightarrow TiO_2(solid) + 4\ HNMe_2 \qquad (D)$$

TiO_2 growth on a titania-precoated surface during one representative closed-valve, 20-pulse cycle of TDMAT–H_2O, along with average QCM readings on both inlet and outlet QCMs, are shown in **Figure 5.10**. The QCM measurements reveal that the growth rate is mole-limited since no substantial mass gain was recorded on the outlet QCM until the fourth pulse. Integrated areas of the TDMAT heat signals also shows that the *third* TDMAT pulse has the largest heat, despite the first heat signal having the largest peak intensity (not shown). The QCM mass gains also indicate that water dosing causes mass loss, a characteristic response which has been seen during an analogous reaction to form TiN using alternating TDMAT and NH_3 pulses.[242] Using the ratio of mass gains from either QCM and an analysis similar to Equation 5.1 above, we estimate that 72% of the NMe_2 ligands are reacted during the first half-reaction at 120°C.

Lastly, we investigated thin film growth of manganese oxide, a material of interest for catalysis[243,244] and battery technologies,[245,246] using repeated open-valve cycles of 12 pulses of $Mn(EtCp)_2$, where Et = C_2H_5, and Cp = cyclopentadienyl (see **Table 5.1** for structure), followed by 12 pulses of H_2O, as reported previously *via* the overall reaction[247]

$$Mn(EtCp)_2 + H_2O \rightarrow MnO(solid) + 2\ HEtCp \qquad (E)$$

MnO growth on a MnO-precoated surface during one representative open-valve, 24-pulse cycle of $Mn(EtCp)_2$–H_2O, along with the average QCM reading on the inlet QCM, are shown in **Figure 5.11**. Burton et al.[247] reported that 54% of the $Mn(EtCp)_2$ molecules lose one EtCp group in the first half-reaction at 150°C, with the remaining 46% of molecules losing both EtCp groups in the first half-reaction. Our QCM measurements show a mass gain after the $Mn(EtCp)_2$ half-reaction

of 96 ng/cm^2 and an overall mass gain of 92 ng/cm^2, indicating a loss of mass in the water dosing step, which is consistent with the literature.[247] Approximately 88% of the ECPDM molecules lose both EtCp ligands after the first half-reaction at 120°C.

DISCUSSION

Analysis of Calorimetric Heats

To a very good approximation, the instantaneous voltage measured by the calorimeter is directly proportional to the instantaneous heat power being added to or removed from the surface, as was shown in **Figure 5.3**. Thus, the absolute heat released on the crystal surface coincident with an ALD precursor dose may be derived by time-integrating the heat-signal voltage versus time plots, such as those shown in **Figure 5.6** and **5.7**. This is only complicated in a very small way by the cooling (negative-going) signal that must accompany the return to equilibrium temperature but is exceedingly small on this scale and decays exponentially due to the 25 s time constant (see discussion after **Figure 5.3** above). Thus, integration should be limited to 5% of this time constant (1.25 seconds). For the signals in **Figure 5.6** and **5.7**, a 0.5 s integration provides a good compromise that gets almost all of the positive-going signal, but may prove too short for other ALD reactions, depending on the kinetics of heat-deposition reactions.

Figure 5.12 shows the results of such integration versus pulse number. There is a large net reaction heat per pulse even after saturation for both TMA and H_2O pulses. We attribute the heat seen after saturation to the changing thermal conductivity of the gas: when a gas like TMA or H_2O with a lower thermal conductivity than N_2 is pulsed, it transiently affects the sample temperature, due to less efficient cooling of the sample by the flowing gas. (At steady-state, the sample is intermediate in temperature between the cooler vacuum chamber walls above it and the warmer

sample holder and heater below it.) This results in a slow and broad heat signal which is also present after saturation. Re-cooling should give rise to a negative-going signal, but that seems to be stretched out over such a long time (up to 10 s) compared to the heating time (0.1 – 0.2 s) that the signal is not obvious in **Figure 5.6** and **5.7**.

We must subtract the heat signal due to this change in thermal conductivity from the net heat due to all reactions in order to get the heat associated with only the irreversible processes that give rise to ALD film growth. For H_2O pulses, this is simple, since the signal that remains after saturation appears to be the same with every pulse (within statistical scatter). So here, we subtracted the integrated heat signal averaged for the pulses *after* saturation from that at earlier pulses. The resulting difference due to irreversibly adsorbed/reacted H_2O is also shown in **Figure 5.12**.

The situation is more complicated with TMA, where it appears that the amount of signal in the slow, broad peak due to the change in thermal conductivity is not constant but instead increases to a saturation level with pulse number. Detailed inspection of the heat signal lineshape in **Figure 5.6** shows that this heat is associated with a peak maximum that occurred ~100 ms after the pulse onset, noticeably slower than the large heat maximum seen in the first pulse. Importantly that fast maximum is also seen in the second pulse but not in later pulses. We attribute it to the heat of the irreversible processes that give rise to ALD growth, and the slower peak at ~100 ms later to the change in thermal conductivity of the gas above the surface as TMA passes the surface. One can see that this slower peak grows in amplitude with pulse number from nearly zero on pulse 1 to a saturation level. This is due to the increase in the amount of TMA that reaches the surface with each pulse in the first few pulses (due to extensive reaction of TMA with chamber walls and other hot surfaces, especially in the first pulse). We estimated its size for pulse 2 by subtracting

the integral of the fast first peak from the total integral. The resulting integral of this slow peak's heat (due to thermal conductivity changes) is shown versus pulse number in **Figure 5.12**. We extrapolated those points back to pulse 1 to estimate the amount of heat due to thermal conductivity change in that first pulse, which is very close to zero, as shown. **Figure 5.13** shows the cumulative integrated heat signals pertaining to irreversible adsorption to highlight the quick approach toward saturation.

Figure 5.14 offers further support for our conclusion that the heat signal which maximizes at ~100 ms after the pulse onset is due to the change in thermal conductivity. It compares the first, second, and saturation TMA heat signals of **Figure 5.6** to the gas pressure in the same time frame. At saturation, the gas pressure after a TMA pulse rises most rapidly just when the heat we attribute to thermal conductivity changes maximizes. In future experiments we will try to minimize this unwanted heat signal by increasing the temperature of the top (cooler) parts of the chamber. We show here that reasonable heats for the irreversible ALD reactions can be obtained even in its presence, due to the separation in time scales.

Summing the areas corresponding to irreversible adsorption, as shown in **Figure 5.12** and **5.13**, gives the total integrated heat signal corresponding to a saturated monolayer of each half-cycle: 27.8 ± 0.4 μVs for TMA and 11.7 ± 0.2 μVs for H_2O. Dividing these sums by the sensitivity factor from **Figure 5.3** (0.1092 ± 0.0015 Vs/J) gives the total reaction heat absorbed by the detector in each half-cycle: 2.54 ± 0.03 x 10^{-4} J for TMA and 1.07 ± 0.01 x 10^{-4} J for H_2O. The QCM data and the area of the detector can be used to convert these values into units of kJ per mol of reaction. The detector area is 0.59 cm^2 and the TMA half-cycle added 35.3 ± 1.4 ng/cm^2 to the surface, resulting in 20.8 ± 0.8 ng deposited on the detector. The H_2O half-cycle added 4.7 ± 1.0 ng/cm^2, resulting in 2.8 ± 0.6 ng added to the detector surface. Given the combination of the molecules

added to and subtracted from the surface during this reaction (with x = 1.7), we determine the average molar mass of the material added during each half-reaction to be 44.8 g/mol and 6.2 g/mol for Reactions A and B, respectively. Dividing the mass gained by the molar masses gives 4.64 ± 0.19 x 10^{-10} moles of Reaction A during the TMA half-cycle and 4.47 ± 0.95 x 10^{-10} moles of Reaction B during the H_2O half-cycle. Dividing the total heats by the moles of reaction gives the enthalpy of reaction for each half-cycle: -548 ± 30 kJ/mol for the TMA half-cycle and -240 ± 54 kJ/mol for the H_2O half-cycle, where "per mole" here refers to "per mole as written" in reactions A and B above, respectively (i.e., per 1 mole of TMA but per 1.5 moles of water). The ratio of the two half-reactions is 2.28. The heat for the full TMA–H_2O ALD cycle:

$$\mathrm{Al(CH_3)_3}(g) + \tfrac{3}{2}\,\mathrm{H_2O}(g) \rightarrow \tfrac{1}{2}\,\mathrm{Al_2O_3}(s) + 3\ \mathrm{CH_4}(g) \qquad \text{(NET)}$$

i.e., the sum of the two half-reaction heats, is -788 ± 84 kJ/mol.

The heat of this NET Reaction to produce corundum (α-Al_2O_3) as calculated from the NIST tables of standard heats of formation is -613.2 kJ per mol Al.[232] However, the TMA–H_2O ALD reaction is known to produce amorphous Al_2O_3,[231] which is 38.4 kJ/mol less stable than α-Al_2O_3,[233] reducing the heat of this NET Reaction to -594 kJ per mol Al. The difference between this value and our calibrated heat (-788 kJ/mol) is associated with imperfect absolute calibration of the detector sensitivity. A better calibration method for the heat detector than using a flashlight as above is to use the net heat of a known reaction like this one to calibrate it. The theoretical sensitivity to produce an overall reaction heat of -594 kJ/mol is 0.145 Vs/J; thus, the sensitivity factor determined using our light calibration method is 24.7% low. Given the inaccuracies inherent in calibration with such a white-light source (see above), this level of disagreement is expected.

We have used this internal calibration below to examine the accuracy of the relative heats during each half-cycle. This new calibration yields calorimetric heats of -413 kJ/mol for the TMA half-cycle and -181 kJ/mol for the H_2O half-cycle to produce amorphous Al_2O_3. (The hypothetical TMA and H_2O half-reaction heats to produce α-Al_2O_3 are -426 and -187 kJ/mol, respectively.)

Simulating the Heats with a Simple Bond Additivity Model

We show next that the experimental results of **Figure 5.8** can be nearly quantitatively simulated with a simple bond additivity model. This model will be based on forming crystalline α-Al_2O_3 rather than the much more complicated amorphous Al_2O_3 that is actually grown here. However, the heat of the above NET Reaction to make α-Al_2O_3 is 613.2 kJ per mol Al from standard heats of formation,[232] while the heat to make amorphous Al_2O_3 is 594.0 kJ/mol (see above). Therefore, we will scale the heats from this bond-additivity model by the ratio 594.0 / 613.2 = 0.969 to more closely model the real experiment.

We first estimate the average bond enthalpies of all the bonds formed/broken during the NET Reaction using standard heats of formation. For example, each Al atom in α-Al_2O_3 is bonded to six oxygen atoms. Therefore, the enthalpy of dissociating α-Al_2O_3 into 2 Al(g) + 3 O(g) (+3083 kJ/mol) corresponds to breaking 12 Al–O bonds, giving +256.9 kJ/mol for its average Al–O bond enthalpy. All the average bond enthalpies we used in this model are compiled in **Table 5.3** along with the net reaction used to estimate it and its standard enthalpy (at 298 K).

Reactions A and B are written above in the usual way for discussing ALD of Al_2O_3, which focuses on the bonds between Al atoms of TMA and the oxygen atoms from surface –OH groups. However, these expressions leave out any details about bonds that may form when the TMA adsorbs between its Al atom and coordinatively-unsaturated surface oxygen atoms of the growing

alumina lattice (O_l, see below) that were not in surface –OH groups. We found that it is necessary to include those bonds in order to accurately reproduce the experimental heats in **Figure 5.8** with our simulation. Thus, we rewrite Reactions A and B below in the following, more precisely-defined way that now specifically includes the surface lattice oxygens (O_l):

$$Al–(CH_3)_3 \; + \; x \; {*O_h}–H \; + \; y \; {*O_l} \; \rightarrow \; {*(O_h)_x(O_l)_y}–Al(CH_3)_{3-x} \; + \; x \; H–CH_3 \qquad (A_y)$$

$${*(O_h)_x(O_l)_y}Al–(CH_3)_{3-x} \; + \; 1.5 \; H–OH \; + \; (4.5-x-y) \; {*O_l} \; \rightarrow \; {*(O_h)_x(O_l)_{6-2x}}Al–(OH)_{1.5}(O_lH)_{x-1.5} \; + \; (3-x) \; H–CH_3 \qquad (B_y)$$

$$Al–(CH_3)_3 + x \; {*O_h}–H + (4.5-x) \; {*O_l} + 1.5 \; H–OH \; \rightarrow \; {*(O_h)_x(O_l)_{6-2x}}–Al–(OH)_{1.5}(O_lH)_{x-1.5} + 3 \; H–CH_3 \qquad (NET_y)$$

The new stoichiometric coefficient *y* is the number of Al-O bonds to surface lattice oxygens that form in the adsorbed intermediate (MMA when $x = 2$, or DMA when $x = 1$). There are two types of surface oxygen species initially, designated by the subscripts *h* for "hydroxyl" and *l* for "lattice," which remain on those oxygens as they convert to other species to keep track of their origins. Oxygen atoms introduced later from H_2O vapor in Reaction B_y are not designated with any subscript. Asterisks indicate species that are part of the alumina surface. Dashes indicate the bonds that are formed/broken in each step.

All integer combinations of $x = 1$ or 2 and $y = 1$, 2 or 3 might be possible for an individual TMA molecule that reacts with the surface, so none can be excluded. As noted above, the QCM measurements show that $x = 1.7$ on average. Using the average bond enthalpies in **Table 5.3**, we can reproduce the observed ratio of saturation heats for Reaction A to B of 2.28 using this average

x value of 1.7 only when we use $y = 2$. Having $x = 1.7$ and $y = 2$ means that the product of Reaction A (i.e., TMA dosing) is $*(O_h)_{1.7}(O_l)_2Al(CH_3)_{1.3}$ on average. Note that this corresponds to a total of 5 bonds to the Al atom, intermediate between 3 in the reactant TMA and 6 in the final Al_2O_3 product. While these average values explain the ratio of saturation heats, they do not explain the very non-linear dependence of heat on the mass gain during TMA dosing (**Figure 5.8**). To understand that, we must consider how the integer values of x and y for specific TMA molecules varies as the reaction proceeds.

As seen in Reaction A_y, each integer addition of 1 to x requires another surface –OH group (written as $*O_h$–H above), and each integer addition of 1 to y requires another coordinatively unsaturated O_l. Since these –OH and O_l groups are being consumed as the reaction proceeds, it is thus likely that both x and y decrease rather markedly as saturation is approached.

Thus, it is likely that the high heat in early pulses is due to reaction to form MMA on the surface ($x = 2$), which requires two surface –OH groups nearby, and only after such "dual –OH" sites are titrated does TMA react to form DMA ($x = 1$), which requires only one –OH. That is, $x = 1.7$ on average, but $x = 2$ in early pulses and $x = 1$ in later pulses. To reproduce the average experimental x value of 1.7 based on the QCM, we must assume that TMA reacts to form MMA on the surface ($x = 2$) over the first 70% of the total number of TMAs that react.

With this in mind, we simply searched for the y values that give the best fit to the data in **Figure 5.8**. We found that the best fit was achieved when $y = 3$ for the first 50% of the $x = 2$ range (first 35% of the total mass-gain range), and then drops to $y = 2$ for the last 50% (35→70% of the total range). Similarly, $y = 1$ in the first 83% of the $x = 1$ range (70→95% of the total range), and drops to $y = 0$ for the last 17% (95→100% of the total range).

Thus, up to point A in **Figure 5.8**, the TMA half-reaction proceeds to form MMA ($x = 2$) and three Al–O_l bonds ($y = 3$) *via* the reaction

$$Al–(CH_3)_3 \; + \; 2 \; {}^*O_h–H \; + \; 3 \; {}^*O_l \; \rightarrow \; {}^*(O_h)_2(O_l)_3–Al(CH_3) \; + \; 2 \; H–CH_3$$

This reaction deposits 11.0 ng/cm^2 with a reaction enthalpy of -645 kJ/mol, and is responsible for 35% of the total TMA reaction (cumulative integrated heat = 0.35 x 645 = 226 kJ/mol). The next 35% (from point A to B) is due to TMA molecules forming MMA ($x = 2$) and two Al–O_l bonds ($y = 2$):

$$Al–(CH_3)_3 \; + \; 2 \; {}^*O_h–H \; + \; 2 \; {}^*O_l \; \rightarrow \; {}^*(O_h)_2(O_l)_2–Al(CH_3) \; + \; 2 \; H–CH_3$$

This reaction thus deposits another 11.0 ng/cm^2 but with a less exothermic reaction enthalpy of -396 kJ/mol (cumulative integrated heat after 70% of the total TMA has reacted = 364 kJ/mol).

From 70% to 95% of the total TMA reacted (point B to C), incoming TMA molecules react to form DMA on the remaining surface ($x = 1$) while making only 1 Al–O_l bond ($y = 1$):

$$Al–(CH_3)_3 \; + \; {}^*O_h–H \; + \; {}^*O_l \; \rightarrow \; {}^*(O_h)(O_l)–Al(CH_3)_2 \; + \; H–CH_3$$

Since only one CH_4 now leaves the surface (as opposed to two when making MMA in the last two reactions above), the mass gain per reacted TMA is larger. This reaction thus deposits another 11.0 ng/cm^2 but again with a less exothermic reaction enthalpy of -198 kJ/mol (cumulative integrated

heat = 414 kJ/mol). Finally, from 95% to the saturated surface (point C to D), TMA reacts to form DMA on the surface ($x = 1$) but there are no remaining O_l with which to bond ($y = 0$):

$$Al–(CH_3)_3 \; + \; {*}O_h–H \; \rightarrow \; {*}(O_h)–Al(CH_3)_2 \; + \; H–CH_3$$

This reaction deposits a final ~2.2 ng/cm^2 and is nearly thermoneutral (reaction enthalpy of +50.9 kJ/mol, total cumulative integrated heat = 411 kJ/mol). Since the gaseous methane product is pumped away, this reaction can proceed to completion even if slightly endothermic.

As seen in **Figure 5.8**, this model fits the data exceptionally well and explains the extreme non-linearity in a very logical way where x and y decrease with coverage just as expected based on physical intuition.

In the case of H_2O dosing (see the inset of **Figure 5.8**), there is much less obvious non-linear trend in heat versus QCM mass gain, so we have not attempted to model that explicitly. The straight line shown from the origin to saturation fits the data well enough. This straight line would be expected if the H_2O molecules do not preferentially react with any of the surface species pre-deposited by TMA (e.g., DMA vs. MMA). This is somewhat surprising since the heat for the H_2O half-reaction depends as strongly on x and y as does the TMA half-reaction, and thus its rate constant does not depend on the exothermicity of the particular x,y value for the TMA-derived intermediate it attacks. This would happen, however, if the reaction probability of the initial attack of every Al-CH_3 group by H_2O is independent of the way in which that Al atom is bonded to the rest of the surface. This seems most likely if this is a very high reaction probability per H_2O—Al-CH_3 collision due to an almost barrier-less process.

State-of-the-art DFT could probably give better accuracy than this simple bond additivity model. It is expected that these new calorimetrically-measured energies for Reactions A and B will be used together with future DFT calculations to more clearly define the surface intermediates involved in Reactions A_y and B_y above.

The heats of adsorption of the TMA and H_2O half-reactions on Al_2O_3 calculated from first principles vary widely in the literature, and some relevant results are summarized in **Table 5.4**. Widjaja and Musgrave[217] used cluster DFT to calculate the adsorption and reaction energy of the TMA and H_2O half-reactions. On an $Al[OAl(OH)_2]_2$-OH cluster, TMA adsorbed to the surface with an energy of -59 kJ/mol and reacted to form DMA and CH_4 with an energy of -105 kJ/mol (overall energy = -164 kJ/mol). The authors did not present the energy released to react another methyl with an adjacent hydroxyl and make MMA, but it may be crudely estimated by adding another -105 kJ/mol to the overall energy (-269 kJ/mol). Adsorption of H_2O on both DMA and MMA surfaces gave overall heats of -143 and -125 kJ/mol, respectively. By linear interpolation we have estimated the ratio of reaction heats for our extent of reaction of x = 1.7 to be 1.82, reasonably close to our experimental value of 2.28.

Elliott and Greer[218] used periodic DFT to calculate the adsorption energy of TMA onto a fully hydroxylated α-Al_2O_3 surface, reporting values of -68, -164, and -174 kJ/mol for the formation of adsorbed TMA, DMA, and MMA, respectively. On a bare α-Al_2O_3 surface, the authors found that TMA adsorbed with a heat of -116 kJ/mol, but this was followed by dissociation of TMA into three Al–CH_3 surface species. These scenarios do not accurately represent our experimental surface, but dissociation reactions may occur locally in regions of the surface where no other reaction pathways are available.[79]

Recently, Weckman and Laasonen[222] investigated TMA and H_2O adsorption on the α-Al_2O_3 surface using periodic DFT with a surface hydroxyl concentration (9.6 OH/nm^2) that agrees well with experimental coverages (~9 OH/nm^2 under typical conditions[79]). The authors calculated the adsorption energy and reaction heat of the first TMA molecule to DMA to be -177 kJ/mol. Further reaction to MMA gave an overall reaction heat of -310 kJ/mol. The heat of adsorption and reaction of H_2O with surface-bound DMA and MMA gave calculated heats of -257 and -122 kJ/mol, respectively. By linear interpolation, we have estimated the ratio of reaction heats for our extent of reaction of x = 1.7 to be 1.66. While the authors did investigate the adsorption of multiple TMA molecules in order to approximate a methylated surface, they did not investigate the adsorption of H_2O with the methylated surface.

Finally, Sandupatla *et al.*[223] used periodic DFT to calculate the adsorption and reaction heats of the TMA and H_2O half-reactions on a γ-Al_2O_3 surface with a surface hydroxyl concentration of 8.8 OH/nm^2. The first TMA adsorption and reaction to DMA had a heat of -264 kJ/mol and subsequent reaction to MMA added an additional heat of -77 kJ/mol. Thus, the corresponding DFT heat for our experimental extent of reaction of x = 1.7 is -318 kJ/mol. Continuing along the path to produce a fully methylated surface gives a total DFT heat of -1263 kJ/mol or -316 kJ per mol Al. This heat is ~77% of our experimental heat for the TMA half-reaction (with the signal calibration based on the heat of the total reaction determined using heats of formation). The authors did not calculate the reaction of H_2O with the fully methylated surface; however, they did present reaction heats of H_2O with single molecules of adsorbed TMA (-120 kJ/mol), DMA (-207 kJ/mol), and MMA (-74 kJ/mol). Since there is likely a very small percentage of adsorbed (yet unreacted) TMA to interact with H_2O in our system, we have ignored the reaction heat with TMA. By linear interpolation, and using our experimental extent of reaction of x = 1.7,

we estimate the reaction heat in the second half-cycle based on these DFT energies to be -114 kJ/mol. The corresponding ratio of DFT energies for the two single-molecule half-cycle reactions is 2.79, which is again in reasonable agreement with our experiments.

To our knowledge, the only prior experimental study of the heats evolved during ALD half-reactions was performed by Nilsen and Fjellvåg using a thermopile.[225] In that work, the authors note that introduction of room temperature precursors into the reaction chamber at 186°C had a very large effect on the observed heats. As such, they were unable to derive a conversion factor from the thermopile voltage reading into heats of adsorption. Additionally, inconsistencies in their data call their conclusions into question. However, the authors did observe a sharp initial feature when dosing H_2O in the absence of TMA, as we have seen in our "saturation" signals shown in **Figure 7**. Comparing to their estimated sensitivity, our calorimeter is ~800 times more sensitive.

General Discussion and Future Work

In addition to the thermodynamic insights that absolute heats of each half-reaction provide, the *in-situ* ALD calorimeter may provide additional insight into ALD reaction dynamics. Due to the intrinsically fast response time of the detector and electronics, ALD reaction kinetics may be resolved with unprecedented precision. The response time of the experiment depends on the heat transfer rate from the growing film's surface to the detector as well as the amplifier circuitry. In practice, we observe a rise time in the calibration experiment with photon heating that is equivalent to the shutter open time (~1 ms), so the response time is faster than that. In our *in-situ* ALD experiments, we recorded a data point every 0.5 ms, which is already two orders of magnitude faster than the time resolution utilized to get good signal-to-noise for other *in-situ* probes such as QCM (100 ms) and quadrupole mass spectrometry (50 ms).

In interpreting the heats measured here, we have assumed above that the reaction products are thermalized to the surface temperature. However, when methane molecules are produced at surfaces from the addition of H to methyl groups, as occurs here, they have been shown in at least one case to exit the surface with excess enthalpy (above that expected for a Boltzmann distribution at the surface temperature).[248] However, since the gas pressure in this ALD system is ~0.3 Torr, the inelastic mean free path of gas molecules is only ~10^{-2} cm, or ~1% of the diameter of the exposed detector. Thus, if the gaseous products of the ALD reactions are generated with excess enthalpy relative to the surface temperature, the gas just above the detector surface would rapidly thermalize the energy and transfer it back to the surface through collisions. Therefore, it seems safe to assume that the reaction products are thermalized to the surface temperature in such ALD measurements at 0.3 Torr total pressure and above.

This ALD calorimetry approach might also be applied to study ALD processes on powders which can be drop-cast and dried directly onto the detector. We performed preliminary ALD calorimetry experiments of indium oxide film growth using pulses of trimethylindium and H_2O onto a powder film of the metal-organic framework (MOF) NU-1000[92,158] which had been drop-cast onto the detector surface from acetone solvent and dried in vacuum. This produced strongly exothermic heat signals, as expected when increasing the surface area for adsorption by multiple orders of magnitude (even if the MOF powder is in imperfect thermal contact with the detector surface). Since the nodes in many MOFs are oxide clusters of controllable sizes near ~1 nm in diameter, they can be thought of as very well-defined and homogeneous oxide "nano-supports" to which catalytic metals can be attached to improve activity or simply to provide a more homogeneous structure to facilitate fundamental studies of oxide-supported metal clusters. Thus, further investigations of ALD in MOFs (and other porous materials) would be highly impactful.[85-

[87,249-251] With proper calibration, this calorimeter may produce benchmark energies to compare with computational results for high surface area substrates as well.

Looking forward, further improvements to the ALD calorimeter can be made. One improvement may be faster dosing so that smaller and more reproducible doses could be made to understand partial saturation reactions. This could be achieved by cooling the precursor sources to lower the vapor pressure in the headspace, or by installing a second actuated valve in place of the manual valve so that the "closed valve" experiments can be precisely timed by the computer (and smaller doses dictated by the flowrate of the gas into the headspace). In addition, a faster sampling rate in pressure detection/recording would help to measure these doses more accurately and precisely. As noted above, using a single-wavelength light source, such as a stabilized HeNe laser, and an integrating sphere to accurately determine the sample reflectivity at various thicknesses of oxide deposition would provide a more accurate calibration of the detector. Stabilizing the ALD chamber temperature and introducing precursor gases that are at exactly this same temperature, perhaps with a longer pre-heat region would further simplify data analysis. Finally, the use of a second pyroelectric detector crystal as a 'reference signal', pressed into the back of the first crystal with the polarization reversed, has been shown to be effective at reducing contributions to the signal from noise in the chamber due to thermal fluctuations and mechanical vibrations.[252]

Measurements of the calorimeter signal during TMA–H_2O ALD at different temperatures up to the limit of the detector (the Curie temperature of $LiTaO_3 \approx 600°C$[253]) would be valuable. Since the TMA–H_2O ALD mechanism depends strongly on surface hydroxyl content,[79,218] which in turn depends on temperature, we could feasibly probe systems where $x = 1$ and $x = 2$ to confirm the effect on the reaction heats of the extent of reaction that occurs in the TMA half-reaction.

Simultaneous transient quadrupole mass spectrometry analysis would provide additional support for these experiments which are underway in our laboratories.

CONCLUSIONS

We presented a new calorimeter that approaches the ideal limit of a heat detector whereby the signal at any time is proportional to the heat power being delivered to the sample, and was proven to be sensitive to measuring heats of adsorption for three distinct sub-monolayer ALD half-reactions. Focusing on the oft-studied TMA–H_2O reaction to form Al_2O_3, we measured the heats of the TMA and H_2O half-reactions to be -413 and -181 kJ per mol of Al, respectively. Simultaneous QCM measurements showed an overall mass gain of 40.0 ng/cm^2 with 35.3 ng/cm^2 gained during the TMA half-reaction, indicating that 1.7 CH_3 groups per TMA react to form CH_4 during the TMA half-cycle. We show below that these results and the cumulative heat of reaction versus extent of reaction can be quantitatively reproduced with a simple bond-additivity model based on tabulated heats of formation, which reveals important details of how the nature of the adsorbed intermediates being produced varies with the extent of reaction during the TMA half cycle. The broad applicability of this calorimetry method was further demonstrated by studying the heats of ALD reactions to produce TiO_2 and MnO_x. In-depth analysis of other ALD reactions would be impactful in clarifying the reaction intermediates and elementary-step energetics, and as energy benchmarks for theory, like shown above for TMA–H_2O to grow Al_2O_3.

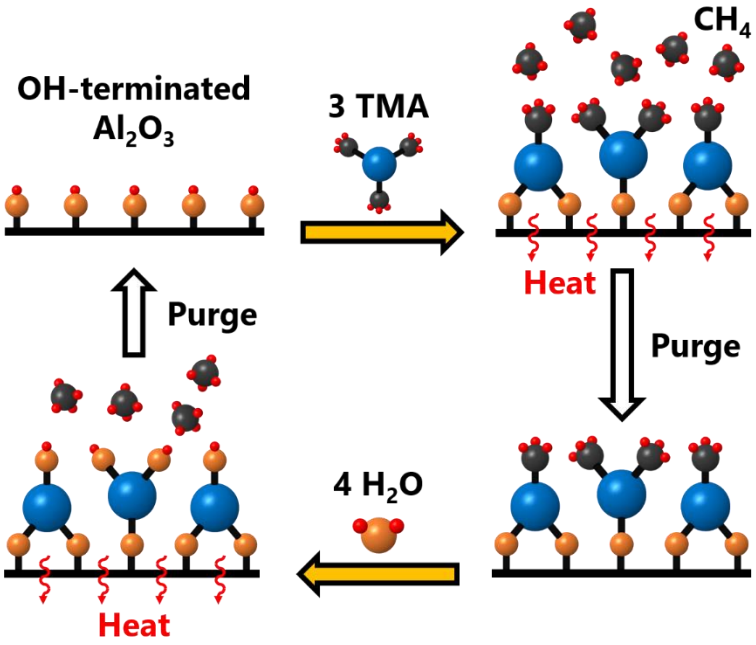

Figure 5.1. Scheme of one ALD dosing cycle using TMA and H_2O to produce Al_2O_3. Clockwise from top left: gaseous TMA is introduced to a hydroxyl-terminated surface where it reacts, producing surface bound MMA and DMA species, gaseous CH_4, and heat (Reaction A in text). Since there are two MMAs and one DMA, $x = 5/3$ for Reaction A in this example. Then, following a purge with pure N_2, H_2O vapor is introduced and reacts with the remaining CH_3 groups, producing Al-bound –OH groups, gaseous CH_4, and heat (Reaction B in text). Not shown are bonds that also form between the Al atoms and non-hydroxyl oxygen atoms of the alumina surface (see text). Elements have the color scheme: Al, blue; O, orange; C, black; H, red.

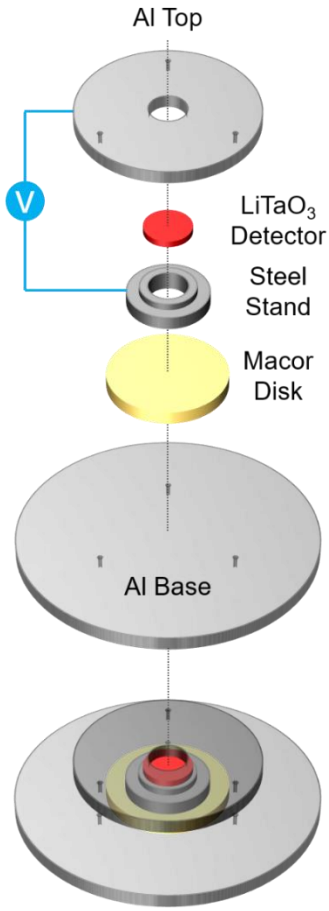

Figure 5.2. Assembled ALD calorimeter at 45° perspective (bottom) with exploded view (top). The heat detector (red) is a 50 µm thick pyroelectric $LiTaO_3$ crystal disk (10 mm in diameter) coated on both sides with 25 nm of gold. These sides act as the signal electrodes which are connected to a preamplifier to read transient voltage signal. The detector is placed on top of a stainless steel stand with a spot-welded signal wire (blue). The stand is electrically isolated from the rest of the calorimeter housing by the $LiTaO_3$ crystal and a 2.54 cm diameter Macor ceramic disk (yellow). The above pieces are sandwiched between a circular base and annular top constructed of aluminum which are connected, physically and electrically, using three screws separated by 120° (not shown). The top piece has an 8.66 mm diameter orifice in the center which exposes the front $LiTaO_3$ crystal face to gases in the ALD chamber, so that the heat associated with film growth on that face is monitored. The top face of the $LiTaO_3$ crystal is grounded to the chamber through the aluminum housing, and this is used as the reference signal.

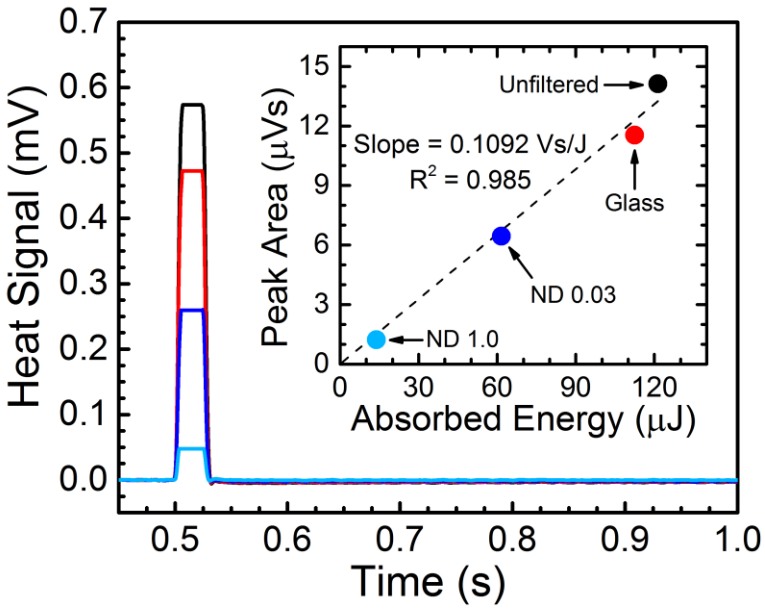

Figure 5.3. True heat signal in mV as a function of time measured by the calorimeter in response to a 25 ms pulse of light through a window on the chamber lid. Unfiltered light (black), glass slide (red), and neutral density filters ND 0.03 (dark blue) and ND 1.0 (light blue). The glass slide reflects ~6% of the light, while the ND 0.03 and ND 1.0 filters transmit 50.1% and 10% of the light, respectively. Each curve is an average of 20 pulses. The inset shows the integrated peak area in μVs as a function of the energy absorbed from the light source in μJ.

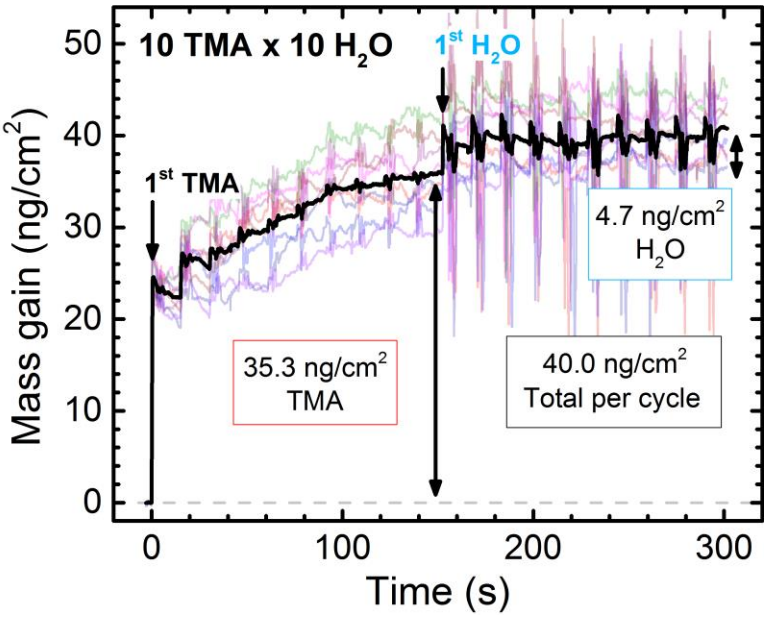

Figure 5.4. (Black line) Average QCM mass gain in ng/cm^2 as a function of time over four cycles of 10 pulses TMA and 10 pulses H_2O at 125°C. (Colored lines are individual cycles.) This average was calculated from the mass gain measured over four cycles using two QCMs, with one mounted near the gas inlet and one near the outlet. A total mass change of ~40.0 ng/cm^2 is measured during one complete cycle: ~35.3 ng/cm^2 during the TMA half-cycle and ~4.7 ng/cm^2 for the H_2O half-cycle.

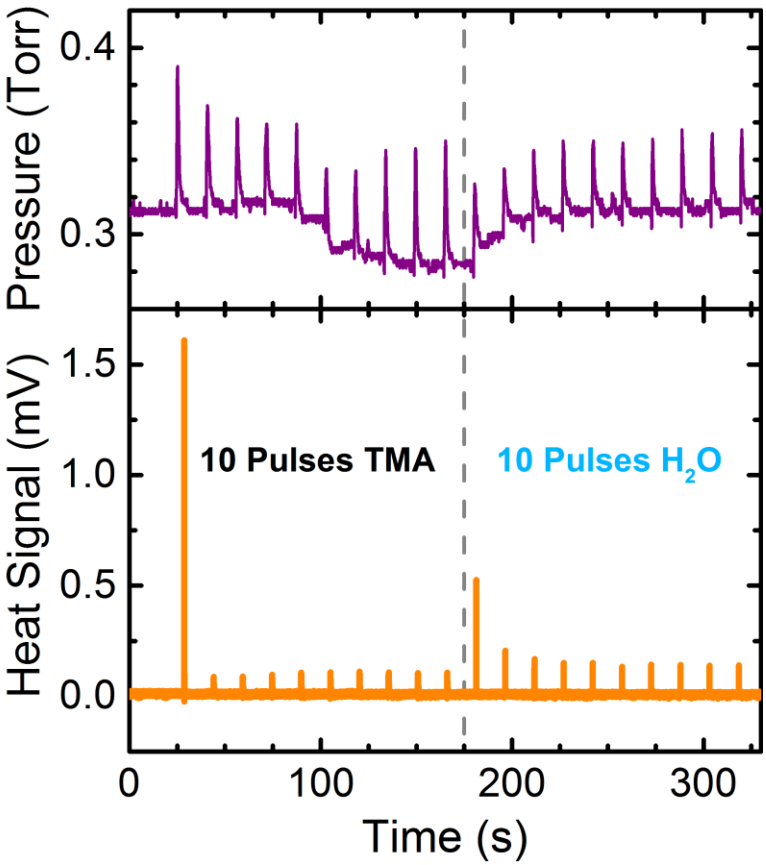

Figure 5.5. (Top) The total ALD chamber's pressure in Torr as a function of time over a typical 20-pulse cycle consisting of 10 pulses TMA followed by 10 pulses H_2O onto the alumina-precoated detector surface at 125°C. The chamber was purged with 20 sccm of N_2 for 15 s after each pulse. This N_2 was also flowing during the pulses. (Bottom) The true heat signal in mV as a function of time over the course of a typical cycle taken simultaneously with the pressure and QCM data.

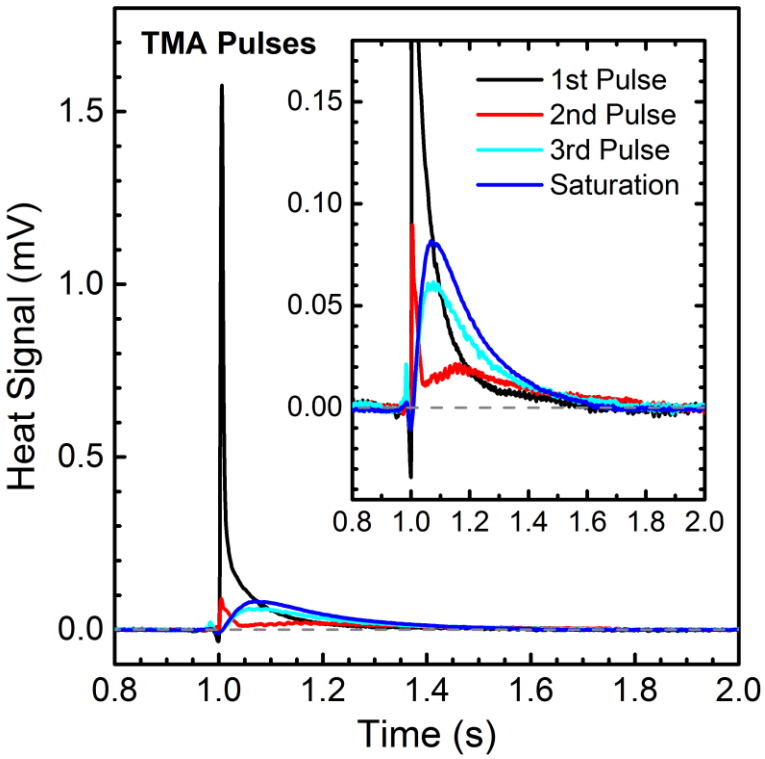

Figure 5.6. Overlaid heat signals during TMA pulses onto the alumina-precoated detector surface at 125°C, averaged for five consecutive cycles with the first pulse in black, second pulse in red, and third pulse in cyan. After the third pulse, the surface is effectively saturated (as shown in **Figure 5.4** and **5.5**), so the seven subsequent pulses were averaged together over each of five cycles (35 pulses total), as shown in dark blue.

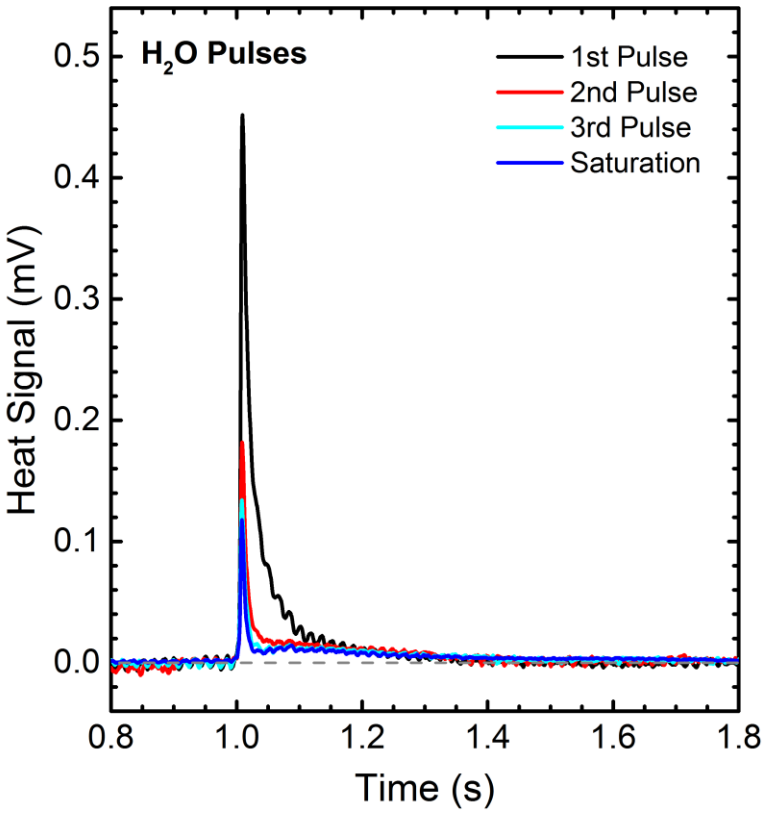

Figure 5.7. Overlaid heat signals during H_2O pulses onto the alumina-precoated detector surface at 125°C, immediately following the 10 TMA pulses of **Figure 5.6**, averaged over five consecutive cycles, with the first pulse in black, second pulse in red, and third pulse in cyan. After the third pulse, the surface is effectively saturated (as shown in **Figure 5.4** and **5.5**), so the seven subsequent pulses were averaged together over each of the five cycles (35 pulses total), as shown in dark blue.

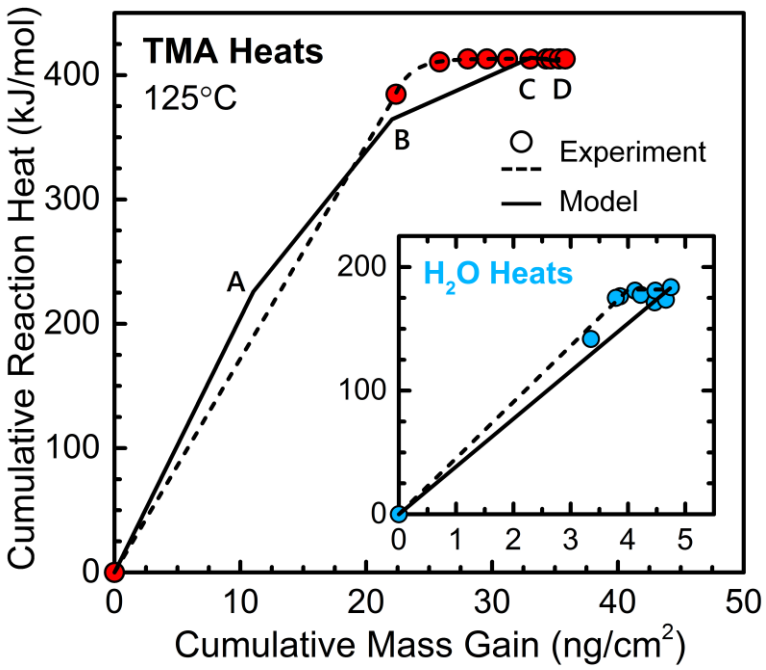

Figure 5.8. Reaction heats in kJ per mol Al from experiment (circles) and the best fits to the data (dashed lines) as a function of QCM mass gain over 10 TMA pulses and 10 H_2O pulses (inset) measured at 125°C. The bond additivity model (solid lines) predicts that TMA first reacts to form adsorbed MMA (x = 2) with a y value of 3 until 35% of the total reaction has occurred (point A) and thereafter with y = 2 until 70% of the total reaction has occurred and all sites that can react with x = 2 are titrated (point B). Then TMA reacts to form DMA (x = 1) with a y value of 1 until 95% of the surface is saturated (point C). Finally, TMA reacts to form DMA (x = 1) with a y value of 0 until the surface is saturated with adsorbed DMA and MMA (point C). In the case of H_2O, the reaction proceeds linearly until saturation because there is no significantly more favorable reaction for H_2O.

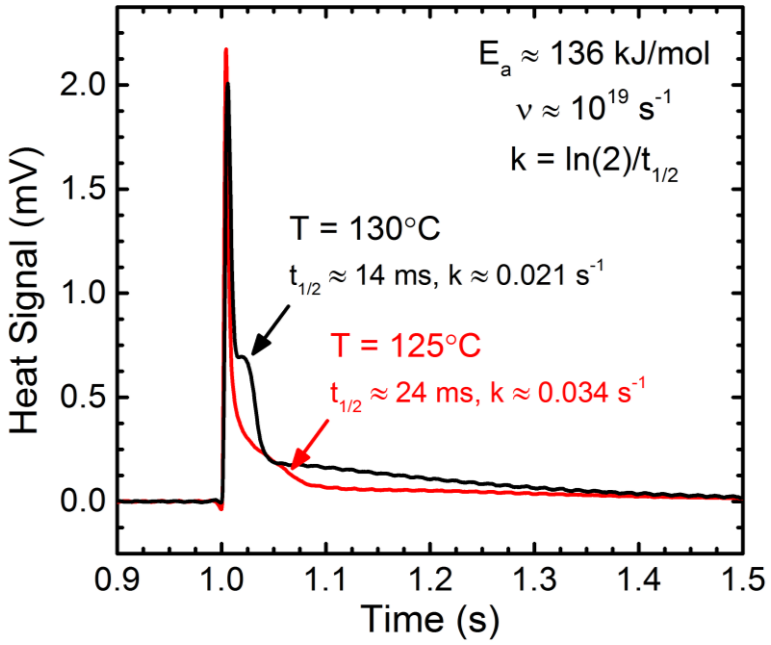

Figure 5.9. Comparison of heat signals measured during the first TMA pulse at 125°C (red) and 130°C (black), using open-valve pulses. Estimated kinetic half-lives ($t_{1/2}$) for the shoulder peak at 125°C and 130°C are 24 ms and 14 ms, respectively, corresponding to first-order rate constants of 0.034 s^{-1} and 0.021 s^{-1}, respectively. Arrhenius analysis of these rate constants gives an apparent activation energy of ~136 kJ/mol and a prefactor of 10^{19} s^{-1}.

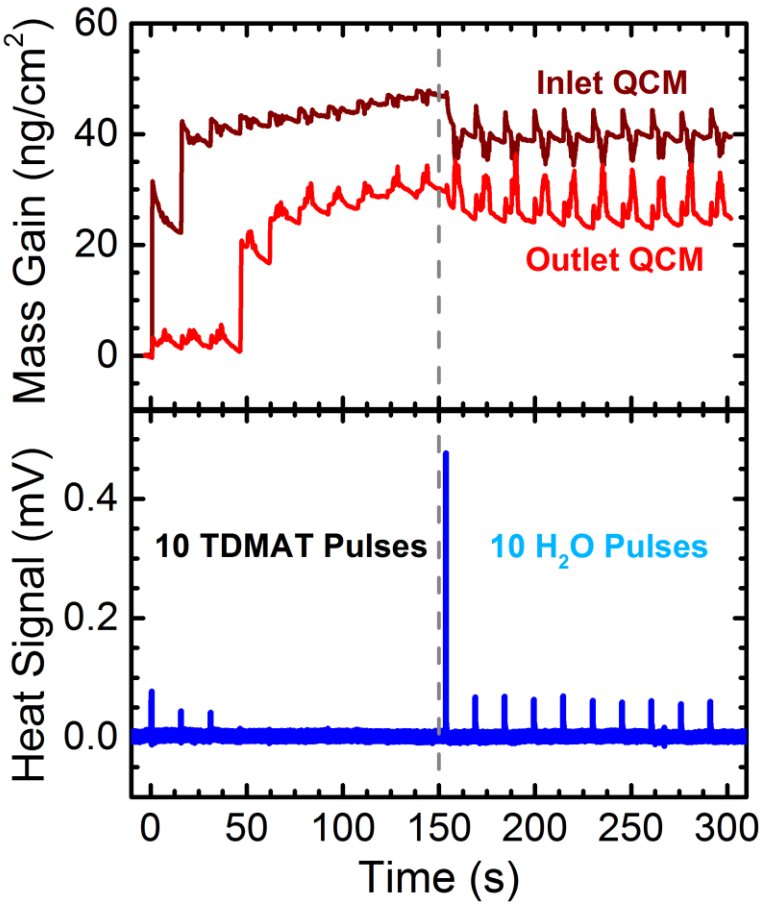

Figure 5.10. Mass gain/loss and calorimetry during ALD growth of TiO_2. (Top) Average QCM mass gains in ng/cm^2 as a function of time over five closed-valve cycles of 10 pulses TDMAT and 10 pulses H_2O at 120°C, measured on the inlet (brown) and outlet (red) QCMs. (Bottom) The raw heat signal in mV as a function of time over the course of a typical 10 x 10 TDMAT–H_2O cycle.

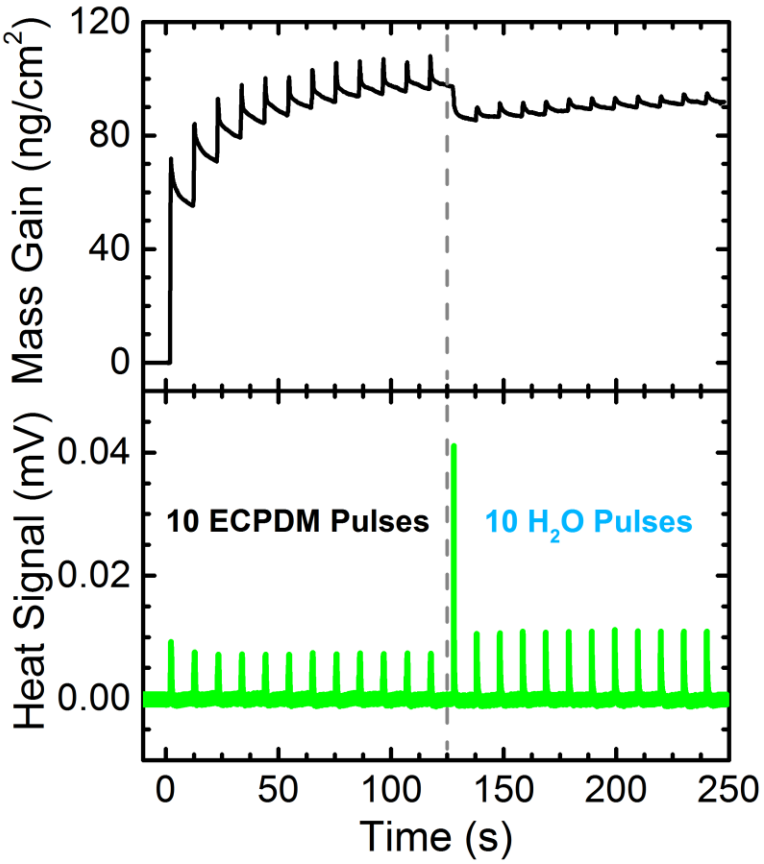

Figure 5.11. Mass gain/loss and calorimetry during ALD growth of MnO. (Top) Average QCM mass gains in ng/cm^2 as a function of time over five open-valve cycles of 12 pulses ECPDM and 12 pulses H_2O at 120°C, measured on the outlet QCM. (Bottom) The raw heat signal in mV as a function of time over the course of a typical 12 x 12 ECPDM–H_2O cycle.

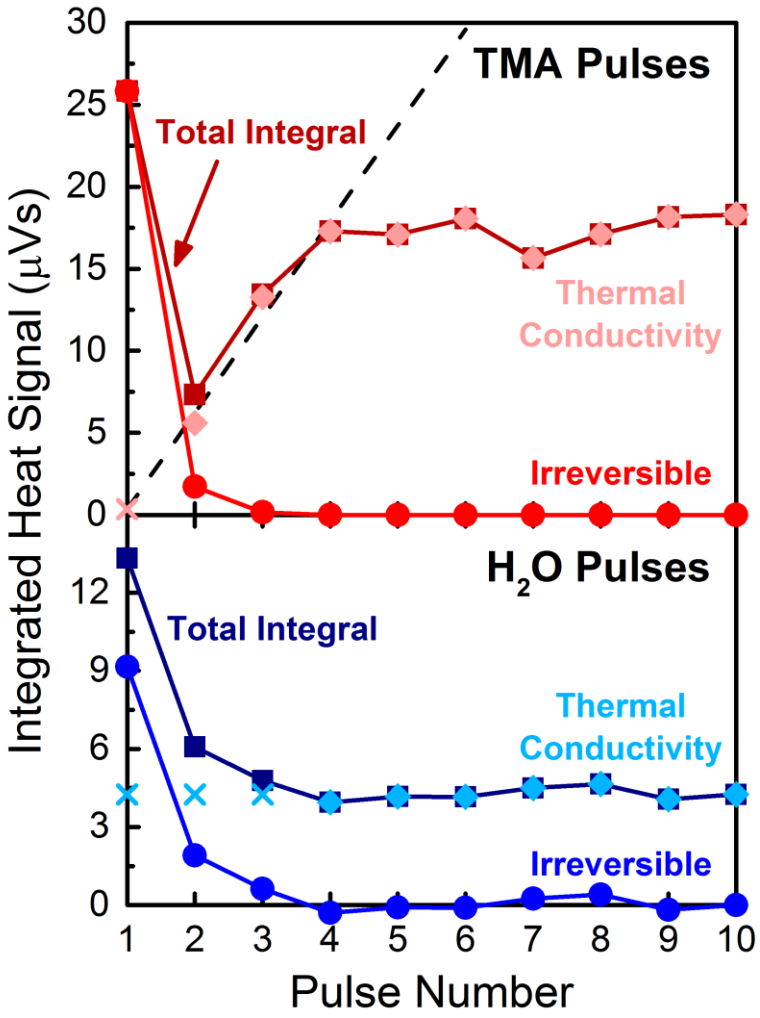

Figure 5.12. (Top) Time-integrated heat signal of TMA pulses vs. pulse number from the data of **Figure 5.6**. Total integrated areas (integrated from the onset of the heat signal to 0.5 s afterward) are shown in maroon squares. Separate contributions to the total areas from irreversible adsorption and from changes in the gas's thermal conductivity are shown in red circles and pink diamonds, respectively. The dashed line indicates the increasing areas of the peaks due to thermal conductivity change from TMA pulses 2-4, extrapolated to show the expected area in the first pulse (as indicated by the pink X). (Bottom) Equivalent plot for H_2O pulses vs. pulse number, showing the total time-integrated signal (navy squares), and separate contributions due to irreversible adsorption (blue circles) and thermal conductivity changes (light blue diamonds and X's).

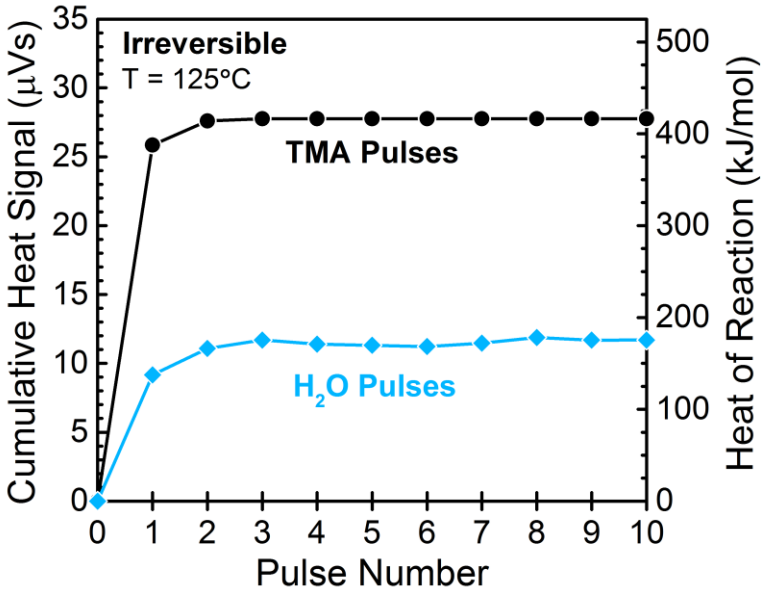

Figure 5.13. Cumulative time-integrated heat signals pertaining to irreversible adsorption plotted vs. pulse number for pulses of TMA (black circles) and H_2O (blue diamonds). Right-hand axis shows the corresponding heat in kJ per mol of Al calibrated using the net reaction heat to form amorphous Al_2O_3 (594 kJ/mol).

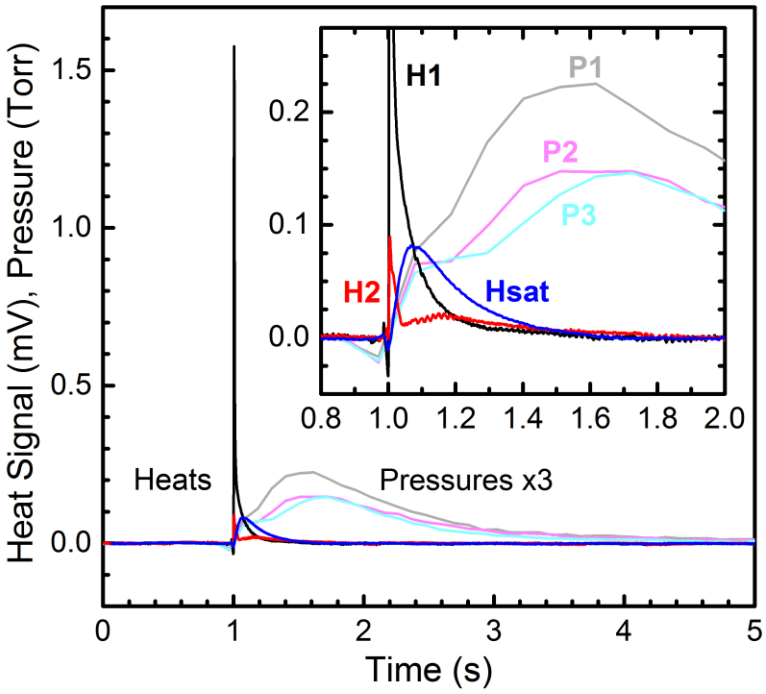

Figure 5.14. Average heat signals in mV for the first (black, H1), second (red, H2), and saturation (blue, Hsat) doses of TMA along with pressure readings in Torr for the first (grey, P1), second (pink, P2), and third (cyan, P3) doses of TMA. The inset shows a close-up at a shorter time scale. This comparison shows that the heat signal at saturation follows the growth in TMA pressure, consistent with the transient heating of the sample that accompanies the decrease in thermal conductivity of the gas above the sample (and therefore the decrease in cooling by this gas) as the TMA gas pulse passes the sample. This subsequent re-cooling of the sample after the pulse has passed is stretched out over such a long time before the next TMA gas pulse arrives 15 s later that it does not show a negative heat signal that is clearly distinguishable below the small baseline drift, although it should have the same negative integrated area as under the blue curve.

TABLES

Table 5.1. ALD precursors used in this work to produce metal oxide surfaces *via* reaction with H_2O.

Surface	Metal Source	Abbreviation	Structure
Al_2O_3	Trimethylaluminum	TMA	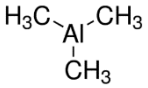
TiO_2	Tetrakis(dimethylamino)titanium	TDMAT	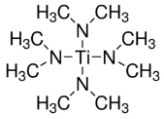
MnO	Bis(ethylcyclopentadienyl)manganese	$Mn(EtCp)_2$	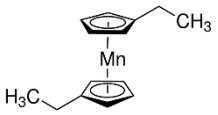

Table 5.2. Procedures for the reactions investigated in this work. Experiments followed a $(t_1–t_2)_n–(t_3–t_4)_n$ procedure where t_1 is the metal precursor pulse time, t_2 is the metal precursor purge time, t_3 is the water pulse time, and t_4 is the water purge time, all in seconds, and n is the number of consecutive pulses of each precursor.

ALD Experiment	Valve Position	T (°C)	t_1 (s)	t_2 (s)	t_3 (s)	t_4 (s)	n
TMA–H_2O	Closed	125	0.1	15	0.1	15	10
TMA–H_2O	Open	125	0.015	15	0.015	15	10
TDMAT–H_2O	Closed	120	0.2	15	0.2	15	10
ECPDM–H_2O	Open	120	0.3	10	0.015	10	12

Table 5.3. Average bond enthalpies in kJ per mole of bonds estimated from NIST tables of standard heats of formation,[232] using the listed reactions. The last column lists the numbers of bonds of that type made or broken in the NET Reaction: 2 $Al(CH_3)_3(g)$ + 3 $H_2O(g)$ → $Al_2O_3(s)$ + 6 $CH_4(g)$.

Bond	**Bond enthalpy (kJ/mol)**	**Reaction used to estimate average bond enthalpy (and its enthalpy)**	**Bonds formed or broken per Al_2O_3**
Al–CH_3	284.5	$Al(CH_3)_3(g)$ → $Al(g)$ + 3 $CH_3(g)$ (853.6 kJ/mol)	6 broken
O–H	463.5	$H_2O(g)$ → 2 $H(g)$ + $O(g)$ (927.0 kJ/mol)	6 broken
Al–O	256.9	$Al_2O_3(s)$ → 2 $Al(g)$ + 3 $O(g)$ (3083 kJ/mol)	12 formed
H–CH_3	438.6	$CH_4(g)$ → $H(g)$ + $CH_3(g)$ (438.6 kJ/mol)	6 formed

Table 5.4. TMA and H_2O half-reaction heats (kJ per mol of Al, or per 3/2 mol of H_2O) for x = 1.7 in this work and the literature.

Reference	Method	(*x*, *y*)	Reaction Heats (kJ per mol Al)			Ratio
			TMA ½ Reaction	H_2O ½ Reaction	Total	
This work	Calorimetry: Net Heat Calibration	(1.7, ?)	-413	-181	-594	2.28
This work	Bond Additivity/ NIST ΔH_f	(1.7, 2)	-411	-183	-594	2.25
(217)	Cluster DFT	(1, 0)	-164	-143	-307	1.15
		(2, 0)	-269	-125	-394	2.15
		(1.7, 0)	-238	-130	-368	1.82
	+ 2 Al–O_l bonds	(1.7, **2**)	--	--	-882	--
(222)	Periodic DFT α-Al_2O_3	(1, 0)	-177	-257	-433	0.69
		(2, 1)	-310	-122	-431	2.55
		(1.7, 0.7)	-270	-162	-432	1.66
	+ 1.3 Al–O_l bonds	(1.7, **2**)	--	--	-766	--
(223)	Periodic DFT γ-Al_2O_3	(1, 1)	-264	-207	-471	1.28
		(2, 1)	-341	-74	-415	4.61
		(1.7, 1)	-318	-114	-432	2.79
	+ 1 Al–O_l bond	(1.7, **2**)	--	--	-689	--

Conclusion

Global climate change is a problem that must be addressed through a multifaceted approach involving the development of new energy conversion technologies, more efficient catalysts, and materials capable of large volume carbon capture. The most promising source of renewable energy is solar, as sunlight is clean, free, and abundant mostly everywhere on Earth. In fact, enough solar radiation strikes the Earth's surface every day to meet the world's *annual* energy requirements.[5] Over the last 25 years, intensive research has been focused on the development of organic photovoltaics (OPV), "third-generation" solar cells that can be produced cheaply and scaled to cover large areas. Another way to address climate change is *via* improved efficiency of industrial processes using better catalysts, and the search is ongoing for new catalysts with high selectivity and activity. One class of compounds that is very appealing for catalysis (as well as carbon capture and separations) is metal-organic frameworks (MOFs). MOFs are extremely versatile materials composed of small metal or metal oxide node connected by organic linker groups of a fixed length and conformation, forming highly ordered, porous structures with large surface areas. Since the nodes in many MOFs are oxide clusters of controllable sizes near ~1 nm in diameter, they can be thought of as very well-defined and homogeneous oxide "nano-supports" to which catalytic metals can be attached to improve activity or simply to provide a more homogeneous and well-defined structure to facilitate fundamental studies of oxide-supported metal clusters.

In this dissertation, adsorption calorimetry was used in concert with surface spectroscopies in ultrahigh vacuum (UHV) to study the adsorption of calcium metal onto phenyl-C_{61}-butyric acid methyl ester (PCBM), by far the most well-studied and prominently-used electron accepting material in OPV. Calcium metal, due to its very low work function, is commonly used as a cathode material in normal OPV devices, making the Ca/PCBM interface critically important for

understanding device performance and stability. This study revealed a tendency for Ca metal to diffuse subsurface over 10 nm deep and react aggressively with subsurface methyl ester groups of PCBM to make the Ca carboxylate of PCBM.

Next, a comprehensive experimental and theoretical study of Ca metal on the MOF NU-1000 was presented. NU-1000 is a particularly promising MOF for catalysis because of its water- and temperature-stability, and large porosity and surface area. Our results revealed a tendency for Ca metal to diffuse subsurface over 20 nm deep to react strongly with the hydroxyl- and H_2O-terminated nodes producing $Ca(OH)_2$ nanoparticles. This is the first study where the interaction of metal atoms with the metal-oxide cluster nodes of *any* MOF has been characterized in detail with respect to experimental bonding energetics, and it provides a crucial benchmark for computational models of metal bonding to the oxide nodes in MOFs.

Finally, this dissertation presented the first-ever calorimetric measurements of the adsorption of precursors used in atomic layer deposition (ALD) using a specially-designed calorimeter. According to the ISI Web of Science, journal articles on the topic of ALD were cited >32,000 in the year 2015 alone, a trend which has grown exponentially since the first publication in 1981. ALD is a versatile technique for depositing uniform thin films of precision thickness with exceptional conformity to underlying substrates, even when the surfaces are extremely complex. It has been applied to a wide range of fields including semiconductors, batteries, biomaterials, photovoltaics, and catalysis, including OPVs and MOFs, making this study a perfect complement to our UHV adsorption calorimetry experiments. Unique to ALD is the sequential, self-limiting surface reactions that are separated in time by inert gas purging. We focused on the sequential reaction of trimethylaluminum and water to make Al_2O_3, by far the most extensively studied ALD reaction scheme and the focus of numerous review papers, which cycles between a methylated and

hydroxylated surface. We show that the reaction heat of the first half-reaction is ~426 kJ/mol and that for the second half-reaction is ~187 kJ/mol (both exothermic). These measured energies will enable future computational studies to verify the nature of the surface intermediates involved in the elementary steps of this highly important ALD process to make conformal alumina films. We then extend this new ALD calorimetry technique to the formation of three other relevant oxides films by ALD—TiO_2, MnO, and one other process to make Al_2O_3—to highlight the technique's versatility.

Taken together, the work presented in this dissertation represents an attempt at deeper understanding of interfaces pertinent to the broad fields of energy conversion and carbon capture, and these results will help to guide the development of efficient new technologies, which is vitally important in order to address the global issue of climate change. The calorimetric study of Ca on PCBM is perhaps the most fundamentally significant study yet produced by our group on metal-organic interfaces, and serves as a perfect complement to the suite of studies by our group of Ca metal adsorption on organic semiconducting polymers. We also applied our UHV adsorption calorimetry technique to perform the first-ever study of metal adsorption on the nodes of any MOF, providing a benchmark for validating the energy accuracy of the computational methods used to model metal bonding to the oxide nodes in MOFs, and to oxide clusters in general. Finally, the introduction here of the first calorimeter for measuring heats of adsorption of ALD precursors has vast potential for future applications, as ALD is a uniquely capable technique with wide-ranging applicability, but very little is known about the enthalpies involved during ALD half-reactions. Moreover, the accuracy of computational methods used for calculating these energies, such as density functional theory, is not known without such experimental energies to reference. Thus, our calorimeter will provide valuable benchmark energies for ALD reactions on surfaces, with future

applications in syntheses of a broad range of materials, such as catalysts, photovoltaics, microelectronics, sensors, biomaterials and coatings, all of broad interest to the scientific community.

References

(1) "Energy and Climate Outlook," MIT Joint Program on the Science and Policy of Global Change, 2014.

(2) "CO_2 Emissions from Fuel Combustion: Highlights," International Energy Agency, 2015.

(3) "IPCC Fifth Assessment Report," Intergovernmental Panel on Climate Change, 2014.

(4) "CCS 2014 - What Lies in Store for CCS?," International Energy Agency, 2014.

(5) Tsao, J.; Lewis, N.; Crabtree, G.; Sandia National Laboratory, 2006.

(6) Feldman, D.; Barbose, G.; Margolis, R.; James, T.; Weaver, S.; Darghouth, N.; Fu, R.; Davidson, C.; Booth, S.; Wiser, R. "Photovoltaic System Pricing Trends: Historical, Recent, and Near-Term Projections," SunShot US Department of Energy, 2014.

(7) Green, M. A.; Emery, K.; Hishikawa, Y.; Warta, W.; Dunlop, E. D. Solar cell efficiency tables (version 47). *Progress in Photovoltaics* **2016,** *24* (1), 3.

(8) "NCPV at NREL. Research Cell Efficiency Records.," National Renewable Energy Laboratory, 2016.

(9) Jackson, P.; Hariskos, D.; Lotter, E.; Paetel, S.; Wuerz, R.; Menner, R.; Wischmann, W.; Powalla, M. New world record efficiency for Cu(In,Ga)Se-2 thin-film solar cells beyond 20%. *Progress in Photovoltaics* **2011,** *19* (7), 894.

(10) Gratzel, M. Recent Advances in Sensitized Mesoscopic Solar Cells. *Accounts of Chemical Research* **2009,** *42* (11), 1788.

(11) O'Regan, B.; Gratzel, M. A Low-Cost, High-Efficiency Solar-Cell Based on Dye-Sensitized Colloidal TiO2 Films. *Nature* **1991,** *353* (6346), 737.

(12) Hoppe, H.; Sariciftci, N. S. Organic Solar Cells: An Overview. *J. Mater. Res.* **2004,** *19* (7), 1924.

(13) Snaith, H. J. Perovskites: The Emergence of a New Era for Low-Cost, High-Efficiency Solar Cells. *Journal of Physical Chemistry Letters* **2013,** *4* (21), 3623.

(14) Fahlman, M.; Salaneck, W. R. Surfaces and Interfaces in Polymer-Based Electronics. *Surf. Sci.* **2002,** *500* (1-3), 904.

(15) Ratcliff, E. L.; Zacher, B.; Armstrong, N. R. Selective Inter layers and Contacts in Organic Photovoltaic Cells. *J. Phys. Chem. Lett.* **2011,** *2* (11), 1337.

(16) Braun, S.; Salaneck, W. R.; Fahlman, M. Energy-Level Alignment at Organic/Metal and Organic/Organic Interfaces. *Adv. Mater.* **2009,** *21* (14-15), 1450.

(17) Chen, D. A.; Nakahara, A.; Wei, D. G.; Nordlund, D.; Russell, T. P. P3HT/PCBM Bulk Heterojunction Organic Photovoltaics: Correlating Efficiency and Morphology. *Nano Lett.* **2011,** *11* (2), 561.

(18) Bertrand, P.; Lambert, P.; Travaly, Y. Polymer Metallization: Low Energy Ion Beam Surface Modification to Improve Adhesion. *Nucl. Instr. Meth. Phys. Res. B* **1997,** *131* (1-4), 71.

(19) Bebin, P.; Prud'homme, R. E. Comparative XPS study of copper, nickel, and aluminum coatings on polymer surfaces. *Chemistry of Materials* **2003,** *15* (4), 965.

(20) Faupel, F.; Willecke, R.; Thran, A. Diffusion of metals in polymers. *Materials Science & Engineering R-Reports* **1998,** *22* (1), 1.

(21) Ettedgui, E.; Razafitrimo, H.; Gao, Y.; Hsieh, B. R. Band Bending Modified Tunneling at Metal/Conjugated Polymer Interfaces. *Applied Physics Letters* **1995,** *67* (18), 2705.

(22) Zhu, J.; Bebensee, F.; Hieringer, W.; Zhao, W.; Baricuatro, J. H.; Farmer, J. A.; Bai, Y.; Steinrueck, H.-P.; Gottfried, J. M.; Campbell, C. T. Formation of the Calcium/Poly(3-Hexylthiophene) Interface: Structure and Energetics. *J. Am. Chem. Soc.* **2009,** *131* (37), 13498.

(23) Bebensee, F.; Zhu, J.; Baricuatro, J. H.; Farmer, J. A.; Bai, Y.; Steinrueck, H.-P.; Campbell, C. T.; Gottfried, J. M. Interface Formation between Calcium and Electron-Irradiated Poly(3-hexylthiophene). *Langmuir* **2010,** *26* (12), 9632.

(24) Bebensee, F.; Schmid, M.; Steinrueck, H.-P.; Campbell, C. T.; Gottfried, J. M. Toward Well-Defined Metal-Polymer Interfaces: Temperature-Controlled Suppression of Subsurface Diffusion and Reaction at the Calcium/Poly(3-Hexylthiophene) Interface. *J. Am. Chem. Soc.* **2010,** *132* (35), 12163.

(25) Sharp, J. C.; Bebensee, F.; Baricuatro, J. H.; Steinrueck, H. P.; Gottfried, J. M.; Campbell, C. T. Calcium Thin Film Growth on a Cyano-Substituted Poly(p-phenylene vinylene): Interface Structure and Energetics. *J. Phys. Chem. C* **2013,** *117* (45), 23781.

(26) Sharp, J. C.; Feng, X. F.; Farmer, J. A.; Guo, Y. X.; Bebensee, F.; Baricuatro, J. H.; Zillner, E.; Zhu, J. F.; Steinrueck, H. P.; Gottfried, J. M.et al. Calcium Thin Film Growth

on Polyfluorenes: Interface Structure and Energetics. *J. Phys. Chem. C* **2014,** *118* (6), 2953.

(27) Diaz, S. F.; Zhu, J. F.; Harris, J. J. W.; Goetsch, P.; Merte, L. R.; Campbell, C. T. Heats of Adsorption of Pb on Pristine and Electron-Irradiated Poly(methyl methacrylate) by Microcalorimetry. *Surf. Sci.* **2005,** *598* (1-3), 22.

(28) Zhu, J.; Goetsch, P.; Ruzycki, N.; Campbell, C. T. Adsorption Energy, Growth Mode, and Sticking Probability of Ca on Poly(methyl methacrylate) Surfaces with and without Electron Damage. *J. Am. Chem. Soc.* **2007,** *129* (20), 6432.

(29) Ju, H.; Feng, X.; Ye, Y.; Zhang, L.; Pan, H.; Campbell, C. T.; Zhu, J. Ca Carboxylate Formation at the Calcium/Poly(methyl methacrylate) Interface. *J. Phys. Chem. C* **2012,** *116* (38), 20465.

(30) Ju, H.; Ye, Y.; Feng, X.; Pan, H.; Zhu, J.; Ruzycki, N.; Campbell, C. T. Low-Temperature Growth Improves Metal/Polymer Interfaces: Vapor-Deposited Ca on PMMA. *J. Phys. Chem. C* **2014,** *118* (12), 6352.

(31) Minh Trung, D.; Hirsch, L.; Wantz, G. P3HT:PCBM, Best Seller in Polymer Photovoltaic Research. *Adv. Mater.* **2011,** *23* (31), 3597.

(32) Bartelt, J. A.; Beiley, Z. M.; Hoke, E. T.; Mateker, W. R.; Douglas, J. D.; Collins, B. A.; Tumbleston, J. R.; Graham, K. R.; Amassian, A.; Ade, H., et al. The Importance of Fullerene Percolation in the Mixed Regions of Polymer-Fullerene Bulk Heterojunction Solar Cells. *Adv. Energy Mater.* **2013,** *3* (3), 364.

(33) Chen, L.-M.; Hong, Z. R.; Li, G.; Yang, Y. Recent Progress in Polymer Solar Cells: Manipulation of Polymer: Fullerene Morphology and the Formation of Efficient Inverted Polymer Solar Cells. *Adv. Mater.* **2009,** *21* (14-15), 1434.

(34) Bull, T. A.; Pingree, L. S. C.; Jenekhe, S. A.; Ginger, D. S.; Luscombe, C. K. The Role of Mesoscopic PCBM Crystallites in Solvent Vapor Annealed Copolymer Solar Cells. *ACS Nano* **2009,** *3* (3), 627.

(35) Li, C. Z.; Yip, H. L.; Jen, A. K. Y. Functional Fullerenes for Organic Photovoltaics. *J. Mater. Chem.* **2012,** *22* (10), 4161.

(36) Yu, G.; Gao, J.; Hummelen, J. C.; Wudl, F.; Heeger, A. J. Polymer Photovoltaic Cells - Enhanced Efficiencies via a Network of Internal Donor-Acceptor Heterojunctions. *Science* **1995,** *270* (5243), 1789.

(37) Dou, L. T.; You, J. B.; Hong, Z. R.; Xu, Z.; Li, G.; Street, R. A.; Yang, Y. 25th Anniversary Article: A Decade of Organic/Polymeric Photovoltaic Research. *Adv. Mater.* **2013,** *25* (46), 6642.

(38) Reese, M. O.; White, M. S.; Rumbles, G.; Ginley, D. S.; Shaheen, S. E. Optimal Negative Electrodes for Poly(3-hexylthiophene) : 6,6-Phenyl-C61-Butyric Acid Methyl Ester Bulk Heterojunction Photovoltaic Devices. *Appl. Phys. Lett.* **2008,** *92* (5), 053307.

(39) Chen, L.-M.; Xu, Z.; Hong, Z.; Yang, Y. Interface Investigation and Engineering - Achieving High Performance Polymer Photovoltaic Devices. *J. Mater. Chem.* **2010,** *20* (13), 2575.

(40) Mazzio, K. A.; Luscombe, C. K. The future of organic photovoltaics. *Chemical Society Reviews* **2015,** *44* (1), 78.

(41) Hodes, G. Perovskite-Based Solar Cells. *Science* **2013,** *342* (6156), 317.

(42) Stranks, S. D.; Snaith, H. J. Metal-halide perovskites for photovoltaic and light-emitting devices. *Nature Nanotechnology* **2015,** *10* (5), 391.

(43) Ruhle, S.; Shalom, M.; Zaban, A. Quantum-Dot-Sensitized Solar Cells. *Chemphyschem* **2010,** *11* (11), 2290.

(44) "The Future of Solar Energy: An Interdisciplinary MIT Study led by the MIT Energy Initiative," MIT Energy Initiative, 2015.

(45) Thomas, J. M.; Thomas, W. J. *Principles and practice of heterogeneous catalysis*; 1st ed.; Weinheim: New York, 2008.

(46) Ertl, G. *Reactions at Solid Surfaces*; 1st ed.; John Wiley & Sons, Inc.: Hoboken, NJ, 2009.

(47) Norskov, J. K.; Bligaard, T.; Rossmeisl, J.; Christensen, C. H. Towards the computational design of solid catalysts. *Nature Chemistry* **2009,** *1* (1), 37.

(48) Blaser, H. U.; Malan, C.; Pugin, B.; Spindler, F.; Steiner, H.; Studer, M. Selective hydrogenation for fine chemicals: Recent trends and new developments. *Advanced Synthesis & Catalysis* **2003,** *345* (1-2), 103.

(49) Rostrup-Nielsen, J. R.; Nielsen, R. Fuels and energy for the future: The role of catalysis. *Catalysis Reviews-Science and Engineering* **2004,** *46* (3-4), 247.

(50) Fechete, I.; Wang, Y.; Vedrine, J. C. The past, present and future of heterogeneous catalysis. *Catalysis Today* **2012,** *189* (1), 2.

(51) Ferey, G. Hybrid Porous Solids: Past, Present, Future. *Chemical Society Reviews* **2008,** *37* (1), 191.

(52) Taguchi, A.; Schuth, F. Ordered mesoporous materials in catalysis. *Microporous and Mesoporous Materials* **2005,** *77* (1), 1.

(53) Venuto, P. B. Organic Catalysis Over Zeolites - A Perspective on Reaction Paths Within Micropores. *Microporous Materials* **1994,** *2* (5), 297.

(54) Weckhuysen, B. M.; Yu, J. H. Recent advances in zeolite chemistry and catalysis. *Chemical Society Reviews* **2015,** *44* (20), 7022.

(55) Shekhah, O.; Wang, H.; Kowarik, S.; Schreiber, F.; Paulus, M.; Tolan, M.; Sternemann, C.; Evers, F.; Zacher, D.; Fischer, R. A.et al. Step-by-Step Route for the Synthesis of Metal-Organic Frameworks. *Journal of the American Chemical Society* **2007,** *129* (49), 15118.

(56) Farha, O. K.; Eryazici, I.; Jeong, N. C.; Hauser, B. G.; Wilmer, C. E.; Sarjeant, A. A.; Snurr, R. Q.; Nguyen, S. T.; Yazaydin, A. O.; Hupp, J. T. Metal-Organic Framework Materials with Ultrahigh Surface Areas: Is the Sky the Limit? *Journal of the American Chemical Society* **2012,** *134* (36), 15016.

(57) Ferey, G.; Mellot-Draznieks, C.; Serre, C.; Millange, F. Crystallized Frameworks with Giant Pores: Are There Limits to the Possible? *Accounts of Chemical Research* **2005,** *38* (4), 217.

(58) Fletcher, A. J.; Thomas, K. M.; Rosseinsky, M. J. Flexibility in Metal-Organic Framework Materials: Impact on Sorption Properties. *Journal of Solid State Chemistry* **2005,** *178* (8), 2491.

(59) Lee, J.; Farha, O. K.; Roberts, J.; Scheidt, K. A.; Nguyen, S. T.; Hupp, J. T. Metal-organic framework materials as catalysts. *Chemical Society Reviews* **2009,** *38* (5), 1450.

(60) Valvekens, P.; Vermoortele, F.; De Vos, D. Metal-organic frameworks as catalysts: the role of metal active sites. *Catalysis Science & Technology* **2013,** *3* (6), 1435.

(61) Yang, D.; Odoh, S. O.; Borycz, J.; Wang, T. C.; Farha, O. K.; Hupp, J. T.; Cramer, C. J.; Gagliardi, L.; Gates, B. C. Tuning Zr-6 Metal-Organic Framework (MOF) Nodes as Catalyst Supports: Site Densities and Electron-Donor Properties Influence Molecular Iridium Complexes as Ethylene Conversion Catalysts. *Acs Catalysis* **2016,** *6* (1), 235.

(62) Yang, D.; Odoh, S. O.; Wang, T. C.; Farha, O. K.; Hupp, J. T.; Cramer, C. J.; Gagliardi, L.; Gates, B. C. Metal-Organic Framework Nodes as Nearly Ideal Supports for Molecular Catalysts: NU-1000-and UiO-66-Supported Iridium Complexes. *Journal of the American Chemical Society* **2015,** *137* (23), 7391.

(63) Mondloch, J. E.; Katz, M. J.; Isley, W. C., III; Ghosh, P.; Liao, P.; Bury, W.; Wagner, G.; Hall, M. G.; DeCoste, J. B.; Peterson, G. W.et al. Destruction of chemical warfare agents using metal-organic frameworks. *Nature Materials* **2015,** *14* (5), 512.

(64) Moon, S.-Y.; Liu, Y.; Hupp, J. T.; Farha, O. K. Instantaneous Hydrolysis of Nerve-Agent Simulants with a Six-Connected Zirconium-Based Metal-Organic Framework. *Angewandte Chemie-International Edition* **2015,** *54* (23), 6795.

(65) Li, J.-R.; Kuppler, R. J.; Zhou, H.-C. Selective gas adsorption and separation in metal-organic frameworks. *Chemical Society Reviews* **2009,** *38* (5), 1477.

(66) Seo, J. S.; Whang, D.; Lee, H.; Jun, S. I.; Oh, J.; Jeon, Y. J.; Kim, K. A homochiral metal-organic porous material for enantioselective separation and catalysis. *Nature* **2000,** *404* (6781), 982.

(67) Rosi, N. L.; Eckert, J.; Eddaoudi, M.; Vodak, D. T.; Kim, J.; O'Keeffe, M.; Yaghi, O. M. Hydrogen storage in microporous metal-organic frameworks. *Science* **2003,** *300* (5622), 1127.

(68) Eddaoudi, M.; Kim, J.; Rosi, N.; Vodak, D.; Wachter, J.; O'Keeffe, M.; Yaghi, O. M. Systematic design of pore size and functionality in isoreticular MOFs and their application in methane storage. *Science* **2002,** *295* (5554), 469.

(69) Peng, Y.; Krungleviciute, V.; Eryazici, I.; Hupp, J. T.; Farha, O. K.; Yildirim, T. Methane Storage in Metal-Organic Frameworks: Current Records, Surprise Findings, and Challenges. *Journal of the American Chemical Society* **2013,** *135* (32), 11887.

(70) Farha, O. K.; Wilmer, C. E.; Eryazici, I.; Hauser, B. G.; Parilla, P. A.; O'Neill, K.; Sarjeant, A. A.; Nguyen, S. T.; Snurr, R. Q.; Hupp, J. T. Designing Higher Surface Area Metal-Organic Frameworks: Are Triple Bonds Better Than Phenyls? *Journal of the American Chemical Society* **2012,** *134* (24), 9860.

(71) Wilmer, C. E.; Leaf, M.; Lee, C. Y.; Farha, O. K.; Hauser, B. G.; Hupp, J. T.; Snurr, R. Q. Large-scale screening of hypothetical metal-organic frameworks. *Nature Chemistry* **2012,** *4* (2), 83.

(72) Farha, O. K.; Hupp, J. T. Rational Design, Synthesis, Purification, and Activation of Metal-Organic Framework Materials. *Accounts of Chemical Research* **2010,** *43* (8), 1166.

(73) Zhou, H.-C.; Long, J. R.; Yaghi, O. M. Introduction to Metal-Organic Frameworks. *Chemical Reviews* **2012,** *112* (2), 673.

(74) Richardson, J. T. *Principles of Catalyst Development*; Plenum Press: New York, NY, 1989.

(75) Baerns, M.; Holena, M. *Combinatorial Development of Solid Catalytic Materials*; Imperial College Press: London, England, 2009.

(76) Ishii, H.; Sugiyama, K.; Ito, E.; Seki, K. Energy level alignment and interfacial electronic structures at organic metal and organic organic interfaces. *Advanced Materials* **1999,** *11* (8), 605.

(77) Hermes, S.; Schroter, M. K.; Schmid, R.; Khodeir, L.; Muhler, M.; Tissler, A.; Fischer, R. W.; Fischer, R. A. Metal@MOF: Loading of highly porous coordination polymers host lattices by metal organic chemical vapor deposition. *Angewandte Chemie-International Edition* **2005,** *44* (38), 6237.

(78) Meilikhov, M.; Yusenko, K.; Esken, D.; Turner, S.; Van Tendeloo, G.; Fischer, R. A. Metals@MOFs - Loading MOFs with Metal Nanoparticles for Hybrid Functions. *European Journal of Inorganic Chemistry* **2010,** (24), 3701.

(79) Puurunen, R. L. Surface chemistry of atomic layer deposition: A case study for the trimethylaluminum/water process. *Journal of Applied Physics* **2005,** *97* (12).

(80) George, S. M. Atomic Layer Deposition: An Overview. *Chemical Reviews* **2010,** *110* (1), 111.

(81) Knez, M.; Niesch, K.; Niinisto, L. Synthesis and surface engineering of complex nanostructures by atomic layer deposition. *Advanced Materials* **2007,** *19* (21), 3425.

(82) George, S. M.; Yoon, B.; Dameron, A. A. Surface Chemistry for Molecular Layer Deposition of Organic and Hybrid Organic-Inorganic Polymers. *Accounts of Chemical Research* **2009,** *42* (4), 498.

(83) Ferrari, S.; Perissinotti, F.; Peron, E.; Fumagalli, L.; Natali, D.; Sampietro, M. Atomic layer deposited Al2O3 as a capping layer for polymer based transistors. *Organic Electronics* **2007,** *8* (4), 407.

(84) Heo, J.; Hock, A. S.; Gordon, R. G. Low Temperature Atomic Layer Deposition of Tin Oxide. *Chemistry of Materials* **2010,** *22* (17), 4964.

(85) Mondloch, J. E.; Bury, W.; Fairen-Jimenez, D.; Kwon, S.; DeMarco, E. J.; Weston, M. H.; Sarjeant, A. A.; Nguyen, S. T.; Stair, P. C.; Snurr, R. Q.et al. Vapor-Phase Metalation by Atomic Layer Deposition in a Metal-Organic Framework. *Journal of the American Chemical Society* **2013,** *135* (28), 10294.

(86) Kim, I. S.; Borycz, J.; Platero-Prats, A. E.; Tussupbayev, S.; Wang, T. C.; Farha, O. K.; Hupp, J. T.; Gagliardi, L.; Chapman, K. W.; Cramer, C. J.et al. Targeted Single-Site MOF Node Modification: Trivalent Metal Loading via Atomic Layer Deposition. *Chemistry of Materials* **2015,** *27* (13), 4772.

(87) Peters, A. W.; Li, Z.; Farha, O. K.; Hupp, J. T. Atomically Precise Growth of Catalytically Active Cobalt Sulfide on Flat Surfaces and within a Metal-Organic Framework via Atomic Layer Deposition. *Acs Nano* **2015,** *9* (8), 8484.

(88) Wind, R. A.; George, S. M. Quartz Crystal Microbalance Studies of Al2O3 Atomic Layer Deposition Using Trimethylaluminum and Water at 125 degrees C. *Journal of Physical Chemistry A* **2010,** *114* (3), 1281.

(89) Elliott, S. D. Atomic-scale simulation of ALD chemistry. *Semiconductor Science and Technology* **2012,** *27* (7).

(90) Spanggaard, H.; Krebs, F. C. A brief history of the development of organic and polymeric photovoltaics. *Solar Energy Materials and Solar Cells* **2004,** *83* (2-3), 125.

(91) Deria, P.; Bury, W.; Hupp, J. T.; Farha, O. K. Versatile functionalization of the NU-1000 platform by solvent-assisted ligand incorporation. *Chemical Communications* **2014,** *50* (16), 1965.

(92) Deria, P.; Mondloch, J. E.; Tylianakis, E.; Ghosh, P.; Bury, W.; Snurr, R. Q.; Hupp, J. T.; Farha, O. K. Perfluoroalkane Functionalization of NU-1000 via Solvent-Assisted Ligand Incorporation: Synthesis and CO2 Adsorption Studies. *Journal of the American Chemical Society* **2013,** *135* (45), 16801.

(93) Wang, T. C.; Vermeulen, N. A.; Kim, I. S.; Martinson, A. B. F.; Stoddart, J. F.; Hupp, J. T.; Farha, O. K. Scalable synthesis and post-modification of a mesoporous metal-organic framework called NU-1000. *Nature Protocols* **2016,** *11* (1), 149.

(94) Stuckless, J. T.; Frei, N. A.; Campbell, C. T. A Novel Single-Crystal Adsorption Calorimeter and Additions for Determining Metal Adsorption and Adhesion Energies. *Rev. Sci. Instrum.* **1998,** *69* (6), 2427.

(95) Lownsbury, J. M.; Sharp, J. C.; Mann, E. J.; Campbell, C. T. Calcium Thin Film Growth on Phenyl-C-61-Butyric Acid Methyl Ester (PCBM): Interface Structure and Energetics. *Journal of Physical Chemistry C* **2015,** *119* (32), 18444.

(96) Pauls, S. W.; Campbell, C. T. Magic-Angle Thermal-Desorption Mass-Spectroscopy. *Surf. Sci.* **1990,** *226* (3), 250.

(97) Brongersma, H. H.; Draxler, M.; de Ridder, M.; Bauer, P. Surface Composition Analysis by Low-Energy Ion Scattering. *Surf. Sci. Rep.* **2007,** *62* (3), 63.

(98) Campbell, C. T.; James, T. E. Ion scattering spectroscopy intensities for supported nanoparticles: The hemispherical cap model. *Surface Science* **2015,** *641*, 166.

(99) Stuckless, J. T.; Frei, N. A.; Campbell, C. T. Pyroelectric detector for single-crystal adsorption microcalorimetry: analysis of pulse shape and intensity. *Sensors and Actuators B-Chemical* **2000,** *62* (1), 13.

(100) Stuckless, J. T.; Starr, D. E.; Bald, D. J.; Campbell, C. T. Calorimetric measurements of the energetics of Pb adsorption and adhesion to Mo(100). *Physical Review B* **1997,** *56* (20), 13496.

(101) Stuckless, J. T.; Starr, D. E.; Bald, D. J.; Campbell, C. T. Metal adsorption calorimetry and adhesion energies on clean single-crystal surfaces. *Journal of Chemical Physics* **1997,** *107* (14), 5547.

(102) Zhu, J.; Farmer, J. A.; Ruzycki, N.; Xu, L.; Campbell, C. T.; Henkelman, G. Calcium adsorption on MgO(100): Energetics, structure, and role of defects. *Journal of the American Chemical Society* **2008,** *130* (7), 2314.

(103) Sharp, J. C.; Yao, Y. X.; Campbell, C. T. Silver Nanoparticles on Fe3O4(111): Energetics by Ag Adsorption Calorimetry and Structure by Surface Spectroscopies. *Journal of Physical Chemistry C* **2013,** *117* (47), 24932.

(104) Farmer, J. A.; Baricuatro, J. H.; Campbell, C. T. Ag Adsorption on Reduced CeO2(111) Thin Films. *Journal of Physical Chemistry C* **2010,** *114* (40), 17166.

(105) Farmer, J. A.; Campbell, C. T. Ceria Maintains Smaller Metal Catalyst Particles by Strong Metal-Support Bonding. *Science* **2010,** *329* (5994), 933.

(106) Farmer, J. A.; Campbell, C. T.; Xu, L.; Henkelman, G. Defect Sites and Their Distributions on MgO(100) by Li and Ca Adsorption Calorimetry. *Journal of the American Chemical Society* **2009,** *131* (8), 3098.

(107) Farmer, J. A.; Ruzycki, N.; Zhu, J. F.; Campbell, C. T. Lithium adsorption on MgO(100) and its defects: Charge transfer, structure, and energetics. *Physical Review B* **2009,** *80* (3).

(108) Campbell, C. T.; Parker, S. C.; Starr, D. E. The effect of size-dependent nanoparticle energetics on catalyst sintering. *Science* **2002,** *298* (5594), 811.

(109) Starr, D. E.; Campbell, C. T. Large entropy difference between terrace and step sites on surfaces. *Journal of the American Chemical Society* **2008,** *130* (23), 7321.

(110) Larsen, J. H.; Starr, D. E.; Campbell, C. T. Enthalpies of adsorption of metal atoms on single-crystalline surfaces by microcalorimetry. *Journal of Chemical Thermodynamics* **2001,** *33* (3), 333.

(111) Starr, D. E.; Campbell, C. T. Low-temperature adsorption microcalorimetry: Pb on MgO(100). *Journal of Physical Chemistry B* **2001,** *105* (18), 3776.

(112) Starr, D. E.; Ranney, J. T.; Larsen, J. H.; Musgrove, J. E.; Campbell, C. T. Measurement of the energetics of metal film growth on a semiconductor: Ag/Si(100)-(2 x 1). *Physical Review Letters* **2001,** *87* (10), art. no.

(113) Starr, D. E.; Bald, D. J.; Musgrove, J. E.; Ranney, J. T.; Campbell, C. T. Microcalorimetric measurements of the heat of absorption of Pb on well-defined oxides: MgO(100) and p(2x1)-oxide on Mo(100). *Journal of Chemical Physics* **2001,** *114* (8), 3752.

(114) Ajo, H. M.; Ihm, H.; Moilanen, D. E.; Campbell, C. T. Calorimeter for adsorption energies of larger molecules on single crystal surfaces. *Review of Scientific Instruments* **2004,** *75* (11), 4471.

(115) Sellers, J. R. V.; James, T. E.; Hemmingson, S. L.; Farmer, J. A.; Campbell, C. T. Adsorption calorimetry during metal vapor deposition on single crystal surfaces: Increased flux, reduced optical radiation, and real-time flux and reflectivity measurements. *Review of Scientific Instruments* **2013,** *84* (12).

(116) Fischer-Wolfarth, J.-H.; Hartmann, J.; Farmer, J. A.; Flores-Camacho, J. M.; Campbell, C. T.; Schauermann, S.; Freund, H.-J. An improved single crystal adsorption calorimeter

for determining gas adsorption and reaction energies on complex model catalysts. *Review of Scientific Instruments* **2011,** *82* (2).

(117) Etzel, K. D.; Bickel, K. R.; Schuster, R. A microcalorimeter for measuring heat effects of electrochemical reactions with submonolayer conversions. *Review of Scientific Instruments* **2010,** *81* (3).

(118) Diaz, S. F.; Zhu, J. F.; Harris, J. J. W.; Campbell, C. T. Calorimetric measurement of heats of adsorption and adhesion energies for metals on polymers. *Abstracts of Papers of the American Chemical Society* **2005,** *229*, U741.

(119) Murdey, R.; Stuckless, J. T. Calorimetry of polymer metallization: Copper, calcium, and chromium on PMDA-ODA polyimide. *Journal of the American Chemical Society* **2003,** *125* (13), 3995.

(120) Maeda, K.; Eguchi, M.; Youngblood, W. J.; Mallouk, T. E. Calcium Niobate Nanosheets Prepared by the Polymerized Complex Method as Catalytic Materials for Photochemical Hydrogen Evolution. *Chemistry of Materials* **2009,** *21* (15), 3611.

(121) Maeda, K.; Mallouk, T. E. Comparison of two- and three-layer restacked Dion-Jacobson phase niobate nanosheets as catalysts for photochemical hydrogen evolution. *Journal of Materials Chemistry* **2009,** *19* (27), 4813.

(122) Hata, H.; Kobayashi, Y.; Bojan, V.; Youngblood, W. J.; Mallouk, T. E. Direct deposition of trivalent rhodium hydroxide nanoparticles onto a semiconducting layered calcium niobate for photocatalytic hydrogen evolution. *Nano Letters* **2008,** *8* (3), 794.

(123) Brabec, C. J.; Gowrisanker, S.; Halls, J. J. M.; Laird, D.; Jia, S. J.; Williams, S. P. Polymer-Fullerene Bulk-Heterojunction Solar Cells. *Adv. Mater.* **2010,** *22* (34), 3839.

(124) Meng, Q.; Dong, H.; Hu, W.; Zhu, D. Recent Progress of High Performance Organic Thin Film Field-Effect Transistors. *J. Mater. Chem.* **2011,** *21* (32), 11708.

(125) Waldauf, C.; Schilinsky, P.; Perisutti, M.; Hauch, J.; Brabec, C. J. Solution-Processed Organic n-type Thin-Film Transistors. *Adv. Mater.* **2003,** *15* (24), 2084.

(126) Collins, B. A.; Tumbleston, J. R.; Ade, H. Miscibility, Crystallinity, and Phase Development in P3HT/PCBM Solar Cells: Toward an Enlightened Understanding of Device Morphology and Stability. *J. Phys. Chem. Lett.* **2011,** *2* (24), 3135.

(127) Li, G.; Shrotriya, V.; Huang, J. S.; Yao, Y.; Moriarty, T.; Emery, K.; Yang, Y. High-Efficiency Solution Processable Polymer Photovoltaic Cells by Self-Organization of Polymer Blends. *Nat. Mater.* **2005,** *4* (11), 864.

(128) He, Z. C.; Zhong, C. M.; Su, S. J.; Xu, M.; Wu, H. B.; Cao, Y. Enhanced Power-Conversion Efficiency in Polymer Solar Cells Using an Inverted Device Structure. *Nat. Photonics* **2012,** *6* (9), 591.

(129) Hammond, M. R.; Kline, R. J.; Herzing, A. A.; Richter, L. J.; Germack, D. S.; Ro, H. W.; Soles, C. L.; Fischer, D. A.; Xu, T.; Yu, L. P., et al. Molecular Order in High-Efficiency Polymer/Fullerene Bulk Heterojunction Solar Cells. *ACS Nano* **2011,** *5* (10), 8248.

(130) Deledalle, F.; Tuladhar, P. S.; Nelson, J.; Durrant, J. R.; Kirchartz, T. Understanding the Apparent Charge Density Dependence of Mobility and Lifetime in Organic Bulk Heterojunction Solar Cells. *J. Phys. Chem. C* **2014,** *118* (17), 8837.

(131) Scharber, M. C.; Sariciftci, N. S. Efficiency of bulk-heterojunction organic solar cells. *Prog. Polym. Sci.* **2013,** *38* (12), 1929.

(132) Guan, Z. L.; Kim, J. B.; Wang, H.; Jaye, C.; Fischer, D. A.; Loo, Y. L.; Kahn, A. Direct Determination of the Electronic Structure of the Poly(3-hexylthiophene) : Phenyl-6,6-C61 Butyric Acid Methyl Ester Blend. *Org. Electron.* **2010,** *11* (11), 1779.

(133) van Gennip, W. J. H.; van Duren, J. K. J.; Thune, P. C.; Janssen, R. A. J.; Niemantsverdriet, J. W. The Interfaces of Poly(p-phenylene vinylene) and Fullerene Derivatives with Al, LiF, and Al/LiF Studied by Secondary Ion Mass Spectroscopy and X-ray Photoelectron Spectroscopy: Formation of AlF3 Disproved. *J. Chem. Phys.* **2002,** *117* (10), 5031.

(134) *CRC Handbook of Chemistry and Physics*; 96th ed.; Haynes, W. M., Ed.; CRC Press: Boca Raton, FL, 2016; Section 5 p 4.

(135) Seah, M. P.; Gilmore, L. S.; Beamson, G. XPS: Binding Energy Calibration of Electron Spectrometers 5 - Re-evaluation of the Reference Energies. *Surf. Interface Anal.* **1998,** *26* (9), 642.

(136) Richter, M. H.; Friedrich, D.; Schmeiber, D. Valence and Conduction Band States of PCBM as Probed by Photoelectron Spectroscopy at Resonant Excitation. *Bionanoscience* **2012,** *2* (1), 59.

(137) Lopez, G. P.; Castner, D. G.; Ratner, B. D. XPS O 1s Binding-Energies for Polymers Containing Hydroxyl, Ether, Ketone and Ester Groups. *Surf. Interface Anal.* **1991,** *17* (5), 267.

(138) Tanuma, S.; Powell, C. J.; Penn, D. R. Calculations of Electron Inelastic Mean Free Paths .5. Data for 14 Organic Compounds Over the 50-2000 eV Range. *Surf. Interface Anal.* **1994,** *21* (3), 165.

(139) Tanuma, S.; Powell, C. J.; Penn, D. R. Calculations of Electron Inelastic Mean Free Paths .2. Data for 27 Elements Over the 50-2000 eV Range. *Surf. Interface Anal.* **1991,** *17* (13), 911.

(140) Kiel, J. W.; Kirby, B. J.; Majkrzak, C. F.; Maranville, B. B.; Mackay, M. E. Nanoparticle Concentration Profile in Polymer-Based Solar Cells. *Soft Matter* **2010,** *6* (3), 641.

(141) Paterno, G.; Warren, A. J.; Spencer, J.; Evans, G.; Sakai, V. G.; Blumberger, J.; Cacialli, F. Micro-focused X-ray Diffraction Characterization of High-quality 6,6-Phenyl-C61-Butyric Acid Methyl Ester Single Crystals without Solvent Impurities. *J. Mater. Chem. C* **2013,** *1* (36), 5619.

(142) Ettedgui, E.; Hsieh, B. R.; Gao, Y. Interface Formation of Metals and Poly(p-phenylene vinylene): Surface Species and Band Bending. *Polymer. Adv. Tech.* **1997,** *8* (7), 408.

(143) Franzosini, P.; Sanesi, M. *Thermodynamic and Transport Properties of Organic Salts*; 1st ed.; Pergamon Press Inc.: New York, 1980.

(144) Treat, N. D.; Brady, M. A.; Smith, G.; Toney, M. F.; Kramer, E. J.; Hawker, C. J.; Chabinyc, M. L. Interdiffusion of PCBM and P3HT Reveals Miscibility in a Photovoltaically Active Blend. *Adv. Energy Mater.* **2011,** *1* (1), 82.

(145) Kokubu, R.; Yang, Y. Vertical Phase Separation of Conjugated Polymer and Fullerene Bulk Heterojunction Films Induced by High Pressure Carbon Dioxide Treatment at Ambient Temperature. *Phys. Chem. Chem. Phys.* **2012,** *14* (23), 8313.

(146) Karagiannidis, P. G.; Georgiou, D.; Pitsalidis, C.; Laskarakis, A.; Logothetidis, S. Evolution of Vertical Phase Separation in P3HT:PCBM Thin Films Induced by Thermal Annealing. *Mater. Chem. Phys.* **2011,** *129* (3), 1207.

(147) Campoy-Quiles, M.; Ferenczi, T.; Agostinelli, T.; Etchegoin, P. G.; Kim, Y.; Anthopoulos, T. D.; Stavrinou, P. N.; Bradley, D. D. C.; Nelson, J. Morphology

Evolution via Self-Organization and Lateral and Vertical Diffusion in Polymer:Fullerene Solar Cell Blends. *Nat. Mater.* **2008,** *7* (2), 158.

(148) Lownsbury, J. M.; Santos-Lopez, I. A.; Zhang, W.; Campbell, C. T.; Yu, H. S.; Liu, W.-G.; Cramer, C. J.; Truhlar, D. G.; Wang, T.; Hupp, J. T.et al. Calcium Vapor Adsorption on the Metal-Organic Framework NU-1000: Structure and Energetics. *Journal of Physical Chemistry C* **2016,** *submitted*.

(149) Katz, M. J.; Brown, Z. J.; Colon, Y. J.; Siu, P. W.; Scheidt, K. A.; Snurr, R. Q.; Hupp, J. T.; Farha, O. K. A Facile Synthesis of UiO-66, UiO-67 and their Derivatives. *Chemical Communications* **2013,** *49* (82), 9449.

(150) Furukawa, H.; Ko, N.; Go, Y. B.; Aratani, N.; Choi, S. B.; Choi, E.; Yazaydin, A. O.; Snurr, R. Q.; O'Keeffe, M.; Kim, J.et al. Ultrahigh Porosity in Metal-Organic Frameworks. *Science* **2010,** *329* (5990), 424.

(151) Deria, P.; Gomez-Gualdron, D. A.; Bury, W.; Schaef, H. T.; Wang, T. C.; Thallapally, P. K.; Sarjeant, A. A.; Snurr, R. Q.; Hupp, J. T.; Farha, O. K. Ultraporous, Water Stable, and Breathing Zirconium-Based Metal-Organic Frameworks with ftw Topology. *Journal of the American Chemical Society* **2015,** *137* (40), 13183.

(152) Zhao, D.; Timmons, D. J.; Yuan, D.; Zhou, H.-C. Tuning the Topology and Functionality of Metal-Organic Frameworks by Ligand Design. *Accounts of Chemical Research* **2011,** *44* (2), 123.

(153) Vermoortele, F.; Ameloot, R.; Alaerts, L.; Matthessen, R.; Carlier, B.; Fernandez, E. V. R.; Gascon, J.; Kapteijn, F.; De Vos, D. E. Tuning the Catalytic Performance of Metal-Organic Frameworks in Fine Chemistry by Active Site Engineering. *Journal of Materials Chemistry* **2012,** *22* (20), 10313.

(154) Gomez-Gualdron, D. A.; Gutov, O. V.; Krungleviciute, V.; Borah, B.; Mondloch, J. E.; Hupp, J. T.; Yildirim, T.; Farha, O. K.; Snurr, R. Q. Computational Design of Metal-Organic Frameworks Based on Stable Zirconium Building Units for Storage and Delivery of Methane. *Chemistry of Materials* **2014,** *26* (19), 5632.

(155) Allendorf, M. D.; Bauer, C. A.; Bhakta, R. K.; Houk, R. J. T. Luminescent metal-organic frameworks. *Chemical Society Reviews* **2009,** *38* (5), 1330.

(156) Kreno, L. E.; Leong, K.; Farha, O. K.; Allendorf, M.; Van Duyne, R. P.; Hupp, J. T. Metal-Organic Framework Materials as Chemical Sensors. *Chemical Reviews* **2012,** *112* (2), 1105.

(157) Horcajada, P.; Serre, C.; Vallet-Regi, M.; Sebban, M.; Taulelle, F.; Ferey, G. Metal-organic frameworks as efficient materials for drug delivery. *Angewandte Chemie-International Edition* **2006,** *45* (36), 5974.

(158) Planas, N.; Mondloch, J. E.; Tussupbayev, S.; Borycz, J.; Gagliardi, L.; Hupp, J. T.; Farha, O. K.; Cramer, C. J. Defining the Proton Topology of the Zr-6-Based Metal-Organic Framework NU-1000. *Journal of Physical Chemistry Letters* **2014,** *5* (21), 3716.

(159) Mondloch, J. E.; Katz, M. J.; Planas, N.; Semrouni, D.; Gagliardi, L.; Hupp, J. T.; Farha, O. K. Are Zr-6-based MOFs water stable? Linker hydrolysis vs. capillary-force-driven channel collapse. *Chemical Communications* **2014,** *50* (64), 8944.

(160) Schroeder, F.; Esken, D.; Cokoja, M.; van den Berg, M. W. E.; Lebedev, O. I.; van Tendeloo, G.; Walaszek, B.; Buntkowsky, G.; Limbach, H. H.; Chaudret, B.et al. Ruthenium nanoparticles inside porous Zn4O(bdC)(3) by hydrogenolysis of adsorbed Ru(cod)(cot) : A solid-state reference system for surfactant-stabilized ruthenium colloids. *Journal of the American Chemical Society* **2008,** *130* (19), 6119.

(161) Houk, R. J. T.; Jacobs, B. W.; El Gabaly, F.; Chang, N. N.; Talin, A. A.; Graham, D. D.; House, S. D.; Robertson, I. M.; Allendorf, M. D. Silver Cluster Formation, Dynamics, and Chemistry in Metal-Organic Frameworks. *Nano Letters* **2009,** *9* (10), 3413.

(162) Klet, R. C.; Wang, T. C.; Fernandez, L. E.; Truhlar, D. G.; Hupp, J. T.; Farha, O. K. Synthetic Access to Atomically Dispersed Metals in Metal-Organic Frameworks via a Combined Atomic-Layer-Deposition-in-MOF and Metal-Exchange Approach. *Chemistry of Materials* **2016,** *28* (4), 1213.

(163) Campbell, C. T.; Lytken, O. Experimental measurements of the energetics of surface reactions. *Surface Science* **2009,** *603* (10-12), 1365.

(164) Kung, C.-W.; Wang, T. C.; Mondloch, J. E.; Fairen-Jimenez, D.; Gardner, D. M.; Bury, W.; Klingsporn, J. M.; Barnes, J. C.; Van Duyne, R.; Stoddart, J. F.et al. Metal-Organic Framework Thin Films Composed of Free-Standing Acicular Nanorods Exhibiting Reversible Electrochromism. *Chemistry of Materials* **2013,** *25* (24), 5012.

(165) Pandey, A. K.; Shaw, P. E.; Samuel, I. D. W.; Nunzi, J.-M. Effect of metal cathode reflectance on the exciton-dissociation efficiency in heterojunction organic solar cells. *Applied Physics Letters* **2009,** *94* (10).

(166) Frisch, M. J.; Trucks, G. W.; Schlegel, H. B.; Scuseria, G. E.; Robb, M. A.; Cheeseman, J. R.; Scalmani, G.; Barone, V.; Mennucci, B.; Petersson, G. A.et al.; Gaussian, Inc.: Wallingford, CT, 2009.

(167) Dovesi, R.; Orlando, R.; Erba, A.; Zicovich-Wilson, C. M.; Civalleri, B.; Casassa, S.; Maschio, L.; Ferrabone, M.; De La Pierre, M.; D'Arco, P.et al. CRYSTAL14: A Program for the Ab Initio Investigation of Crystalline Solids. *International Journal of Quantum Chemistry* **2014,** *114* (19), 1287.

(168) Zhao, Y.; Truhlar, D. G. A new local density functional for main-group thermochemistry, transition metal bonding, thermochemical kinetics, and noncovalent interactions. *Journal of Chemical Physics* **2006,** *125* (19).

(169) Zhao, Y.; Truhlar, D. G. The M06 suite of density functionals for main group thermochemistry, thermochemical kinetics, noncovalent interactions, excited states, and transition elements: two new functionals and systematic testing of four M06-class functionals and 12 other functionals. *Theoretical Chemistry Accounts* **2008,** *120* (1-3), 215.

(170) Yu, H.; Truhlar, D. G. What Dominates the Error in the CaO Diatomic Bond Energy Predicted by Various Approximate Exchange-Correlation Functionals? *Journal of Chemical Theory and Computation* **2014,** *10* (6), 2291.

(171) Ditchfield, R.; Hehre, W. J.; Pople, J. A. Self-Consistent Molecular-Orbital Methods .9. Extended Gaussian-Type Basis for Molecular-Orbital Studies of Organic Molecules. *Journal of Chemical Physics* **1971,** *54* (2), 724.

(172) Hehre, W. J.; Pople, J. A. Self-Consistent Molecular-Orbital Methods .13. Extended Gaussian-Type Basis for Boron. *Journal of Chemical Physics* **1972,** *56* (8), 4233.

(173) Binkley, J. S.; Pople, J. A. Self-Consistent Molecular-Orbital Methods .19. Split-Valence Gaussian-Type Basis Sets for Beryllium. *Journal of Chemical Physics* **1977,** *66* (2), 879.

(174) Hehre, W. J.; Ditchfield, R.; Pople, J. A. Self-Consistent Molecular-Orbital Methods .12. Further Extensions of Gaussian-Type Basis Sets for Use in Molecular-Orbital Studies of Organic Molecules. *Journal of Chemical Physics* **1972,** *56* (5), 2257.

(175) Francl, M. M.; Pietro, W. J.; Hehre, W. J.; Binkley, J. S.; Gordon, M. S.; Defrees, D. J.; Pople, J. A. Self-Consistent Molecular-Orbital Methods .23. A Polarization-Type Basis Set for 2nd-Row Elements. *Journal of Chemical Physics* **1982,** *77* (7), 3654.

(176) Andrae, D.; Haussermann, U.; Dolg, M.; Stoll, H.; Preuss, H. Energy-Adjusted Ab Initio Pseudopotentials for the 2nd and 3rd Row Transition-Elements. *Theoretica Chimica Acta* **1990,** *77* (2), 123.

(177) Martin, J. M. L.; Sundermann, A. Correlation consistent valence basis sets for use with the Stuttgart-Dresden-Bonn relativistic effective core potentials: The atoms Ga-Kr and In-Xe. *Journal of Chemical Physics* **2001,** *114* (8), 3408.

(178) Kaupp, M.; Schleyer, P. V.; Stoll, H.; Preuss, H. Pseudopotential Approaches to Ca, Sr, and Ba Hydrides - Why Are Some Alkaline-Earth MX2 Compounds Bent? *Journal of Chemical Physics* **1991,** *94* (2), 1360.

(179) Alecu, I. M.; Zheng, J.; Zhao, Y.; Truhlar, D. G. Computational Thermochemistry: Scale Factor Databases and Scale Factors for Vibrational Frequencies Obtained from Electronic Model Chemistries. *Journal of Chemical Theory and Computation* **2010,** *6* (9), 2872.

(180) Yu, H. S.; Fiedler, L. J.; Alecu, I. M.; Truhlar, D. G. *Computer Physics Communications* **2016,** *submitted*.

(181) Ertl, G.; Küppers, J. *Low Energy Electrons and Surface Chemistry*; VCH: Weinheim, Germany, 1985.

(182) *Handbook of X-Ray Photoelectron Spectroscopy*; Wagner, C. D.; Riggs, W. M.; Davis, L. E.; Moulder, J. F.; Muilenberg, G. E., Eds.; Perkin-Elmer Corporation, Physical Electronics Division: 6509 Flying Cloud Drive, Eden Prairie, MN, 1979.

(183) Silva, M. P.; Costa, C. M.; Sencadas, V.; Paleo, A. J.; Lanceros-Mendez, S. Degradation of the dielectric and piezoelectric response of beta-poly(vinylidene fluoride) after temperature annealing. *Journal of Polymer Research* **2011,** *18* (6), 1451.

(184) Rittmeyer, P.; Weitelmann, U. In *Ullmann's Encyclopedia of Industrial Chemistry*; Wiley - CVH Verlag GmbH & Co. KGaA, 2000.

(185) Marenich, A. V.; Jerome, S. V.; Cramer, C. J.; Truhlar, D. G. Charge Model 5: An Extension of Hirshfeld Population Analysis for the Accurate Description of Molecular Interactions in Gaseous and Condensed Phases. *Journal of Chemical Theory and Computation* **2012,** *8* (2), 527.

(186) Mulliken, R. S. Electronic Population Analysis on LCAO-MO Molecular Wave Functions .1. *Journal of Chemical Physics* **1955,** *23* (10), 1833.

(187) Nanda, K. K.; Maisels, A.; Kruis, F. E.; Fissan, H.; Stappert, S. Higher surface energy of free nanoparticles. *Physical Review Letters* **2003,** *91* (10).

(188) Platero-Prats, A. E.; Mavrandonakis, A.; Gallington, L. C.; Liu, Y.; Hupp, J. T.; Farha, O. K.; Cramer, C. J.; Chapman, K. W. Structural Transitions of the Metal -Oxide Nodes within Metal- Organic Frameworks: On the Local Structures of NU-1000 and UiO-66. *Journal of the American Chemical Society* **2016,** *138* (12), 4178.

(189) Lownsbury, J. M.; Campbell, C. T.; Kim, I. S.; Martinson, A. B. F. Direct Measurement of Reaction Heats during Atomic Layer Deposition by Calorimetry. **2016,** *in preparation*.

(190) Leskela, M.; Ritala, M. Atomic layer deposition chemistry: Recent developments and future challenges. *Angewandte Chemie-International Edition* **2003,** *42* (45), 5548.

(191) Leskela, M.; Ritala, M. Atomic layer deposition (ALD): from precursors to thin film structures. *Thin Solid Films* **2002,** *409* (1), 138.

(192) Dasgupta, N. P.; Meng, X.; Elam, J. W.; Martinson, A. B. F. Atomic Layer Deposition of Metal Sulfide Materials. *Accounts of Chemical Research* **2015,** *48* (2), 341.

(193) Kim, H. Atomic layer deposition of metal and nitride thin films: Current research efforts and applications for semiconductor device processing. *Journal of Vacuum Science & Technology B* **2003,** *21* (6), 2231.

(194) Ylilammi, M. Monolayer thickness in atomic layer deposition. *Thin Solid Films* **1996,** *279* (1-2), 124.

(195) Robertson, J. High dielectric constant gate oxides for metal oxide Si transistors. *Reports on Progress in Physics* **2006,** *69* (2), 327.

(196) Javey, A.; Kim, H.; Brink, M.; Wang, Q.; Ural, A.; Guo, J.; McIntyre, P.; McEuen, P.; Lundstrom, M.; Dai, H. J. High-kappa dielectrics for advanced carbon-nanotube transistors and logic gates. *Nature Materials* **2002,** *1* (4), 241.

(197) Zhu, H.; McDonnell, S.; Qin, X.; Azcatl, A.; Cheng, L.; Addou, R.; Kim, J.; Ye, P. D.; Wallace, R. M. Al2O3 on Black Phosphorus by Atomic Layer Deposition: An in Situ Interface Study. *Acs Applied Materials & Interfaces* **2015,** *7* (23), 13038.

(198) Xu, K. Electrolytes and Interphases in Li-Ion Batteries and Beyond. *Chemical Reviews* **2014,** *114* (23), 11503.

(199) Meng, X.; Yang, X.-Q.; Sun, X. Emerging Applications of Atomic Layer Deposition for Lithium-Ion Battery Studies. *Advanced Materials* **2012,** *24* (27), 3589.

(200) Liu, D.; Liu, Y.; Candelaria, S. L.; Cao, G.; Liu, J.; Jeong, Y.-H. Atomic layer deposition of Al2O3 on V2O5 xerogel film for enhanced lithium-ion intercalation stability. *Journal of Vacuum Science & Technology A* **2012,** *30* (1).

(201) Kozen, A. C.; Lin, C.-F.; Pearse, A. J.; Schroeder, M. A.; Han, X.; Hu, L.; Lee, S.-B.; Rubloff, G. W.; Noked, M. Next-Generation Lithium Metal Anode Engineering via Atomic Layer Deposition. *Acs Nano* **2015,** *9* (6), 5884.

(202) Wise, A. M.; Ban, C.; Weker, J. N.; Misra, S.; Cavanagh, A. S.; Wu, Z.; Li, Z.; Whittingham, M. S.; Xu, K.; George, S. M.et al. Effect of Al2O3 Coating on Stabilizing LiNi0.4Mn0.4Co0.2O2 Cathodes. *Chemistry of Materials* **2015,** *27* (17), 6146.

(203) Dingemans, G.; Kessels, E. Status and prospects of Al2O3-based surface passivation schemes for silicon solar cells. *Journal of Vacuum Science & Technology A* **2012,** *30* (4).

(204) Zhang, Q.; Dandeneau, C. S.; Zhou, X.; Cao, G. ZnO Nanostructures for Dye-Sensitized Solar Cells. *Advanced Materials* **2009,** *21* (41), 4087.

(205) Naghavi, N.; Abou-Ras, D.; Allsop, N.; Barreau, N.; Buecheler, S.; Ennaoui, A.; Fischer, C. H.; Guillen, C.; Hariskos, D.; Herrero, J.et al. Buffer layers and transparent conducting oxides for chalcopyrite Cu(In,Ga)(S,Se)(2) based thin film photovoltaics: present status and current developments. *Progress in Photovoltaics* **2010,** *18* (6), 411.

(206) Chang, C.-Y.; Lee, K.-T.; Huang, W.-K.; Siao, H.-Y.; Chang, Y.-C. High-Performance, Air-Stable, Low-Temperature Processed Semitransparent Perovskite Solar Cells Enabled by Atomic Layer Deposition. *Chemistry of Materials* **2015,** *27* (14), 5122.

(207) Chen, Y. W.; Prange, J. D.; Duehnen, S.; Park, Y.; Gunji, M.; Chidsey, C. E. D.; McIntyre, P. C. Atomic layer-deposited tunnel oxide stabilizes silicon photoanodes for water oxidation. *Nature Materials* **2011,** *10* (7), 539.

(208) McDowell, M. T.; Lichterman, M. F.; Carim, A. I.; Liu, R.; Hu, S.; Brunschwig, B. S.; Lewis, N. S. The Influence of Structure and Processing on the Behavior of TiO2 Protective Layers for Stabilization of n-Si/TiO2/Ni Photoanodes for Water Oxidation. *Acs Applied Materials & Interfaces* **2015,** *7* (28), 15189.

(209) Lu, J.; Fu, B.; Kung, M. C.; Xiao, G.; Elam, J. W.; Kung, H. H.; Stair, P. C. Coking- and Sintering-Resistant Palladium Catalysts Achieved Through Atomic Layer Deposition. *Science* **2012,** *335* (6073), 1205.

(210) Dixon-Warren, S. J.; Kovar, M.; Wartnaby, C. E.; King, D. A. Pyroelectric Single-Crystal Adsorption Microcalorimetry at Low Temperatures - Oxygen on Ni(100). *Surface Science* **1994,** *307*, 16.

(211) Dillon, A. C.; Ott, A. W.; Way, J. D.; George, S. M. Surface-Chemistry of Al2O3 Deposition Using Al(CH3)3 and H2O in a Binary Reaction Sequence. *Surface Science* **1995,** *322* (1-3), 230.

(212) Groner, M. D.; Elam, J. W.; Fabreguette, F. H.; George, S. M. Electrical characterization of thin Al2O3 films grown by atomic layer deposition on silicon and various metal substrates. *Thin Solid Films* **2002,** *413* (1-2), 186.

(213) Groner, M. D.; Fabreguette, F. H.; Elam, J. W.; George, S. M. Low-temperature Al2O3 atomic layer deposition. *Chemistry of Materials* **2004,** *16* (4), 639.

(214) Rahtu, A.; Alaranta, T.; Ritala, M. In situ quartz crystal microbalance and quadrupole mass spectrometry studies of atomic layer deposition of aluminum oxide from trimethylaluminum and water. *Langmuir* **2001,** *17* (21), 6506.

(215) Riha, S. C.; Libera, J. A.; Elam, J. W.; Martinson, A. B. F. Design and implementation of an integral wall-mounted quartz crystal microbalance for atomic layer deposition. *Review of Scientific Instruments* **2012,** *83* (9).

(216) Puurunen, R. L. Correlation between the growth-per-cycle and the surface hydroxyl group concentration in the atomic layer deposition of aluminum oxide from trimethylaluminum and water. *Applied Surface Science* **2005,** *245* (1-4), 6.

(217) Widjaja, Y.; Musgrave, C. B. Quantum chemical study of the mechanism of aluminum oxide atomic layer deposition. *Applied Physics Letters* **2002,** *80* (18), 3304.

(218) Elliott, S. D.; Greer, J. C. Simulating the atomic layer deposition of alumina from first principles. *Journal of Materials Chemistry* **2004,** *14* (21), 3246.

(219) Elliott, S. D.; Pinto, H. P. Modelling the deposition of high-k dielectric films by first principles. *Journal of Electroceramics* **2004,** *13* (1-3), 117.

(220) Elliott, S. D.; Dey, G.; Maimaiti, Y.; Ablat, H.; Filatova, E. A.; Fomengia, G. N. Modeling Mechanism and Growth Reactions for New Nanofabrication Processes by Atomic Layer Deposition. *Advanced Materials* **2016,** *28*, 5367.

(221) Shirazi, M.; Elliott, S. D. Cooperation between adsorbates accounts for the activation of atomic layer deposition reactions. *Nanoscale* **2015,** *7* (14), 6311.

(222) Weckman, T.; Laasonen, K. First principles study of the atomic layer deposition of alumina by TMA-H2O-process. *Physical Chemistry Chemical Physics* **2015,** *17* (26), 17322.

(223) Sandupatla, A. S.; Alexopoulos, K.; Reyniers, M.-F.; Marin, G. B. Ab Initio Investigation of Surface Chemistry of Alumina ALD on Hydroxylated gamma-Alumina Surface. *Journal of Physical Chemistry C* **2015,** *119* (23), 13050.

(224) Travis, C. D.; Adomaitis, R. A. Modeling alumina atomic layer deposition reaction kinetics during the trimethylaluminum exposure. *Theoretical Chemistry Accounts* **2013,** *133* (1).

(225) Nilsen, O.; Fjellvag, H. Measuring the heat evolved from individual reaction steps in atomic layer deposition. *Journal of Thermal Analysis and Calorimetry* **2011,** *105* (1), 33.

(226) Wilson, C. A.; Grubbs, R. K.; George, S. M. Nucleation and growth during Al2O3 atomic layer deposition on polymers. *Chemistry of Materials* **2005,** *17* (23), 5625.

(227) Liang, X. H.; Hakim, L. F.; Zhan, G. D.; McCormick, J. A.; George, S. M.; Weimer, A. W.; Spencer, J. A.; Buechler, K. J.; Blackson, J.; Wood, C. J.et al. Novel processing to produce polymer/ceramic nanocomposites by atomic layer deposition. *Journal of the American Ceramic Society* **2007,** *90* (1), 57.

(228) Bakke, J. R.; Pickrahn, K. L.; Brennan, T. P.; Bent, S. F. Nanoengineering and interfacial engineering of photovoltaics by atomic layer deposition. *Nanoscale* **2011,** *3* (9), 3482.

(229) van Delft, J. A.; Garcia-Alonso, D.; Kessels, W. M. M. Atomic layer deposition for photovoltaics: applications and prospects for solar cell manufacturing. *Semiconductor Science and Technology* **2012,** *27* (7).

(230) Kim, I. S.; Martinson, A. B. F. Stabilizing hybrid perovskites against moisture and temperature via non-hydrolytic atomic layer deposited overlayers. *Journal of Materials Chemistry A* **2015,** *3* (40), 20092.

(231) Miikkulainen, V.; Leskela, M.; Ritala, M.; Puurunen, R. L. Crystallinity of inorganic films grown by atomic layer deposition: Overview and general trends. *Journal of Applied Physics* **2013,** *113* (2).

(232) *NIST Chemistry WebBook, NIST Standard Reference Database Number 69*; Linstrom, P. J.; Mallard, W. G., Eds.; National Institute of Standards and Technology: Gaithersburg, MD; http://webbook.nist.gov (accessed May 24, 2016).

(233) Tavakoli, A. H.; Maram, P. S.; Widgeon, S. J.; Rufner, J.; van Benthem, K.; Ushakov, S.; Sen, S.; Navrotsky, A. Amorphous Alumina Nanoparticles: Structure, Surface Energy, and Thermodynamic Phase Stability. *Journal of Physical Chemistry C* **2013,** *117* (33), 17123.

(234) Elam, J. W.; Martinson, A. B. F.; Pellin, M. J.; Hupp, J. T. Atomic layer deposition of In2O3 using cyclopentadienyl indium: A new synthetic route to transparent conducting oxide films. *Chemistry of Materials* **2006,** *18* (15), 3571.

(235) Diebold, U. The surface science of titanium dioxide. *Surface Science Reports* **2003,** *48* (5-8), 53.

(236) Chen, X.; Mao, S. S. Titanium dioxide nanomaterials: Synthesis, properties, modifications, and applications. *Chemical Reviews* **2007,** *107* (7), 2891.

(237) Fujishima, A.; Zhang, X. T.; Tryk, D. A. TiO2 photocatalysis and related surface phenomena. *Surface Science Reports* **2008,** *63* (12), 515.

(238) Kemell, M.; Pore, V.; Tupala, J.; Ritala, M.; Leskela, M. Atomic layer deposition of nanostructured TiO2 photocatalysts via template approach. *Chemistry of Materials* **2007,** *19* (7), 1816.

(239) Park, K.; Zhang, Q.; Garcia, B. B.; Zhou, X.; Jeong, Y.-H.; Cao, G. Effect of an Ultrathin TiO2 Layer Coated on Submicrometer-Sized ZnO Nanocrystallite Aggregates by Atomic Layer Deposition on the Performance of Dye-Sensitized Solar Cells. *Advanced Materials* **2010,** *22* (21), 2329.

(240) Hagfeldt, A.; Boschloo, G.; Sun, L. C.; Kloo, L.; Pettersson, H. Dye-Sensitized Solar Cells. *Chemical Reviews* **2010,** *110* (11), 6595.

(241) Xie, Q.; Jiang, Y. L.; Detavernier, C.; Deduytsche, D.; Van Meirhaeghe, R. L.; Ru, G. P.; Li, B. Z.; Qu, X. P. Atomic layer deposition of TiO2 from tetrakis-dimethyl-amido

titanium or Ti isopropoxide precursors and H2O. *Journal of Applied Physics* **2007,** *102* (8).

(242) Elam, J. W.; Schuisky, M.; Ferguson, J. D.; George, S. M. Surface chemistry and film growth during TiN atomic layer deposition using TDMAT and NH3. *Thin Solid Films* **2003,** *436* (2), 145.

(243) Stobbe, E. R.; de Boer, B. A.; Geus, J. W. The reduction and oxidation behaviour of manganese oxides. *Catalysis Today* **1999,** *47* (1-4), 161.

(244) Pickrahn, K. L.; Park, S. W.; Gorlin, Y.; Lee, H.-B.-R.; Jaramillo, T. F.; Bent, S. F. Active MnOx Electrocatalysts Prepared by Atomic Layer Deposition for Oxygen Evolution and Oxygen Reduction Reactions. *Advanced Energy Materials* **2012,** *2* (10), 1269.

(245) Thackeray, M. M. Manganese oxides for lithium batteries. *Progress in Solid State Chemistry* **1997,** *25* (1-2), 1.

(246) Li, H.; Wang, Z. X.; Chen, L. Q.; Huang, X. J. Research on Advanced Materials for Li-ion Batteries. *Advanced Materials* **2009,** *21* (45), 4593.

(247) Burton, B. B.; Fabreguette, F. H.; George, S. M. Atomic layer deposition of MnO using Bis(ethylcyclopentadienyl) manganese and H2O. *Thin Solid Films* **2009,** *517* (19), 5658.

(248) Donald, S. B.; Harrison, I. Dynamically biased RRKM model of activated gas-surface reactivity: vibrational efficacy and rotation as a spectator in the dissociative chemisorption of CH4 on Pt(111). *Physical Chemistry Chemical Physics* **2012,** *14* (5), 1784.

(249) Shim, J. H.; Chao, C. C.; Huang, H.; Prinz, F. B. Atomic layer deposition of yttria-stabilized zirconia for solid oxide fuel cells. *Chemistry of Materials* **2007,** *19* (15), 3850.

(250) Hermes, S.; Zacher, D.; Baunemann, A.; Woll, C.; Fischer, R. A. Selective growth and MOCVD loading of small single crystals of MOF-5 at alumina and silica surfaces modified with organic self-assembled monolayers. *Chemistry of Materials* **2007,** *19* (9), 2168.

(251) Detavernier, C.; Dendooven, J.; Sree, S. P.; Ludwig, K. F.; Martens, J. A. Tailoring nanoporous materials by atomic layer deposition. *Chemical Society Reviews* **2011,** *40* (11), 5242.

(252) Porter, S. G. A Brief Guide to Pyroelectric Detectors. *Ferroelectrics* **1981,** *33* (1-4), 193.

(253) Kitamura, K.; Furukawa, Y.; Niwa, K.; Gopalan, V.; Mitchell, T. E. Crystal growth and low coercive field 180 degrees domain switching characteristics of stoichiometric LiTaO3. *Applied Physics Letters* **1998,** *73* (21), 3073.